PhD Thesis

Experimental study for spectroscopy of Ξ^--atomic X rays

(Ξ^-原子X線分光の実験的研究)

Manami Fujita

Graduate School of Science, Department of Physics,
Tohoku University

2019

Abstract

This thesis describes a first pioneering study on exotic atoms containing Ξ^-, one of hyperons with two strange quarks. The Ξ^- atomic X-ray spectroscopy is one of the useful ways to obtain information on the Ξ-nuclear interaction. The shift of the X-ray energy (ΔE) from the energy by the Coulomb interaction only and the width of the X-ray peak depend on the depth of a real and imaginary parts of the Ξ^--nuclear potential. The experimental methods and the procedure of data analysis for the Ξ^- atomic X-ray spectroscopy experiment are discussed in this thesis.

The most of produced Ξ^-s decay before stopping and cause a huge background. The key of experiments to measure X rays with good significance is to select Ξ^--stop events cleanly and two methods were developed. In method 1, Ξ^--stop events are identified in the developed nuclear emulsion image. And in method 2, the Ξ^- with a large stop probability at the target is selected using information of the Ξ^- momentum.

The J-PARC E07 experiment, which aims at searching for double-Λ hypernuclei, was performed at the J-PARC K1.8 beam line in 2016 and 2017. In the experiment, X-ray measurement of Ξ^-C, Ξ^-Ag, and Ξ^-Br atoms was also performed at the same time. Ξ^-s were produced in a diamond target via the (K^-, K^+) reaction and then detected using the nuclear emulsion. By emulsion image analysis, the Ξ^- atoms, as well as double-Λ hypernuclei were searched for. The Ξ^- atomic X rays were measured by the array of germanium (Ge) detectors, called Hyperball-X. The analysis of the (K^-, K^+) reaction by the magnetic spectrometers and analysis of the Ξ^- track by silicon strip detectors predicted the position where Ξ^- hit at the emulsion surface. This is called a counter-emulsion hybrid method. In this method, the prediction by counters shortened the time for the emulsion image analysis.

By coincidence of the Ξ^--stop events selected by the emulsion image analysis and the X-ray hits by Hyperball-X analysis, the Ξ^-Ag and Ξ^-Br atomic X-ray spectrum was obtained. At present, analyzed data correspond to 20% of the estimated total σ-stop yield. No evident peaks were found in the expected X-ray regions. The background level was evaluated to be $0.17^{+0.57}_{-0.10}$ in 1 keV around the 370-keV region. When the emulsion image analysis is completed, an expected X-ray yield of the Ag($8J \to 7I$) transition will be 7.75 counts for σ-stop events and $S/\sqrt{N}$ would be 4.56 in the $\pm 2\sigma$ peak region.

As a byproduct, the Ξ^-C atomic X-ray spectrum was obtained by coincidence analysis of the (K^-, K^+) reaction and Hyperball-X. The X ray of the ^{12}C($3D \to 2P$) transition was searched for, but no evident peak with 3σ significance was found. Then, the branching ratio that Ξ^- in the $3D$ orbit was absorbed by the nucleus due to the Ξ^--nuclear interaction was constrained from the upper limit of the X-ray yield. This limit was compared to the theoretical calculation using the Woods-Saxon type optical potential. It was found that the experimental sensitivity was not sufficient to constrain the imaginary part of the Ξ^--nuclear potential. More improvements, for

example optimization of the target thickness and detector developments to reject contamination of the background, are needed in the future experiment.

From this research, the method of Ξ^- atomic X-ray spectroscopy was established and the present sensitivity was shown. If the data is acquired for a double period using a larger Ge array with 3 times efficiency of Hyperball-X, a statistical error will be improved to be comparable with a systematic error and the energy shift would be measured with 100-eV accuracy.

Contents

List of Tables

List of Figures

Chapter 1

Introduction

This thesis describes a pioneering study on exotic atoms containing Ξ^-, one of hyperons with two strange quarks. In this chapter, basic explanations on the ΞN and Ξ-nuclear interactions with Ξ^--hypernuclei and Ξ^--atoms are given. Then, introduction of Ξ^- atomic X-ray spectroscopy is described.

1.1 Nuclear and hypernuclear physics

A baryon is a fermion consisting of three quarks. Nuclei are formed of nucleons via the strong interaction, and various matter consists of atoms. Understanding the strong interaction leads to understanding the formation and the diversity of matter.

The nucleons (N), namely protons and neutrons, consist of only up and down quarks, and they have almost the same properties except for their charge. Thus a proton and a neutron can be considered to be identical particles that differ only in the z component of isospin. They are described by isospin vectors which are orthogonal to each other. That is, nucleons are expressed in the isospin 2-dimensional special unitary group SU(2). The N-N interaction can be understood under the isospin SU(2) symmetry.

Of six kinds of quarks, consider the light three, up, down and strange quarks. Assuming the masses of u, d and s quarks are the same, they can be considered as the identical particles except for the difference in the quantum number of flavor. A baryon consisting of these quarks is expressed by flavor 3-dimensional special unitary group SU(3). The baryons which contain strange quarks such as Λ, Σ, Ξ, are called hyperons (Y).

Nucleons and hyperons, are classified into the octet with spin 1/2 and the decuplet with spin 3/2. The baryon octet is represented using the axes for charge (Q) and for strangeness (S) as shown in Fig. 1.1. Protons and neutrons classified as $S = 0$ had been investigated by numerous scattering experiments. On the other hand, scattering experiments with the hyperons are difficult due to their short lifetime of the order of 100 ps. Researches on the $S = -1$ systems, such as Λ hypernuclei and Σ hypernuclei, have progressed at KEK, BNL, J-PARC, JLab and MAMI. In

particular, spectroscopy of Λ hypernuclei has been well studied as reviewed in [1]. Information on the ΛN interaction has been obtained from such experimental researches together with theoretical studies. Σ-hypernulear state was searched for by the reaction spectroscopy experiment at KEK-PS via the (π^-, K^+) reaction and it was found that the Σ^-N interaction was repulsive [4]. ΣN interaction was also investigated by Σ^- atomic X-ray spectroscopy (see Subsection 1.3.2). On the other hand, for the ΞN interaction, the experimental data are especially limited.

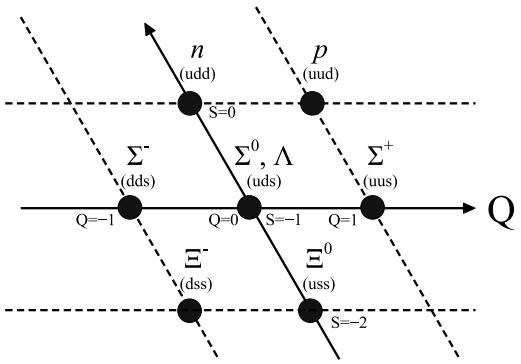

Figure 1.1: The baryon octet with spin-parity $1/2^+$

1.2 Physics of ΞN interaction

Ξ^- particle is one of hyperons which contains two strange quarks, and its mass is 1321.71 ± 0.07 MeV/c^2 and lifetime is 163.9 ± 0.015 ps [2]. In this section, the purpose of investigation for ΞN interaction and past experiments are described.

1.2.1 Motivation

The Y-N interaction should be investigated to understand the baryon-baryon interactions under the flavor SU(3) symmetry, As described above, ΛN and ΣN interactions are better known than ΞN interaction. For the $S = -2$ sector with Ξ^-(dss) and Ξ^0(uss) hyperons, the small cross section of Ξ production makes experiments difficult. For this reason experimental studies on $S = -2$ system such as Ξ^- hypernuclei and Ξ^- atoms are extremely limited so far even though they are essential for the general understanding of the baryon-baryon interaction.

In addition, research on Ξ^--nucleon interaction would give important information for understanding neutron stars. A neutron star, which has a radius of about 10 km and a density of 10^{12} kg/cm^3, is produced after a supernova explosion and mainly it is composed with neutron. In such high density matter, some neutrons occupy high-lying orbits because they cannot occupy the same orbit with others due to the Pauli blocking. In such a situation, to reduce a fermi energy, some of the neutrons are expected to convert to other particles which are not affected by the Pauli blocking

of nucleons. As described in ref. [3], Λ and Ξ^- hyperons are the candidates. The understanding for ΞN interaction gives us information that whether Ξ^-s exist or not in neutron stars.

1.2.2 Past experiments on the ΞN interaction

In the past experiments for investigation of ΞN interaction, a Ξ^- particle can be produced using the (K^-, K^+) reaction which is a double charge and double strangeness exchange reaction.

The (K^-, K^+) reaction itself had been studied in order to clarify various possible processes. At Lawrence Radiation Laboratory, the production of Ξ^- and Ξ^{-*} hyperons and their decay were studied in the experiment using a hydrogen bubble chamber. Not only the processes with two particles in the final states such as $K^+\Xi^-$, $K^+\Xi^{-*}$, but also three-particle states such as $K^+\Xi^-\pi^0$ and $K^+\Xi^0\pi^-$ were identified by their trajectories. The cross section and the angular distribution of each process were reported [5]. At KEK E176, for study of the (K^-, K^+) reaction, a nuclear emulsion was used to record trajectories of charged particles [6][7]. At KEK-PS E224, using scintillation fiber detector, productions of scaler and vector mesons ($f_0/a_0/\phi$) via the (K^-, K^+) reaction were studied [8]. According to Ref. [9], the cross section of the elementary process depends on K^- momentum p_k in laboratory frame and the cross section peaks around $p_k(\mathrm{lab}) = 1.8$ GeV/c in forward angles.

The Ξ^- bound systems, namely, Ξ^- hypernuclei or Ξ^- atoms, were produced in two ways using the (K^-, K^+) reaction. The first way is to produce a Ξ^- hypernucleus directly by replacing a proton in a nucleus with a Ξ^-. The second one is to stop a Ξ^- in material and make a Ξ^- atom. Since Ξ^- is negatively charged, it replaces an electron in an outer orbit and forms Ξ^- atom, which is similar to other exotic atoms such as $\mu^-, \bar{p}, \pi^-, K^-$ and Σ^--atoms. The captured Ξ^- cascades down to inner orbits while emitting Auger electrons and X rays. At the end, it is absorbed by a nucleus via the strong interaction between the Ξ^- and the nucleus. Both of these two ways can provide information of the Ξ-nuclear potential. Overview of the past experiments and the outcome of the present study on the Ξ-nuclear potential are explained in the following.

Mass spectroscopy of Ξ^- hypernuclei by a direct production

The first way is to produce Ξ^- hypernuclei directly via the (K^-, K^+) reaction. The mass spectroscopy of hypernuclei with $S = -2$ using magnetic spectrometers was performed as KEK-PS E224 [10] and AGS E885 experiments [11]. In KEK-PS E224, the ^{12}C(K^-, K^+)X reaction was measured using a scintillation fiber target. As a result, the missing mass distribution as a function of the binding energy (B_{Ξ^-}) of the ^{11}B-Ξ bound system is shown in the left side of Fig. 1.2. The lower figure is expanded around the bound region. The theoretical curve for $^{12}_{\Xi^-}$Be production with Ξ^- potential of Woods-Saxon type are shown in solid lines. Curves assuming the well depth of 12, 16, and 24 MeV are shown in solid line. In AGS E885, the ^{12}C(K^-, K^+)X reaction was measured using a diamond target. The obtained missing mass distributions with the scattered angles of the outgoing K^+ , $\theta_{K^+} < 14^\circ$ and $\theta_{K^+} < 8^\circ$, are shown in the right side of Fig. 1.2. The

arrows represent the expected location of the ground state of ${}^{12}_{\Lambda\Lambda}$Be, ${}^{11}_{\Lambda}$Be+Λ, and ^{11}B+Ξ^-. The theoretical curves with the 12, 14, 16, 18, and 20-MeV well depth of Woods-Saxon potentials were shown in dotted line. In both experiments, statistics and mass resolution were very limited. Since the experimental sensitivity is not sufficient, any signal of Ξ^--hypernuclei, such as ${}^{12}_{\Xi}$Be, was not observed clearly from these experiments. Compared the data to the theoretical curves, the ΞN interaction is suggested to be attractive and a real part of the potential (V_0) is $-10 \sim -20$ MeV.

with the potential depth between 10 and 20 MeV. To obtain a definitive Ξ^- well depth, subsequent experiments with better resolution and higher statistic are desired.

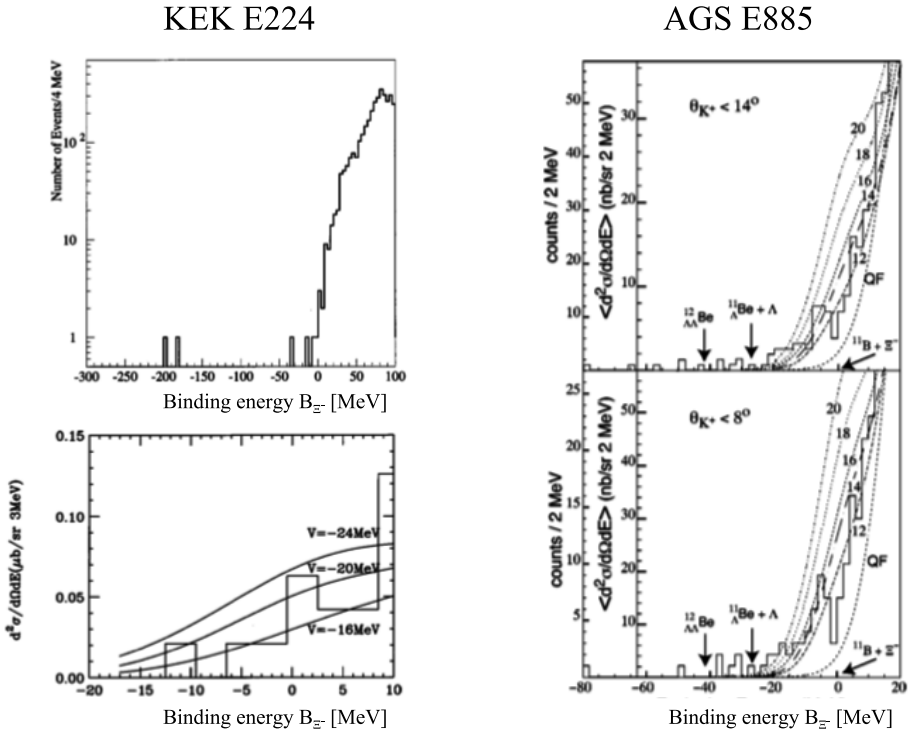

Figure 1.2: Missing mass spectra as a function of the binding energy of Ξ^- (B_{Ξ^-}) for ^{12}C(K^-, K^+)X reaction obtained in the KEK E224 [10] and AGS E885 [11].

1.2.3 Production of Ξ^--bound system using stopped Ξ^-

In the second way, a Ξ^- is produced by the (K^-, K^+) reaction, slows down, stops in material, then it is captured by an atomic orbit, and eventually absorbed by a nucleus. The Ξ^- atoms are in highly excited states and de-excite to lower states via Auger effect and X-ray emission before absorbed by a nucleus via the strong interaction process, $\Xi^- p \to \Lambda\Lambda$, then the nucleus is broken. Some of fragments end up with double-Λ hypernuclei or twin single-Λ hypernuclei. This process has been investigated by nuclear emulsion experiments. When the formed Ξ^- atom decays into two single-Λ hypernuclei (such an event is called "twin Λ hypernuclei"), the mass of the bound

Table 1.1: Theoretically predicted B_{Ξ^-} values of the Ξ^-N bound system [21].

state	B_{Ξ^-}[Ξ^--^{14}N] (MeV)
$1S$	5.93
$2P$	1.14
$3D$	0.174
$2S$	0.54
$3P$	0.28

(atomic) Ξ^- nucleus state is reconstructed from the masses and the kinetic energies of the two Λ hypernuclei. The binding energy of the $\Xi^-(B_{\Xi^-})$ can be obtained with 100-keV accuracy, which comes from a systematic error in the emulsion method. Experiments to search for $S = -2$ system using nuclear emulsion were performed at KEK (E176 [7], E373 [12]). The observed twin single-Λ and double-Λ hypernuclei were reported in [7] [13] [15] [16].

Here, the reported Ξ-bound systems are described. In KEK E176, two events of twin single-Λ hypernuclei were observed [13][14]. In these events, Ξ^- was considered to be captured by a light nucleus contained in the emulsion (^{12}C, ^{14}N, or ^{16}O) and then decayed into two Λ hypernuclei. One of them was identified as ${}^{4}_{\Lambda}$H. Considering the momentum balance with the ${}^{4}_{\Lambda}$H track, the range of the other hypernucleus was estimated and compared with the measured value. As a result, the process of

$$\Xi^- + {}^{12}\mathrm{C} \rightarrow {}^{4}_{\Lambda}\mathrm{H} + {}^{9}_{\Lambda}\mathrm{Be}$$

was concluded to be most probable. However, the possibility of $\Xi^- + {}^{14}$N or $\Xi^- + {}^{16}$O state cannot be ruled out due to momentum error of ${}^{4}_{\Lambda}$H, and thus the reaction was not identified uniquely.

In KEK E373, a twin single-Λ hypernuclei event named "KISO" was found [17]. For this event, the species of hyperfragments was identified and the process was uniquely determined as follows,

$$\Xi^- + {}^{14}\mathrm{N} \rightarrow {}^{10}_{\Lambda}\mathrm{Be} + {}^{5}_{\Lambda}\mathrm{He}.$$

As a result of the KISO event, B_{Ξ^-} was obtained to be 4.38 ± 0.25 MeV if the produced ${}^{10}_{\Lambda}$Be was in the ground state. However, the case that ${}^{10}_{\Lambda}$Be produced in excited states should be taken into account. Since there was no experimental data of exited stated of ${}^{10}_{\Lambda}$Be, theoretically calculated values using a cluster model [18] and a shell model [19] are used. The difference between the models was less than 200 keV. If ${}^{10}_{\Lambda}$Be is in the 2nd excited state, which is the highest bound excited state theoretically predicted, B_{Ξ^-} was estimated to be 1.11 ± 0.25 MeV.

Considering electromagnetic and strong interactions, the Ξ^- binding energy of the Ξ^--N system is theoretically predicted as shown in Table. 1.1. In this calculation, Ehime potential [21] is employed for the strong interaction. According to the theoretical calculation, the B_{Ξ^-} value for the $3D$ state is 0.174 MeV which is far from the experimental result. Assuming that ^{10}Be was in the 2nd excite state, the ${}^{10}_{\Lambda}$Be value of 1.11 MeV is consistent with the theoretically calculated B_{Ξ^-} of the $2P$ state, 1.14 MeV. They concluded that the Ξ^- could be absorbed from the $2P$ state

in the KISO event, although the theoretical calculation suggests that the probability of Ξ^- being absorbed from the $2P$ state is as small as a few %.

From the emulsion experiment, some of the Ξ^-bound systems were observed and they gave us important information that the ΞN interaction was attractive. Several theoretical models predict the Ξ-nuclear potential, but the difference in the Ξ^--binding energy depending on models is from hundreds eV to a few keV. The data of emulsion experiments which have at least 100-keV systematic errors cannot be used to discuss the Ξ-nuclear potential at sub-keV level. Thus, more accurate measurement with accuracy of at least a few hundreds eV is necessary to investigate the Ξ-nuclear potential in detail. We approach the Ξ-nuclear potential with a new experimental method, namely Ξ^- atomic X-ray spectroscopy.

1.3 X-ray spectroscopy of exotic atoms

The exotic atom and physical information given by its study are explained in this section. The previous research of an exotic atoms, especially of Σ^- atomic X-ray spectroscopy is introduced as an example. Then, the motivation and experimental concept of Ξ^- atomic X-ray spectroscopy are described.

1.3.1 Exotic atom

When a negatively charged particle (X^-) kicks off an electron in an atom and is captured by the atom, the exotic atom (X^- atom) is formed. This X^- deexcites to lower states with X-ray emission. The X-ray energy corresponds to an atomic level spacing which is related to the interaction between X^- and the nucleus describes as a potential, $U(r)$. When Coulomb interaction ($U_{Coul}(r)$) and the strong interaction ($U_{St}(r)$) work as a central force ($U(r)$), information on $U_{St}(r)$ can be extracted by subtracting the known $U_{Coul}(r)$ from $U(r)$. So far, research on the strong interaction using exotic atoms such as π^-, K^-, $\overline{p}$ and Σ^-, have been developed. Their properties summarized in PDG are listed in Table 1.2. When the typical stopping time in material is shorter than their life time, they from exotic atoms.

With the radial wave function for the X^- atom and the energy written as $\Phi(r)$ and E, respectively. The radial Schrödinger equation is given as

$$\left(-\frac{\hbar^2}{2\mu}\frac{d^2}{dr^2} + \frac{\hbar^2 l(l+1)}{2\mu r^2} + U(r)\right)\Phi(r) = E\Phi(r) \tag{1.1}$$

where $\Phi(r)$ is the wave function of the X^- atom. The reduced mass (μ) is defined as follows using the mass of X^- (m_{X^-}) and that of a core nucleus (m_N),

$$\mu = \frac{m_{X^-} m_N}{m_{X^-} + m_N}. \tag{1.2}$$

Table 1.2: Properties of negative particles summarized in PDG [2].

	mass [MeV]	lifetime [ns]	cτ [m]	Bohr radius [m] (Z=1)
e^-	0.511	∞	-	0.529×10^{-10}
π^-	140	26.0	7.8	1.93×10^{-13}
K^-	494	12.4	3.7	5.47×10^{-14}
$\overline{p}$	938	∞	-	2.88×10^{-14}
Σ^-	1197	0.148	0.044	2.26×10^{-14}
Ξ^-	1322	0.164	0.050	2.05×10^{-14}

By solving Eq. 1.1, the energy eigenvalues were obtained as a function of principal quantum number n. The orbital angular momentum l can take the values $l = 0, 1, \cdots, n-1$. An orbit where $l = n-1$ is called a circular orbit.

The energy shift and width

An atomic level is shifted and broadened due to the strong interaction compared to that with only Coulomb interaction considered. For the strong interaction potential $U_{St}(r)$, an optical potential is employed, $U_{St}(r) = V(r) + iW(r)$, and the real and the imaginary parts are written in $V(r)$ and $W(r)$, respectively. As an example, the energy levels for Ξ^--C bound system is shown in Fig. 1.3. It shows the schematic figure of the difference between the levels calculated only from Coulomb interaction (in dashed line) and from the Coulomb plus the strong interaction (in solid line) as the Ξ^--nuclear interaction. The difference between the two is called as the energy shift (ΔE) and is expressed with arrows. The shaded regions represent the width (Γ) of the state. The energy shift is given as

$$\Delta E = E^{n,l}_{Re(Coul.+St.)} - E^{n,l}_{Re(Coul.)} \tag{1.3}$$

$$= \langle \Phi^{n,l} | H_{kin} + U_{Coul} + V | \Phi^{n,l} \rangle - \langle \Phi'^{n,l} | H_{kin} + U_{Coul} | \Phi'^{n,l} \rangle \tag{1.4}$$

where $\langle \Phi^{n,l}|$ and $\langle \Phi'^{n,l}|$ are (n,l) eigenstates with and without the strong interaction, respectively. Note that the kinematical terms of Hamiltonian in Eq.1.1 are written in H_{kin},

$$H_{kin} \equiv -\frac{\hbar^2}{2\mu}\frac{d^2}{dr^2} + \frac{\hbar^2 l(l+1)}{2\mu r^2}. \tag{1.5}$$

The absorption means that a X^- reacts with a nucleon and produces another particles; it is expressed in the imaginary part of the optical potential. In the case of Ξ^-, Ξ^- is absorbed via the $\Xi^- p \rightarrow \Lambda\Lambda$ reaction. The width $\Gamma_{abs.}$ is related to the imaginary energy eigenvalue E_{Im} as $E_{Im} = -\frac{i}{2}\Gamma_{abs.}$. That is $\Gamma_{abs.}$ is given as

$$E_{Re} - \frac{i}{2}\Gamma_{abs.} = \langle \Phi^{n,l} | H_{kin} + U_{Coul} + U_{St} | \Phi^{n,l} \rangle \tag{1.6}$$

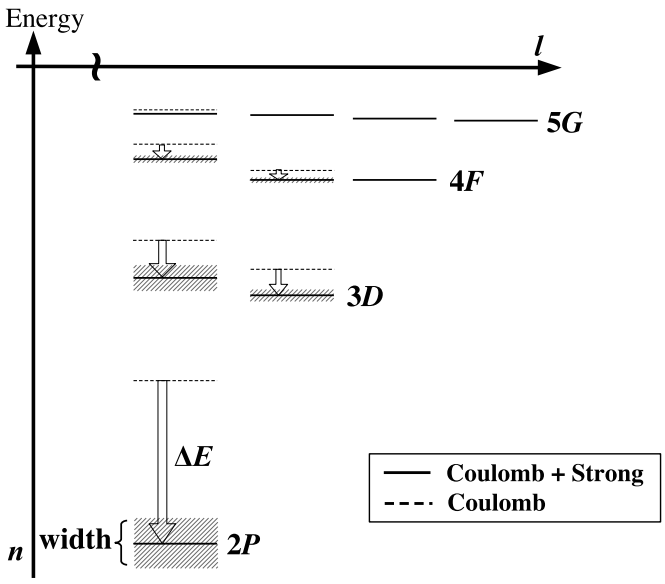

Figure 1.3: The schematic figure of the energy shift and width of Ξ^--C system.

The energy shift and width are obtained as a function of the overlap of the potential term and wave functions. The Wood-Saxon type potential is assumed and it is given as

$$U_{St}(r) = \frac{V_0 + iW_0}{1 + \exp\left(\frac{r-R}{a}\right)}, \tag{1.7}$$

where R is the nuclear radius, a is the diffuseness and V_0 and W_0 are the well depths of the real and imaginary potential. The wave functions with only Coulomb interaction for the circular orbit where $n = 1$ to 5 and the Woods-Saxon type nuclear potential with V_0 is 15 MeV and W_0 is 1.5 MeV are shown in Fig. 1.4. In Fig. 1.4, the potential with a 15-MeV well depth is shown.

Where r is small enough, the centrifugal force is much larger than $U(r) - E(r)$ and Eq.1.1 is approximated as

$$-\frac{\hbar^2}{2\mu}\frac{d^2\Phi(r)}{dr^2} + \frac{l(l+1)\hbar^2}{2\mu r^2}\Phi(r) \cong 0. \tag{1.8}$$

The wave function of X^- atom near the nucleus behaves as $\sim r^l$. Therefore, the wave function and the potential overlap more for the lower l. The more overlap between a wave function and the nuclear potential results in the larger energy shifts and width. This shift and width are especially sensitive to the shape of the potential near the surface of the nucleus.

$E1$ transition and absorption

When a X^- is captured by an atomic orbit, it is more likely to be captured by larger l orbits among the same n orbits. The levels of the X^-C atomic orbits are shown in Fig. 1.5. Arrows represent

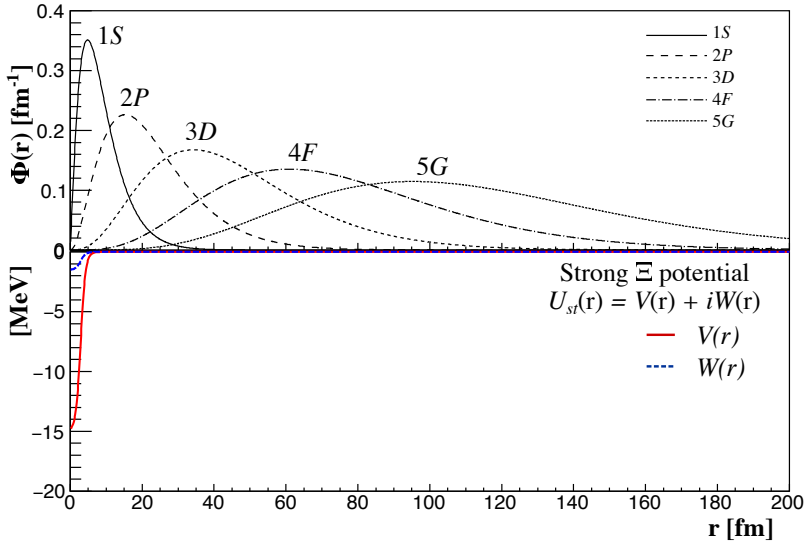

Figure 1.4: The wave functions of C atom with only Coulomb interaction are shown in top. The strong Ξ potential $U(r)$ is shown bottom, real part $V(r)$ and imaginary part $W(r)$ are shown in a solid red line and a dashed blue line, respectively.

$E1$ transitions and absorption. Small overlaps between a wave function of $5G$ state and the strong Ξ^- potential, and Coulomb interaction is dominate. Most of Ξ^- $E1$ transitions, satisfying $\delta l = 1$, and $n_f < n_i$.

The X^- in the atomic state (n_i, l_i) de-excites to a lower orbit (n_f, l_f) with X-ray emission. In the state with a large l, the wave function is pushed out as shown in Fig. 1.4, and Coulomb interaction dominates ($\Gamma_{abs.} \ll \Gamma_{E1}$). $E1$ transitions satisfying $\delta l = l_f - l_i = 1$ and $n_f < n_i$ are dominant. Thus, the X^- tends to occupy the circular orbits after several $E1$ transitions are repeated. In this thesis, we discuss transitions between the circular orbits only, otherwise noted. After $E1$ transitions, the X^- enters the inner orbit, the (n, l) state in Fig. 1.5, and the strong interaction works similarly to Coulomb interaction ($\Gamma_{abs.} \approx \Gamma_{E1}$). In this region, in addition to the deexcitation to the $(n-1, l-1)$ state by the $E1$ transition, the X^- is absorbed by a nucleus due to the strong interaction. In the inner orbits of the $(n-1, l-1)$ state, the nuclear absorption is much more dominant than the $E1$ transition ($\Gamma_{abs.} \gg \Gamma_{E1}$), and thus the X^- is absorbed by a nucleus with a large probability. The $(n, l) \to (n-1, l-1)$ transition, just before the absorption shown in a blue arrow, is called the "last transition". The $(n-1, l-1)$ orbit is called the last orbit. In this thesis only, a transition $(n+1, l+1) \to (n, l)$ before the last transition is called the "preceding transition". To measure X rays of the last transition is most effective since the lower l state is, the more affected by the strong interaction.

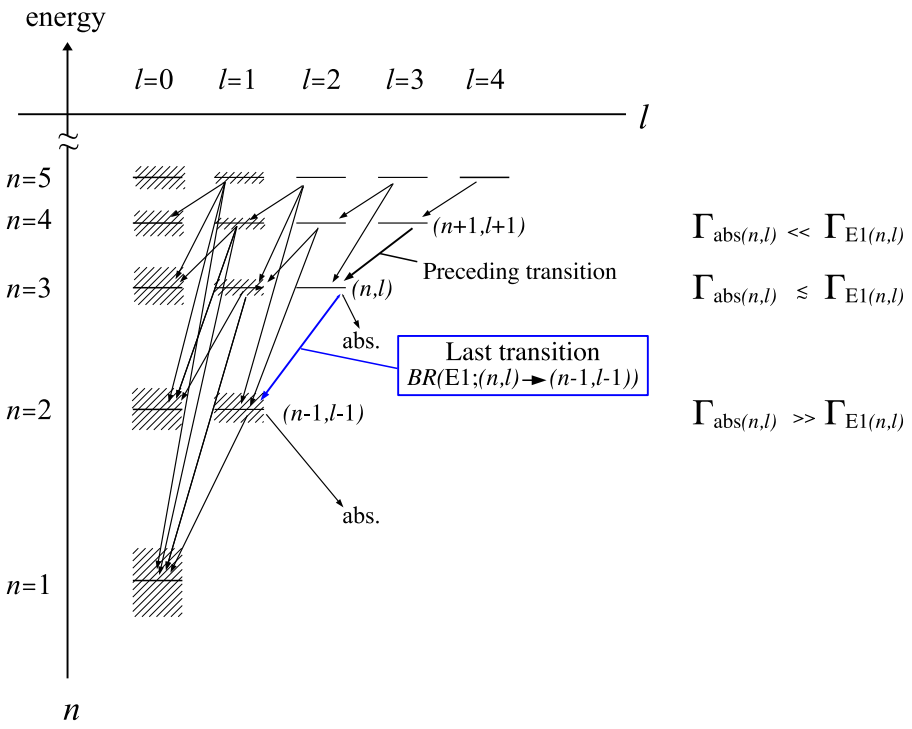

Figure 1.5: The energy levels of a X^- atom and dominant transitions.

Branching ratio

The probability for the X^- in the (n_i, l_i) state to de-excite to the (n_f, l_f) state is defined as the branching ratio $BR(E1; (n_i, l_i) \to (n_f, l_f))$. When a Ξ^- atom undergoes a transition from the (n_i, l_i) state to the (n_f, l_f) state, both of the electromagnetic and the strong interaction contribute. The branching ratio of the $E1$ transition, denoted as $BR(E1; (n_i, l_i) \to (n_f, l_f))$, is given as

$$BR(E1; (n_i, l_i) \to (n_f, l_f)) = \frac{w(E1)}{w(E1) + w(abs)} \tag{1.9}$$

$$= \frac{\Gamma_{E1}^{(n_i,l_i)\to(n_f,l_f)}}{\Gamma_{E1}^{(n_i,l_i)\to(n_f,l_f)} + \Gamma_{abs}^{(n_i,l_i)}} \tag{1.10}$$

where $w(E1)$ is the transition probability of $E1$, $w(abs)$ is the probability of absorption by the nucleus due to the strong interaction. The probability w is proportional to the width, that is $\Gamma_{E1} = w(E1)\hbar$ and $\Gamma_{abs} = w(abs)\hbar$. BR is given as a function of the width as shown in Eq. 1.10. The total width of a state, Γ, is given as $\Gamma = \Gamma_{E1} + \Gamma_{abs}$.

The ratio of the number of X^-s which finally reach the (n, l) orbit to the total number of Ξ^-s captured in the atom is written as $P_{\Xi(n,l)}$. When the $E1$ transition is dominant ($\Gamma_{abs} \ll \Gamma_{E1}$), that is, most of all orbits above the last orbit, the $P_{\Xi(n,l)}$ can be essentially calculated only from Coulomb interaction.

As a notation representing a transition, for example, the $(3,2) \rightarrow (2,1)$ transition is also expressed as $(3D \rightarrow 2P)$.

1.3.2 Previous X-ray measurements of exotic atoms

For exotic atoms with the particles listed in Table 1.2 expect for Ξ^-, X-ray measurements have been performed. Among them, the characteristics of Σ^- atom is similar to and Ξ^- atoms. The lifetime of hyperons, Σ^- and Ξ^-, is as short as $\sim$150 ps while that of π^-, K^- is of the order of 10 ns. The small yield of exotic atoms with negative hyperons due to their short lifetimes makes X-ray measurement difficult. In addition, the mass of Σ^- hyperon is 1197 MeV/c^2 which is not very different from Ξ^- hyperon.

In the past, Σ^- atomic X-ray spectroscopy experiments were performed using stopped K^- beams at CERN [24], RAL [25] and BNL [26]. A stopped K^- is absorbed in material followed by Σ^- production as follows,

$$\begin{aligned} K^- + p &\rightarrow \Sigma^- + \pi^+ \\ K^- + n &\rightarrow \Sigma^- + \pi^0 \\ K^- + p + n &\rightarrow \Sigma^- + p. \end{aligned}$$

X rays were measured by Ge detectors with resolution of $0.6 \sim 0.7$ keV (σ) at 120 keV in coincidence with the stopped K^-. The obtained results are listed in Table 1.3.

Table 1.3: The result of the past Σ^- atomic X-ray measurements.

Target	Z	Transition $n+1 \rightarrow n$	Electromagnetic energy [keV]	Measured energy [keV]	Shift (ΔE) [eV]	Width(Γ_n) [eV]	Γ_{n+1} [keV]	ref.
C	6	4→3	50.68	50.65±0.02			0.031±0.012	[24]
Ca	20	6→5	152.07	151.66±0.29			0.408±0.223	[24]
Ti	22	6→5	185.02	185.41±0.20			0.649±0.422	[24]
Ba	56	9→8	327.58	326.72±0.50			2.925±3.475	[24]
O	8	4→3	92.437	92.76±0.23	320±230	-	$1.0^{+1.7}_{-0.4}$	[25]
Mg	12	5→4	98.748	98.77±0.04	25±40	<70	0.11±0.09	[25]
Al	13	5→4	116.508	116.576±0.028	68±28	43±75	0.24±0.06	[25]
Si	14	5→4	135.403	135.56±0.04	159±36	220±110	0.41±0.10	[25]
S	16	5→4	177.921	178.28±0.22	360±220	870±700	1.5±0.8	[25]
Pb	82	10→9	504.899	505.321±0.048	422±65	428±158	17±3	[26]
W	74	10→9	410.901	411.115±0.053	214±60	18±149	2±2	[26]

According to Ref. [27], the Σ^- atomic X-ray data were best fitted by the phenomenological density dependent potential. It is suggested that the Σ^--nuclear potential has a shallow attractive pocket at just outside a nucleus and a repulsive core inside the nucleus. However, the Σ^- atomic X-ray data allow for several potential shapes inside the nucleus.

Sigma-nucleus potential was investigated with the reaction spectroscopy experiment [4]. From the result of this experiment, a real part of the Σ^--nuclear potential was found to be strongly repulsive. Taking into account the repulsive Σ-nuclear potential, it is suggested that neutrons convert to Σ hyperons under much higher density compared to Λ hyperons inside neutron stars.

As shown in the research on Σ-nuclear interaction, the X-ray spectroscopic experiment and the reaction spectroscopic experiment To investigate the potential at inside and the surface of a nucleus, both of two experimental methods are important.

1.4 The motivation of this research

The purpose of this research is to measure Ξ^- atomic X-rays and to obtain information on the Ξ^--nuclear potential. For the future experiments, evaluation of detection sensitivity and measurement accuracy are important to establish the experimental method.

To obtain information on the Ξ^--nuclear potential by measuring X rays, a clean spectrum, with a good signal to noise ratio is necessary. Since the lifetime of Ξ^- is as short as 164 ps, most of the Ξ^-s decay before stopping and make a huge background. The main decay mode of Ξ^- is $\Xi^-\rightarrow\Lambda\pi^-$ (branching ratio 99.9%). Λ decay as $\Lambda \rightarrow n\pi^0$ followed by a π^0 decay to 2γ, and make background. On the other hand, when Λ decay as $\Lambda \rightarrow p\pi^-$, the produced π^-s hit surrounding material, π^-+A$\rightarrow$ n+X /γ+ X', and make background γ rays, Also, a high energy π^- makes background γ rays.

In addition to the small cross section of Ξ^- production, these huge background make it difficult to measure X rays of Ξ^- atoms. Tagging Ξ^- stop events is a key to overcome these difficulties for and successful measurement of X rays. Two methods for selecting Ξ^--stop events were developed and studied to see whether Ξ^- atomic X rays were measured with sufficient accuracy.

1.4.1 Method 1: Emulsion image method

A tracking detector for Ξ^- is useful to identify the Ξ^--stop events. The experiment to search for double-Λ hypernuclei using nuclear emulsion was planned (J-PARC E07[28]). E07 was designed to obtain 10 times the statistics, that is 10^4 Ξ^--stop events, than the KEK E373 experiment in which the first double-Λ hypernucler event (NAGARA [15]) was discovered. The target for Ξ^- production and the detectors were designed so that the produced Ξ^- stops in the emulsion with a large probability. Thus, we planned to measure Ξ^- atomic X rays simultaneously since it is possible to select Ξ^--stop events cleanly using this emulsion as a Ξ^- tracking detector. Selecting Ξ^--stop events by the emulsion image analysis is called the emulsion image method in this thesis. The Ξ^- atoms of C, N, O, Br, and Ag contained in the emulsion were produced. By X-ray measurement in coincidence with the Ξ^- stop image, the Ξ^- atomic X-ray spectra can be obtained, especially of the Ξ^- Ag, and Ξ^- Br atoms, with almost background free condition.

The last transition of Ξ^- Ag and Ξ^- Br atoms are assumed as Ag($8J \to 7I$) and Br($7I \to 6H$), respectively. The energy shift and width of their X rays were predicted by assuming two types of the potential, the tρ potential and the Nijmegen D (ND) potential, as shown in Table. 1.4. The $t\rho$ potential [27] is an optical potential which is proportional to a nuclear density distribution $\rho(r)$ and given as

$$V_{opt}(r) = -\frac{4\pi}{2m}(1 + \frac{m}{M})b_0\rho(r) \tag{1.11}$$

where m is the Ξ^--nucleus reduced mass, M is the mass of the nucleon, $\rho(r)$ is the nuclear density, and b_0 is the complex parameter of the hadron-nucleon scattering length. The $t\rho$ potential which is corrected to have a 14-MeV depth is shown in red in Fig. 1.6. On the other hand, ND potential is calculated based on one-boson exchange model [20]. It is shown in blue in Fig. 1.6, and it is adjusted so that its averaged depth reproduces 14 MeV. The expected shift is of the order of keV although they vary depending on the model.

Table 1.4: The theoretically predicted shift and width for the last transition of Ξ^- Ag and Ξ^- Br atoms [22].

transition	potential	X-ray energy [keV]	shift [keV]	width [keV]
Ag($8J \to 7I$)	$t\rho$	370.45	0.28	0.15
	ND		3.3	0.79
Br($7I \to 6H$)	$t\rho$	315.5	0.73	0.44
	ND		5.5	1.74

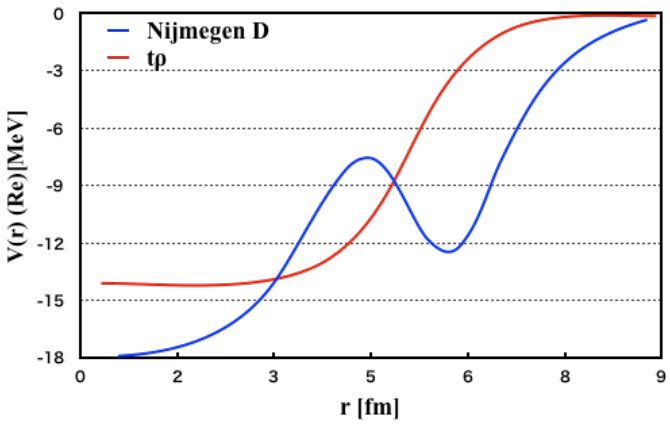

Figure 1.6: The Ξ^--nucleus potential expected with two types of theoretical model, the $t\rho$ potential shown in red [27] and the Nijmegen D (ND) type potential shown in blue [20].

Requirements for an experiment

The detectors were designed for Ξ^-Ag and Ξ^-Br atomic X-ray measurement. The X-ray yield of the Ag($8J \to 7I$) transition was estimated as

$$Yield(N_{Xray}) = N_{\Xi capture}(\mathrm{Ag}) \times P_{\Xi(8J)} \times BR(E1; 8J \to 7I) \times \epsilon_{detector} \tag{1.12}$$

where $N_{\Xi capture}$(Ag) is the number of Ξ^-s captured by Ag atoms, $P_{\Xi(8J)}$ is the ratio that captured Ξ^-s deexcite to the $8J$ state and $\epsilon_{detector}$ is the efficiency of a X-ray detector. The statistical error ($\sigma_{stat.}$) and systematic error ($\sigma_{sys.}$) should be small enough to determine the X-ray energy with accuracy of a few hundreds eV. The number of Ξ^--stop events depended on the amount of the emulsion and 3600 Ξ^-s were estimated to be captured by Ag atoms in this experiment. A value of 0.6 estimated from the past Σ^- atomic X-ray measurement was employed as P_Ξ [23]. The $\sigma_{stat.}$ depends on the X-ray yield and the energy resolution of X-ray detector $\sigma_{det.}$ as $\sigma_{stat.} = \sigma_{det.}/\sqrt{N_{Xray}}$. Germanium (Ge) detectors were employed due to their good energy resolution of $\sim$2 keV (FWHM) at 400 keV. Then, the systematic error was required to be comparable to the statistical error, which is around $\sim$ 200 eV from an expected value of N_{Xray}. When, roughly estimated, $N_{\Xi capture}$ (Ag) is 3600, P_Ξ is 0.6, $BR(E1; 8J \to 7I)$ is $\sim$0.9, and the Ge detector efficiency is 1%, and then the yield is N_{Xray} $\sim$20 counts.

1.4.2 Method 2 : Kinematical method

In the method 1, only atoms included in the emulsion are used for Ξ^- atoms. To develop a systematic study of Ξ^- atomic X rays, by measuring mass (A) dependence of the energy shift, the method other than method1 is necessary. One of the possible methods is to select Ξ^--stop events using kinematical information of Ξ^- obtained from reaction analysis. This method, called the kinematical method in this thesis, was also studied and applied as a byproduct. Since a diamond target was used, Ξ^-C atomic X rays were studied in this experiment. The levels of Ξ^-C atom is shown in Fig. 1.7. Since the energy range of the Ge detectors for the X-ray measurement is higher than $\sim$100 keV, the ($3D \to 2P$) transition whose energy is 154 keV considering only the Coulomb interaction can be measured. The shift and width are possibly as large as hundreds of keV since the $3D$ orbit is considered as the last orbit of Ξ^-C atom. Thus, X rays should be searched for over a wide region. When it is not observed as an evident peak, the branching ratios of $BR(E1; 3D \to 2P)$ and $BR(abs.; 3D)$ will be discussed based on the X-ray yield.

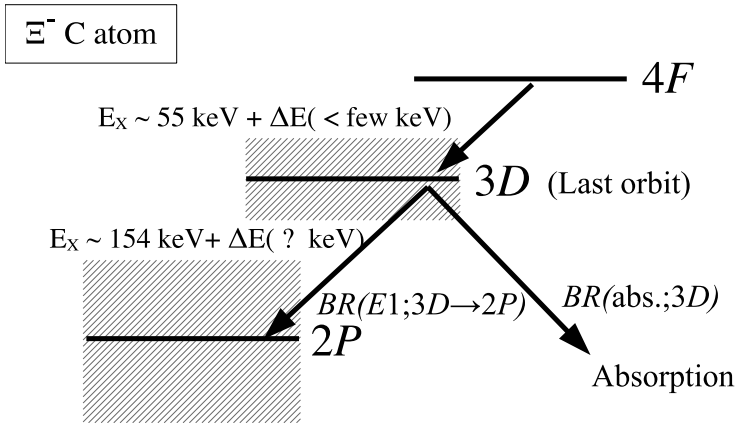

Figure 1.7: The levels of Ξ^-C atom.

Chapter 2

Experiment

In this section, the first Ξ^- atomic X-ray spectroscopy experiment (J-PARC E07) performed at J-PARC, Japan Proton Accelerator Research Complex, in 2016 and 2017 is described.

2.1 Overview

The experiment was originally planned to search for double-Λ hypernuclei and designed based on the concept of identifying hypernuclei by emulsion image analysis. The process from production of a Ξ^- particle to form the hypernuclei is shown in Fig. 2.1. The Ξ^- produced via the (K^-, K^+) reaction at a reaction target is injected to the emulsion, and some of them are stopped there. Then, they are captured by atoms and form Ξ^- atoms. The captured Ξ^- de-exicites to lower atomic orbits with X-ray emission, and, at the end, the Ξ^- is absorbed by the nucleus, that is, the Ξ^- reacts with a proton as $\Xi^- p \rightarrow \Lambda\Lambda$ and the nucleus is break up to fragments. Sometimes a double-Λ hypernucleus, or one or two single-Λ hypernuclei are produced as fragments, and sometimes produced Λs not bound to the nucleus and mesonic decay as $\Lambda \rightarrow p\pi^-$ or $\Lambda \rightarrow n\pi^0$. The Λ inside a nucleus decays as $\Lambda p \rightarrow pn$ or $\Lambda n \rightarrow nn$. If one or more charged fragments are produced, one or more charged tracks are observed at the stopping point of Ξ^- as shown in (a) of the figure and they are called "σ-stop" events. On the other hand, the events in which no tracks are observed at the stopping point of Ξ^- except tracks of Auger electrons as shown in (b) are called "ρ-stop" events. By selecting σ- and ρ-stop events, the events of Ξ^- atom production are identified cleanly. This method allows us to measure X rays of Ξ^- atom, which contains in the emulsion such as Ag and Br, with a good S/N ratio.

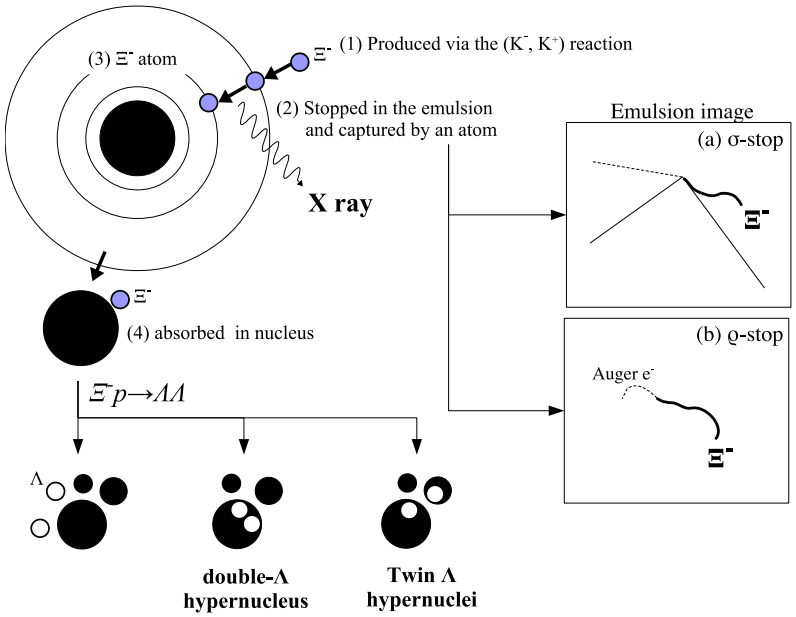

Figure 2.1: The process of the double-Λ hypernuclear production.

The (K^-, K^+) reaction cross section is maximum at the incident K^- momentum of 1.8 GeV/c [9]. The K1.8 beam line at J-PARC was designed to supply K^- beam of 1.8 GeV/c momentum for experiments using the (K^-, K^+) reaction. Thus, the present experiment was performed using this facility.

A diamond target was used as the Ξ^- production target, and it was also used as an energy degrader for the produced Ξ^-. The slowed down Ξ^- passed through the target, then reached the emulsion placed downstream of the target, and stopped in it. To obtain information on where the Ξ^- arrived at the surface of the emulsion, the Ξ^- track was measured by silicon strip detectors (SSD) placed sandwiching the emulsion. The prediction on the Ξ^- hit position given by SSD made time shorter to search for the Ξ^- track in the emulsion image analysis. This is called the emulsion-counter hybrid method. The experiment was designed to obtain 1×10^4 Ξ^- which was 10 times that obtained in the past experiment, KEK E373 [16].

For the identification of the (K^-, K^+) reaction, two magnetic spectrometers were used. The magnetic spectrometers were not necessary to have a high momentum resolution because the reaction was identified by K^- and K^+ tracks as well as the Ξ^- track analyzed by SSD. In addition to that, the production of hypernuclei was cleanly identified by emulsion image analysis. The important requirement was to detect the scattered K^+ with large efficiency. Thus, KURAMA spectrometer with a large acceptance of 280 msr was used for the scattered K^+. The incident K^- beam was analyzed by the K1.8 beam line spectrometer which was optimized to measure K^- around 1.8 GeV/c and had been also used in the past experiments.

For measurement of Ξ^- Ag and Ξ^- Br atomic X rays for the last transition, $300 - 400$ keV, germanium (Ge) detectors were employed. To achieve high-precision measurement with a system-

atic error as small as a statistical error of ∼150 eV, a new developed in-beam energy calibration system was employed.

2.2 J-PARC and the K1.8 beam line

J-PARC, Japan Proton Accelerator Research Complex, is the proton synchrotron facility located at Tokai, Ibaraki. In this facility, primary protons are accelerated in every 5.5 seconds and supplied to the experimental facility (Hadron hall) during a period (called "spill") of 2.2 seconds. In the present experiment, 4.3×10^{13} protons per spill were accelerated with 37-kW operation and were irradiated to a primary gold target. The dimension of the primary target was 15 mm (horizontal) × 11 mm (vertical) × 66 mm (thickness). Many species of produced secondary beams such as K, π, ν and μ are available, and we used a secondary K^- beam of 1.8 GeV/c momentum in this experiment. As shown in Fig. 2.2, it was transported to the K1.8 area through the K1.8 beam line consisting of several magnets of dipole (D1-D4), quadrupole (Q1-Q13), sextapole (S1-S4), and octapole (O1-O2). Momentum of the particle was selected by the dipole magnets and the momentum slit. To reject contamination of other secondary particles, mainly π^-, two electrostatic separators (ESS1,2) and mass slits (MS1, 2) were used. The ESS1 and ESS2 were operated by applying ±250 kV to a 10-cm gap. The trajectories of beam particles were different according to their velocities when an electric field by the electrostatic separators was applied together with a magnetic field. The position and width of the mass slits located downstream of each electrostatic separators were adjusted to select K^-. In our data-taking period, 280×10^3 K^- and 60×10^3 π^- per spill were transported to the experimental target at the K1.8 area. The ratio of K^- and π^- particles contained in the beam was 4:1. The beam profile of x (horizontal) and y (vertical) directions are shown in Fig. 2.3 and Fig. 2.4, respectively. The momentum bite was ±3% and momentum resolution ($\delta p/p$) was 3.3×10^{-4} (FWHM). Detail information is given in elsewhere [29].

2.3 Target

The cross section of the (K^-, K^+) reaction is reported to be proportional to $A^{0.38}$ [6] but the produced Ξ^- is absorbed in nuclei particularly with a large Z. To stop the produced Ξ^- in the emulsion located downstream of the target, the target was also used as a degrader. Thus, a diamond target was employed since it has a high density. Size of the target was $5.06^x \times 3.03^y \times 3.04^z$ cm^3 and its density was 3.24 g/cm^3 and thickness was 9.85 g/cm^2.

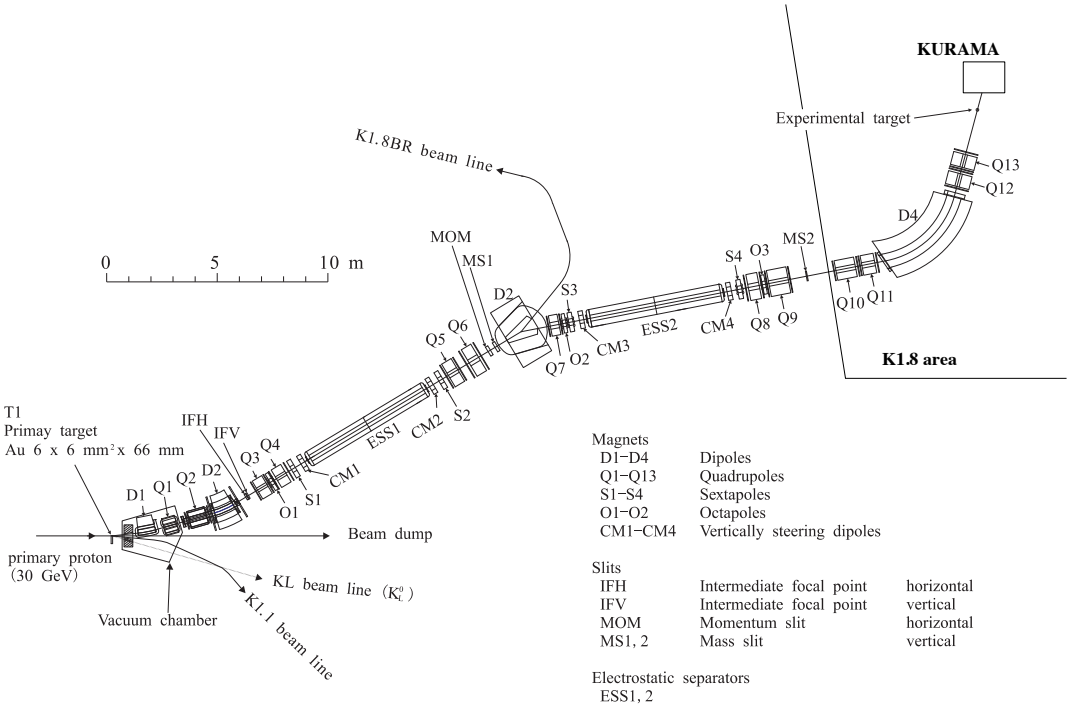

Figure 2.2: The schematic view of K1.8 beam line.

2.4 Reaction spectrometers

2.4.1 Beam line spectrometer

To identify K^- beam and analyze its momentum, the K1.8 beam lime spectrometer which consists of QQDQQ magnets, trigger counters, and tracking detectors were used. The schematic view of the K1.8 beam line spectrometer is shown in Fig. 2.5. To identify the incident beam, two hodoscopes (BH1, BH2) were placed, one was upstream of the magnets and the other was downstream. To reject contamination of π^- beam at the trigger level, aerogel Cherenkov detectors (BAC1, BAC2) were used. For the selection of K^-, time-of-flight between BH1 and BH2 were measured. For momentum analysis, the beam position upstream of the magnets and the beam track downstream of the magnets were measured by the beam fiber detector (BFT) and drift chambers (BC3, BC4), respectively. From the information on the magnetic field of the magnets of QQDQQ, the transfer matrix was calculated by TRANSPORT code[1]. The specifications of detectors of the beam line spectrometer are summarized in Table. 2.2, and they are explained below. Main specifications of this spectrometer are shown in Table 2.1.

[1]the program for calculating particle transport based on the beam line optics

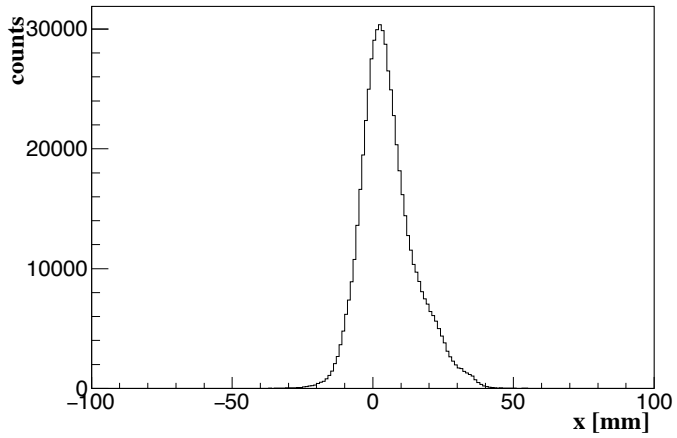

Figure 2.3: Beam profile in x direction at the experimental target.

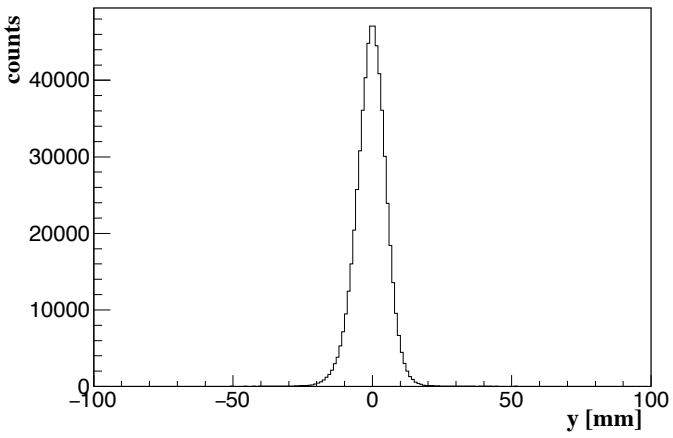

Figure 2.4: Beam profile in y direction at the experimental target.

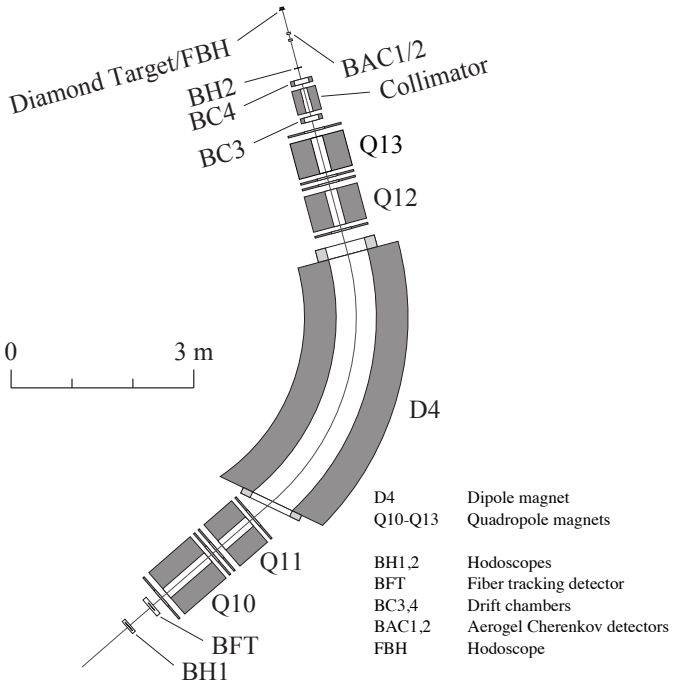

Figure 2.5: The schematic view of the K1.8 beam line spectrometer.

Table 2.1: Main specification of the beam line spectrometer

Momentum resolution	3.3 $\times 10^{-4}$ (FWHM)
Maximum momentum	2.0 [GeV/c]
Central momentum	1.8 [GeV/c]
Momentum bite	± 3[%]
Bending angle	64 [deg]
Flight length between BH1 and BH2	11.2 [m]

Table 2.2: The specifications of detectors of beam line spectrometer.

Hodoscope	effective area [mm^2]	thickness [mm]	segment	Readout
BH1	$170^x \times 66^y$	5	11	3/4" PMT ; H6524MOD, both ends
BH2	$120^x \times 40^y$	60	1	2" PMT ; H10570, both ends
FBH	$82.5^x \times 30^y$	2	16	MPPC w/ wave length shifting fiber, both ends

Aerogel Cherenkov	effective area [mm^2]	thickness [mm]	index	Readout
BAC1, 2	$170^x \times 70^y$	46	1.03	3" PMT ; R6683

Fiber tracker	effective area [mm^2]	fiber	Readout
BFT	$160^x \times 80^y$	KURARAYSCSF-78M $\phi = 1$ mm	MPPC

Drift chamber	effective area [mm^2]	plane	title angle [deg] anode-anode	wire pitch [mm] anode-cathode	
BC3	$192^x \times 100^y$	$xx'vv'uu'$	$0, -15, +15$	3	2
BC4	$192^x \times 100^y$	$uu'vv'xx'$	$+15, -15, 0$	3	2

Trigger Counters

BH1, BH2

As trigger counters for beam particles, two Beam Hodoscope (BH1, BH2) were used. BH1 was located upstream of the Q10 magnet of the beam spectrometer as shown in Fig. 2.5. It consists of horizontally-segmented 11 slabs of plastics scintillator (BC420) with 5 mm thickness and effective area was $170^x \times 66^y$ mm^2. Scintillation light was collected on photo-multiplier tubes (PMT) attached to both ends. BH2 was located downstream of the drift chamber (BC4) as shown in Fig. 2.5. It consists of a plastic scintillator (Eljen Technology EJ-212) with dimension of $120^x \times 40^y \times 60^z$ mm^3. Acrylic light guides and PMTs were attached to both ends of the scintillator. BH2 was used as a reference timing counter for all the other detectors. In addition, time-of-flight between BH1 and BH2 was measured in order to reject contaminating π^-.

FBH

Fine Beam Hodoscope (FBH) was located just upstream of the target. It consists of horizontally-segmented 16 slabs of plastic scintillator (EJ-212) of 2 mm thick with wave length shifting fibers (Kuraray PSFY-11J). The size of each segment was $7.5^x \times 35^y$ mm^2, and the whole effective area was $82.5^x \times 30^y$ mm^2. The scintillator slabs were placed with 2.5 mm overlap to each other as shown in Fig. 2.6. Emitted scintillation light was collected by MPPC -Multi-Pixel Photon Counter- (Hamamatsu S12571-100P) with 1 mm×1 mm size through the wave length shifting fiber. Signals from MPPCs were read out using the EASIROC boards. FBH was used as one of the trigger counters for the 2D Matrix trigger to be described in section 2.4.3.

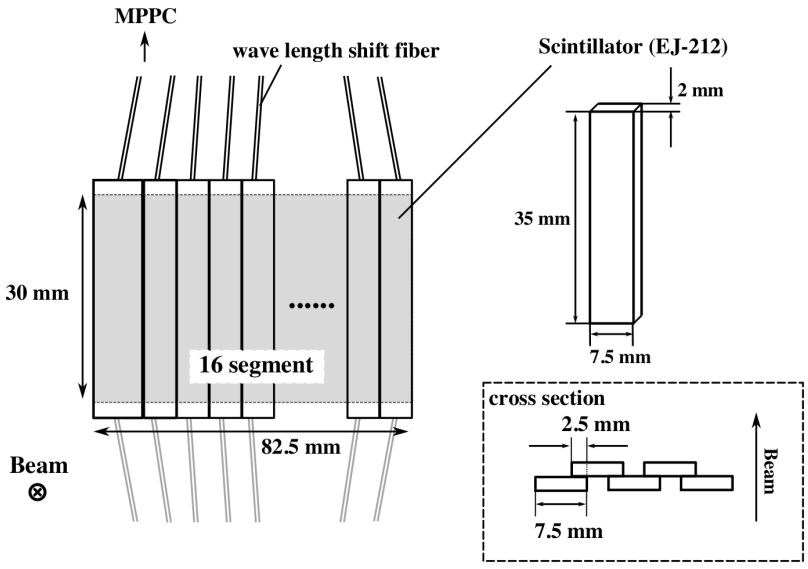

Figure 2.6: The schematic drawing of FBH.

BAC1, BAC2

To reject contaminating π^- beam of 1.8 GeV/c, Beam Aerogel Cherenkov counter (BAC) was placed upstream of FBH. In aerogel of refractive index (n), Cherenkov light was emitted when the velocity of particle exceeds the light speed in the material ($\beta c > c/n$). The correlation between momentum and β for K^- and π^- are plotted in Fig. 2.7. Aerogel with index $n = 1.03$ was employed for BAC to distinguish an incident K^- and π^- with 1.8 GeV/c momentum. Only a π^- passing through the radiator emitted Cherenkov light, but not K^-. The radiator was wrapped with a teflon sheet and shielded with a black sheet. Emitted Cherenkov light was collected by fine-mesh type PMTs with 3" diameter (Hamamatsu R6683).

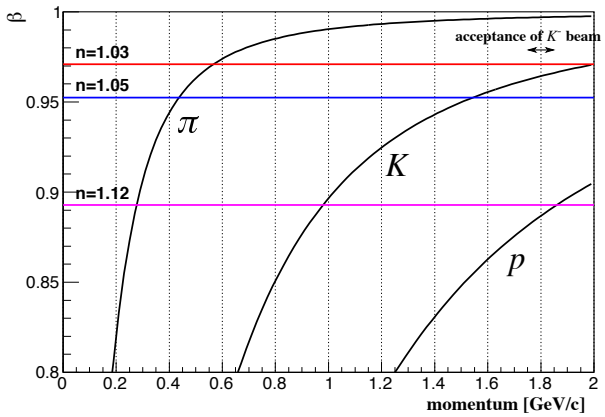

Figure 2.7: The relation between momentum and beta.

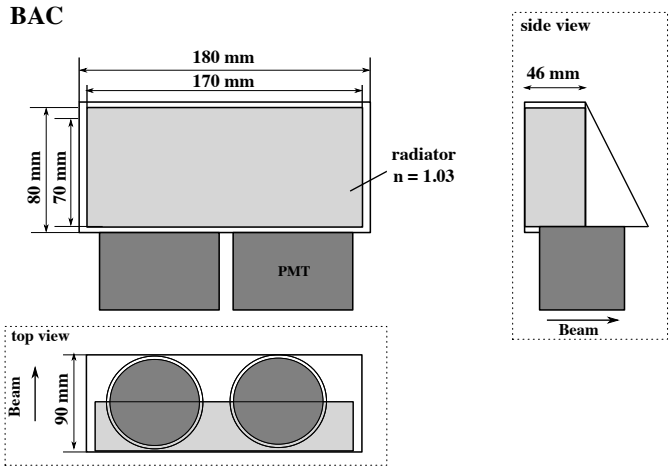

Figure 2.8: The schematic drawing of BAC.

Tracking detectors

For momentum analysis of the K^- beam, the beam position and angle at upstream and down stream of the magnets (QQDQQ) were measured using a fiber detector (BFT) and drift chambers (BC3, BC4).

BFT

Scintillation fiber detector (BFT) [30] was located upstream of the Q10 magnet to measure the x position of the incident beam particle. BFT consists of 320 horizontally-aligned fibers with 1 mm diameter. Two layers of fibers were stacked as shown in Fig. 2.9 to increase detection efficiency. The effective area was $160^x \times 80^y$ mm^2. A multi photon pixel counter (MPPC) attached to one end of each fiber collects scintillation light. The timing resolution (σ_t) was 0.8 ns and the position

resolution (σ_{pos}) was 0.2 mm. Note that only x position of the beam particles was measured at upstream of the magnets.

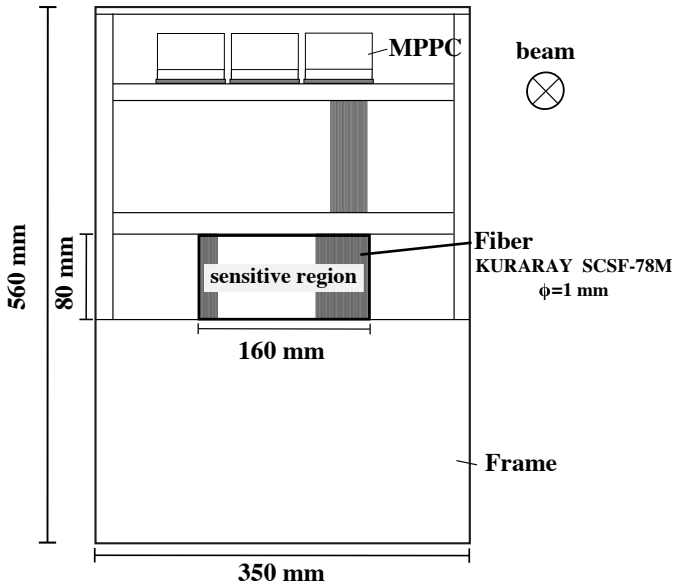

Figure 2.9: The schematic drawing of BFT.

BC3, BC4

Two multi-wire drift chambers (BC3, BC4) were located at the downstream of the Q12 magnet. A schematic drawing of BC3,4 is shown in Fig. 2.10. Both of them had 6 layers of sense-wire plane ($xx'uu'vv'$). The u and v planes were inclined to $+15$ and -15 degrees, respectively, with respect to the x plane. The wire spacing was 3 mm, and the distance between the wire and the cathode plane was 2 mm. Mixed gas of Ar (76%) and iso-C_4H_{10} (20%) was flown in to the chambers. In addition, $C_3H_8O_2$ (4%) was mixed. A typical position resolution (σ) was 0.2 mm.

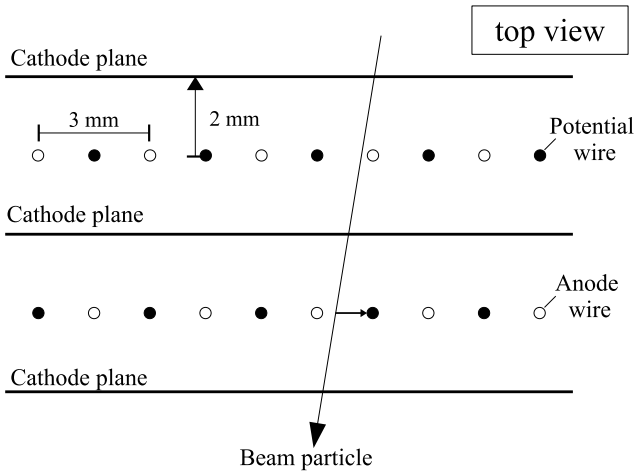

Figure 2.10: Top view of BC3, BC4.

2.4.2 Reaction spectrometer : KURAMA

To measure the scattered K^+, a magnetic spectrometer, called KURAMA, was placed downstream of the target. To identify Ξ^- particles, not only reaction analysis by the magnetic spectrometers but also information of emulsion image analysis were used. Thus, we used the KURAMA spectrometer with a large solid angle of 280 msr in favor of higher acceptance than good resolution. The main specifications of the KURAMA spectrometer are shown in Table 2.3.

Table 2.3: Main specification of KURAMA spectrometer

Momentum resolution ($\delta p/p$)	2.8 $\times 10^{-2}$ (FWHM)
Gap size	80 [cm]
acceptance (solid angle)	280 [msr]
magnetic field	0.76 [T]

The schematic view is shown in Fig. 2.11. It consists of a dipole magnet, trigger counters, and tracking detectors. Scintillation hodoscopes (SCH, TOF) were used as trigger counters and TOF measured time-of-flight between BH2 and TOF. To reject low-momentum protons and pions emitted forward, Aerogel Cherenkov detectors (PVAC, FAC) were used as trigger counters. The particle tracks were reconstructed by drift chambers (SCD1, SDC2, SDC3), SCH and SSD described below. The scattered particles were identified by the mass calculated by the time-of-flight, the path length, and the momentum. The specifications of detectors of the KURAMA spectrometer are summarized in Table. 2.4.

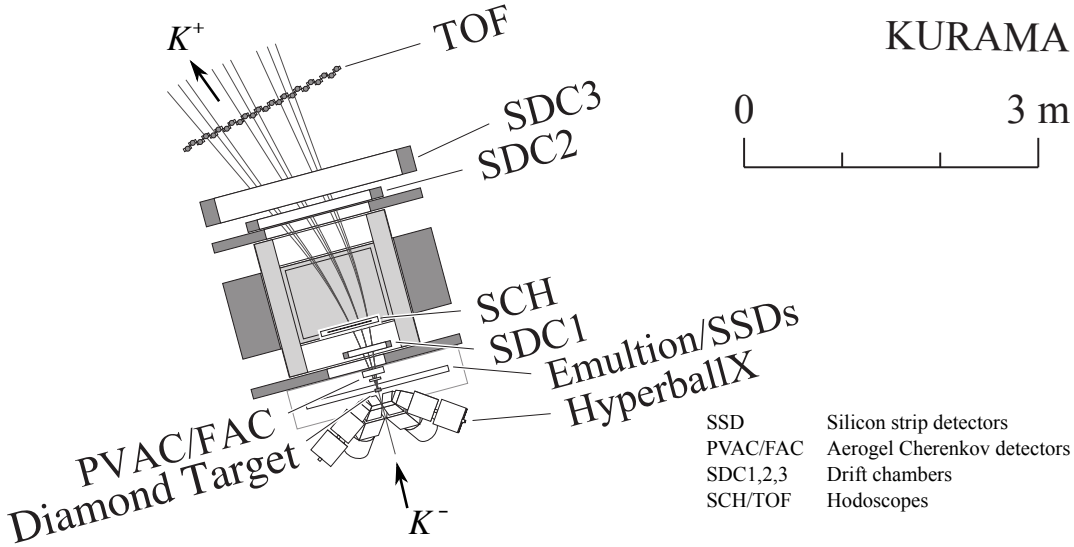

Figure 2.11: The schematic view of KURAMA spectrometer.

Table 2.4: The specifications of detectors of KURAMA spectrometer.

Hodoscope	effective area [mm^2]	thickness [mm]	segment	Readout		
SCH	$673^x \times 450^y$	2	64	MPPC w/ wave length shifting fiber, both ends		
TOF	$1805^x \times 1800^y$	30	24	2" PMT ; H1949, both ends		
Aerogel Cherenkov	effective area [mm^2]	thickness [mm]	index	Readout		
PVAC	$117^x \times 117^y$	14	1.12	2.5" PMT ; R6682		
FAC	$225^x \times 162^y$	60	1.05	2.5" PMT ; R6682		
Drift chamber	effective area [mm^2]		plane	title angle [deg]	wire pitch [mm]	
					anode-anode	anode-cathode
SDC1	$384^x \times 264^y$		$vv'xx'uu'$	$+15, 0, -15$	6	2
SDC2	$1152^x \times 1152^y$		$xx'yy'$	$0, 90$	9	2
SDC3	$1920^x \times 1280^y$		$yy'xx'$	$90, 0$	20	2

Trigger Counters

PVAC and FAC

The Proton Veto Aerogel Cherenkov counter (PVAC) was located downstream of an emulsion module. The scattered K^+ was contaminated with protons with low momenta from $\sim$0.8 GeV/c to $\sim$1.6 GeV/c. Aerogel with the refractive index of the 1.12 was employed to remove the protons (see Fig 2.7). A schematic drawing of PVAC is shown in Fig. 2.12. The effective area was $117^x \times 117^y$ mm^2, and the thickness was 14 mm.

The Forward Aerogel Cherenkov counter (FAC) was employed in order to remove forward background particles, namely high momentum π and unscattered beam K^-. It was located at

the downstream of PVAC. The refractive index of the radiator was 1.05. The effective size was $225^x \times 162^y$ mm^2 and the thickness was 60 mm. Six 2.5" PMTs were attached at both ends of the radiator. A schematic drawing of FAC is shown in Fig. 2.12. Cherenkov light was emitted only for high momentum π and beam K^- around 1.8 GeV/c momentum, but was not for scattered K^+.

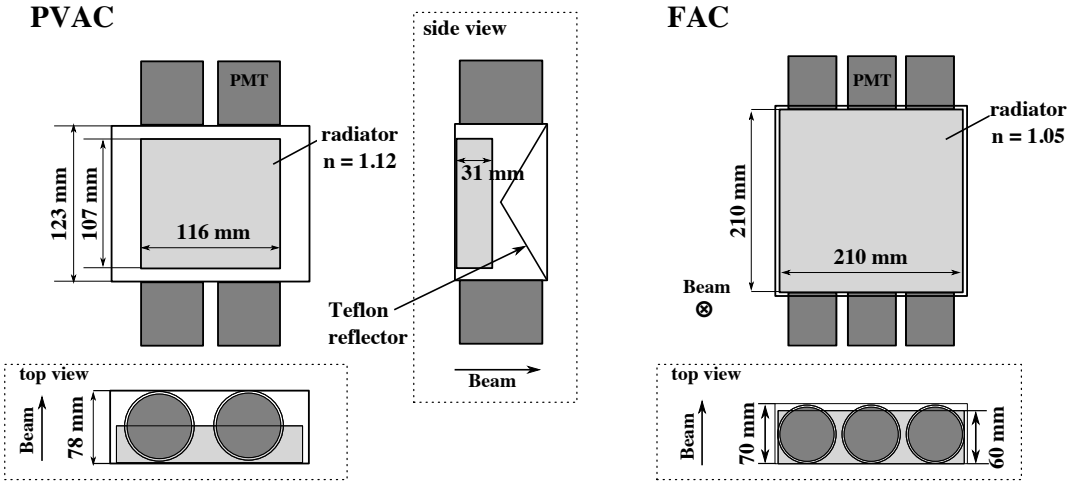

Figure 2.12: The schematic drawing of PVAC and FAC.

SCH

Only with particle identification by AC detectors, contamination of the incident K^- which did not react at the target was not rejected. The hodoscopes were used to distinguish the scattered particles and the beam K^- using the correlation of their hit pattern. To measure the particle position at downstream of the target, the charge hodoscope (SCH) was placed between the poles of the dipole magnet, that is, inside of the magnetic field. The information of SCH hit pattern was included in the matrix trigger described in section. 2.4.3, and hit position information was also used in tracking analysis of the scattered particles. SCH consists of horizontally-segmented 64 slabs of plastic scintillator (EJ-212) of 2 mm thick, wave length shift fibers (Kuraray PSFY-11J) and MPPCs (Hamamatsu S10362-11-100P), similar to FBH. The size of each segment was $11.5^x \times 450^y$ mm^2 and they were assembled with 1 mm overlap in the same way as FBH. The effective area was $673^x \times 450^y$ mm^2.

TOF

To measure the position and time-of-flight of the scattered particles downstream of a dipole magnet, the time-of-flight counter (TOF) was installed downstream of SDC3. TOF consists of 24 segments of 30 mm thick plastic scintillator and the effective area was $1805^x \times 1800^y$ mm^2.

Each segment was wrapped with aluminized mylar and a black sheet. Fish-tail-shaped acrylic light guides and PMTs with 2" diameter (H1949-50) were attached at both ends of a scintillator

slab. The TOF counter was also used for the matrix trigger.

Tracking detectors

SDC1

The drift chamber SDC1 was located at upstream of the KURAMA magnet. SDC1 had six sense-wire planes ($vv'xx'uu'$) with hexagonal cell structure. Each pair plane was tiled by $+15, 0, -15$ degree, respectively, respect to the vertical direction as shown in Fig 2.13 (a). A placement of the wires is shown in Fig 2.13 (b). The sense-wire spacing was 6 mm. Between a pair planes, the position of sense-wire was shifted by a half of the cell. The same mixed gas as used in BC3,4 was used in SDC1. The tracks of scattered particles were affected by the magnetic field because SDC1 was installed close to the yoke of the KURAMA magnet.

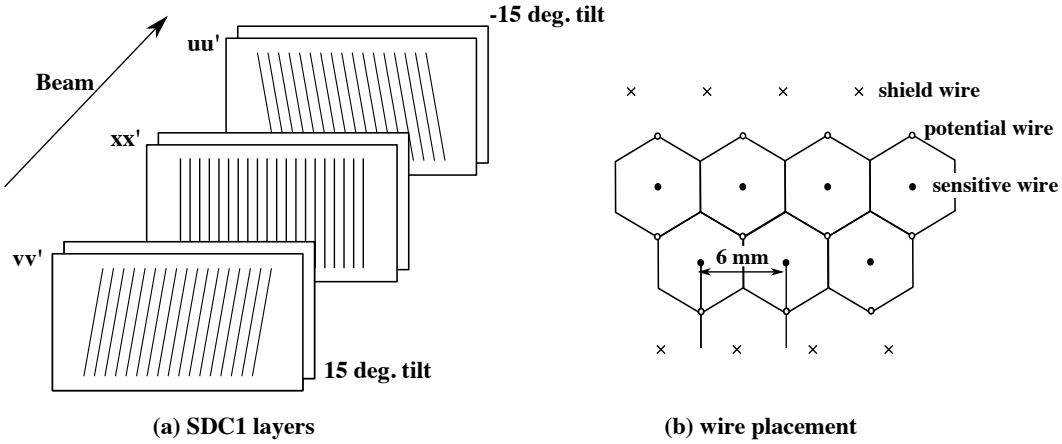

Figure 2.13: The schematic drawing of SDC1

SDC2, SDC3

The drift chambers SDC2 and SDC3 were installed at downstream of the KURAMA magnet. Both of them had four sense-wire planes ($xx'yy'$). The cell structure was almost the same as SDC1 although details such as the wire spacing were different. The sense-wire spacing was 9 mm for SDC2 and 20 mm for SDC3. The y and y' planes were tilted by 90 degree with respect to the vertical direction. Mixed gas of Ar (50%) and C_2H_6 (50%) was filled in both chambers.

2.4.3 Trigger and data acquisition system

KK trigger

The trigger for the data taking of the (K^-, K^+) reaction events was made using the combination of the detector response described above. The logical signals of incident K^- (K_{in}) and outgoing

K^+ (K_{out}) were defined as follows and the diagram is shown in Fig. 2.14.

$$K_{in} = BH1 \cap BH2 \cap (\overline{BAC1} \cap \overline{BAC2}), \quad (2.1)$$
$$K_{out} = TOF \cap PVAC \cap \overline{FAC}. \quad (2.2)$$

In the K_{in} side, the coincidence between BH1 and BH2 was taken in order to identify beam particles. To reject pion contamination, it was required that both of BACs had no signal. In the K_{out} side, the events with TOF hit were accepted as scattered particles. To reject unscattered beam kaons and pions which were transported to TOF, events with no signal at FAC were selected. In addition, a proton with low momentum was rejected if coincident with PVAC.

The matrix trigger ($MATRIX$) was introduced to select the (K^-, K^+) reaction efficiently since the incident K^- which did not react at the target was not rejected by particle identification using the AC counters. The data of the hodoscopes were analyzed online, and the scattered particles were selected using combination of hit pattern. The result was applied to the data taking as the matrix trigger. The 2-dimensional matrix ($2DMATRIX$) was used for selection of the scattered particles using the combination of hit pattern of two hodoscopes, SCH and TOF. The event with a particular correlation between the hit positions of the two detectors were accepted. The beam K^- was identified by the 3-dimensional matrix ($3DMATRIX$) using hit pattern of BFT, TOF and SCH. The particles which were not scattered and passed through the three detectors were rejected as the beam K^-. The matrix trigger is given as

$$MATRIX = 2DMATRIX \cap \overline{3DMATRIX}. \quad (2.3)$$

The "KK trigger" was a coincidence between K_{in} and K_{out} together with the matrix trigger applied, that is,

$$\text{KK trigger} = K_{in} \cap K_{out} \cap MATRIX. \quad (2.4)$$

Table 2.5: Typical values of trigger rates.

trigger	BH1∩BH2	K_{in}	K_{out}	KK trigger
Rate [kHz]	180	140	15	0.6

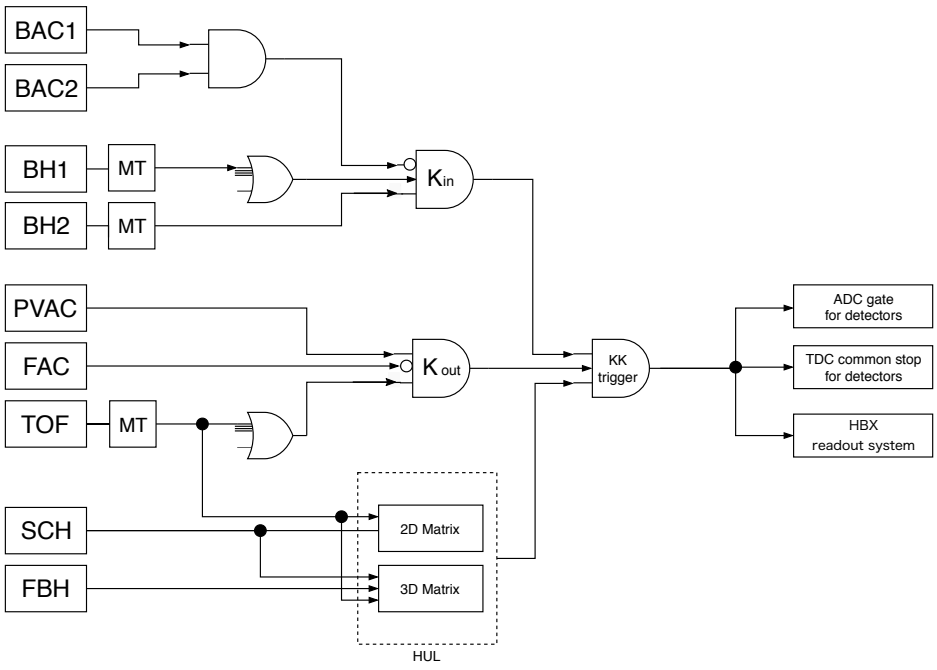

Figure 2.14: The logic diagram of the readout system of the magnetic spectrometers. MT represents a mean timer.

DAQ system

For a data acquisition system for the magnetic spectrometers, we used HD-DAQ [31]. It consists of a master trigger module (MTM), a host computer and subsystems such as VME, COPPER, EASIROC and HUL. An overview of HD-DAQ is shown in Fig. 2.15. The KK trigger, spill gate and

DAQ gate were input to MTM, then the trigger and information of "event tag", that is, the event and spill number, were distributed to each subsystem. The data acquired by the subsystems were sent to the event builder and event distributer of the host computer via the network. Then, the data was kept on being monitored. The signals of PMTs used in the hodoscopes and AC detectors were taken by VME modules, namely CAEN V792 for ADC and CAEN V775 for TDC. The signals of MPPCs used for BFT, FBH and SCH were read out by EASIROC (Extended Analogue Silicon PM Integrated Read-Out Chip) modules [32]. The COPPER (COmmon Pipelined Platform for Electronics Readout)[33] module was used to digitize the timing signal of the drift chamber, BC3 and SDC1. The matrix coincidence trigger was mede using FPGA at the Hadron Universal Logic Module (HUL).

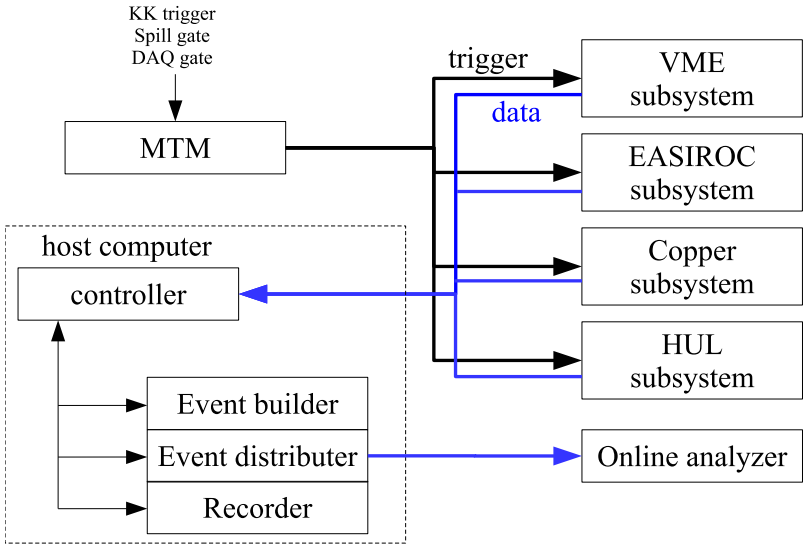

Figure 2.15: Overview of the data acquisition system for the magnetic spectrometers.

2.5 Ξ^- tracking detectors

A track of the Ξ^- particle was reconstructed by the Silicon Strip Detectors (SSD) and the nuclear emulsion. As shown in Fig. 2.16, the SSDs and an emulsion module were located at just downstream of the diamond target. The emulsion module was put between a pair of SSDs. The distance between the end of the target and the first layer of SSD1 was 0.5 mm.

2.5.1 Silicon Strip Detector (SSD1 and SSD2)

A pair of Silicon Strip Detectors (SSD1 and SSD2) was used to reconstruct tracks of the produced Ξ^- and the scattered positive kaon. In emulsion image analysis, the Ξ^- track reconstructed by SSD1 is a clue to find a Ξ^- track in the emulsion. When the Ξ^- particle was detected by SSD2,

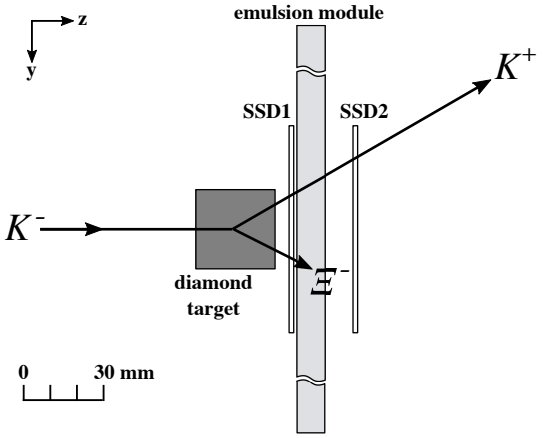

Figure 2.16: The schematic drawing around the target.

the event was rejected since the Ξ^- passed through the emulsion module. Both of SSDs had 4 layers; two measured x position and the others measured y position. The p-in-n type silicon sensors which were a product of Hamamatsu Photonics were used, and their thickness was 0.32 mm. The sensitive area was $76.8^x \times 76.8^y$ mm^2. A strip pitch was 0.05 mm. One side of the silicon sensor was attached to the APV readout chip (APV25-s1) and signals were transferred to 10-bit Flash-ADCs. The ADC value summed up for all the readout channels was defined as the energy deposit at SSD. Calculating with a typical density of the silicon sensor, 2.33 [g/cm^3], the thickness of SSD1 in the beam direction was 2.98 [g/cm^2].

2.5.2 Nuclear emulsion

The emulsion module was located about 0.7 cm downstream of the target. In one module, 13 nuclear emulsion sheets were packed as shown in Fig. 2.17. The size of an emulsion sheet was $345^x \times 350^y$ mm^2. Two types (thin type and thick type) of emulsion sheets were prepared. Each sheet had a polystyrene base. Its both sides were coated with photographic emulsion layer as shown in Fig. 2.17. For the thin- and thick- type sheets, thickness of the emulsion layer was 0.2 mm and 0.9 mm, respectively. The thickness of the base layer was 0.18 mm and 0.04 mm for the thin and thick sheets, respectively. The thin-type sheets were placed at both faces of the emulsion module to improve angular accuracy of tracking. The thick-type sheets with a large sensitive volume were employed for the other 11 sheets. The density of the employed emulsion called Fuji GIF was 3.53 g/cm^3. The composition of Fuji GIF is listed in Table. 2.6.

In the experiment, they were installed in a special holder called the Emulsion Mover (EM). EM changed the emulsion position automatically. In this way, a position at the emulsion module where the beam particles were incident was changed spill by spill so that the whole area of emulsion sheets was exposed almost uniformly.

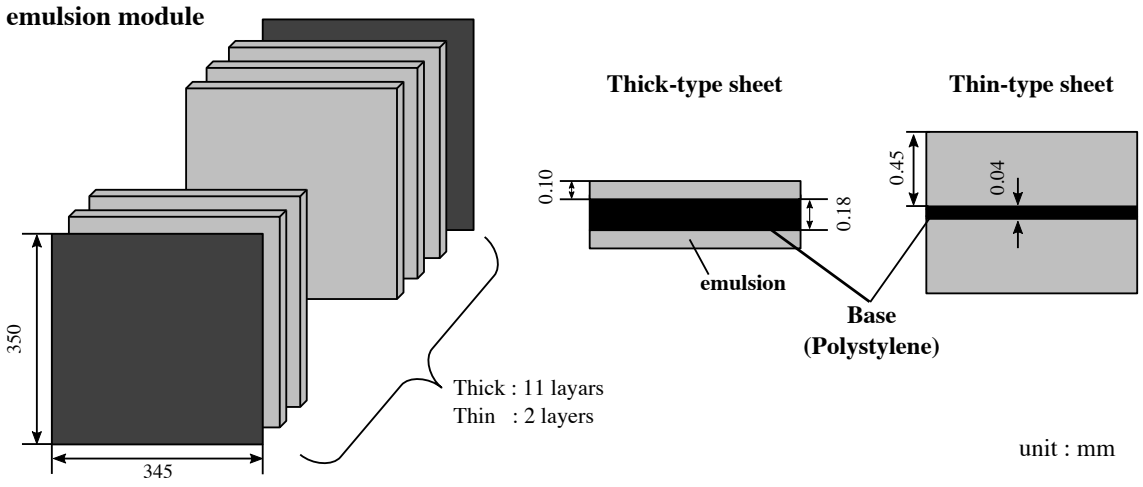

Figure 2.17: Drawing of an emulsion module

Table 2.6: Composition of dried emulsion, Fuji GIF

	H	C	N	O	Br	Ag	I	others	total
density [g/cm^3]	0.05	0.326	0.11	0.23	1.166	1.6	0.033	0.015	3.53

2.6 X-ray detector : Hyperball-X (HBX)

The X-ray detector must be able to measure the energy shift of a few hundreds eV. Accuracy of X-ray measurement depends on statistical errors ($\sigma_{stat.}$) and systematic errors ($\sigma_{sys.}$). The former depends on the X-ray yield (N_{Xray}) and energy resolution of detectors (σ_{E_γ}) and is given as $\sigma_{stat.} = \sigma_{E_\gamma}/\sqrt{N_{Xray}}$ if the background is negligible. The expected X-ray yield was a few tens of counts in this experiment. In order to measure Ξ^- atomic X rays with a few hundreds eV accuracy, germanium (Ge) detectors which can measure X rays with high resolution (σ_{E_γ} $\sim$0.85 keV at 300 keV) was employed. Assuming that N_{Xray} is 30 counts, the statistical error is 160 eV. On the other hand, for systematic errors, those associated with energy calibration were considered. By the energy calibration method used in our past hypernuclear $\gamma-$ray spectroscopy experiment at J-PARC (J-PARC E13)[34], a few hundreds eV of calibration accuracy was not achieved. Thus, the new method was developed for this experiment.

The schematic view of the Ge detector array called Hyperball-X is shown in Fig. 2.18. It consists of six sets of a Ge detector and BGO detectors placed around the diamond target. The positions for the three sets at the right half were numbered as SLOT1, 2 and 3, and those at the left half were numbered as SLOT4, 5 and 6. A pair of LSO scintillators and ^{22}Na sources were also installed for a new calibration system.

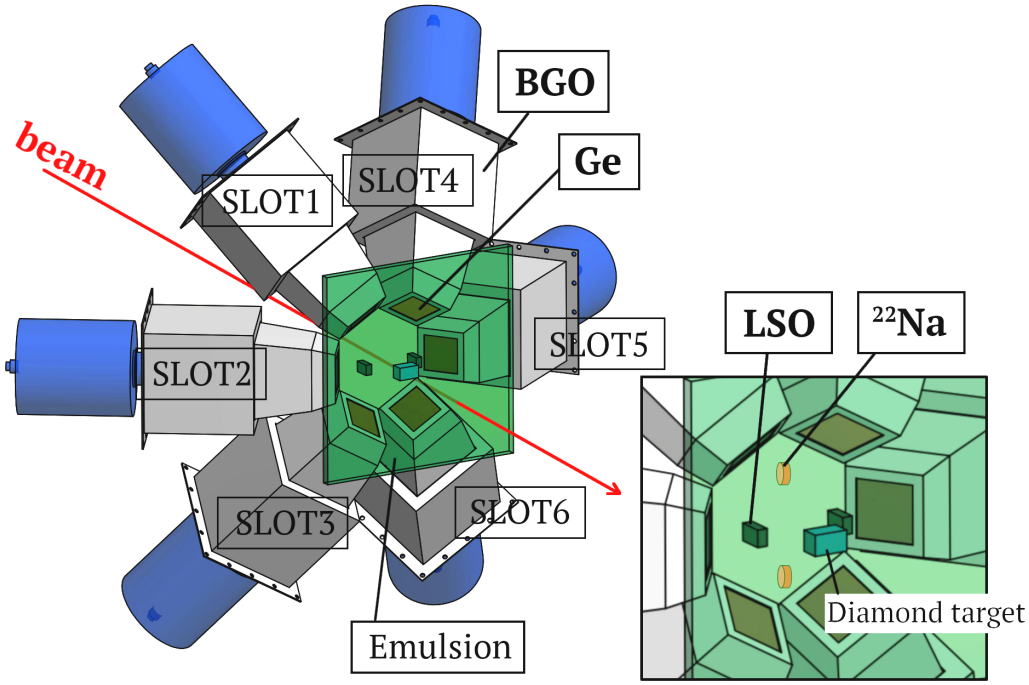

Figure 2.18: Schematic view of Hyperball-X. It consists of six sets of Ge detector and BGO detectors placed around the diamond target. In addition, LSO scintillation counters and ^{22} Na sources were installed as an energy calibration system.

2.6.1 Ge detectors

The coaxial-type Ge detectors were used. Two of them were of the "clover-type" and the others were of the "standard-type". The clover-type detector, the products of EURISYS company, had four n-type crystals with a volume of 85 cm^3 and they were arranged like clover leaves in a common cryostat. Entrance of the Ge crystal was covered with a thin beryllium window. The relative efficiency was 80%[2]. They were installed at SLOT 1 and 2. On the other hand, the standard-type detector has a single crystal. In this thesis, this detector is called a "single-type" detector. Four single-type detectors, one by Canberra and the others by ORTEC, were installed at SLOT 3, 4, 5 and 6. These detectors had n-type crystals with a volume of 250 cm^3. The relative efficiency was about 60%. The detailed specifications of the Ge detectors are listed in Table 2.7. The distance between the entrance of the Ge detector and the center of the emulsion module was about 17 cm. The single rate was 2 kHz for the clover-type detectors and 4∼6 kHz for the single-type detectors. The reset rate was 100 Hz for the clover-type and 200∼400 Hz for the single-type detectors.

[2]The reference value of the efficiency is defined as the absolute photopeak detection efficiency of 1.33 MeV-γ ray from ^{60}Co placed at 25 cm away by a NaI detector with crystal size of 3"×3"ϕ

Table 2.7: Main specifications of the Ge detectors.

Location	type	crystal volume [cm^3]	relative efficiency [%]
SLOT 1	clover	85	80
SLOT 2	clover	85	80
SLOT 3	single(ORTEC)	250	61.3
SLOT 4	single(Canberra)	250	55
SLOT 5	single(ORTEC)	250	62.3
SLOT 6	single(ORTEC)	250	60.3

The Ge detectors were located around the target where high energy γ rays were produced by the high rate beam (∼700 kHz). In order to operate Ge detectors under this high energy-deposit environment, a transistor-reset type preamplifier was employed. As shown in Fig. 2.19, a feed back capacitor and a transistor switch were connected to an operational amplifier in parallel. When a charge was collected, the output voltage changes stepwise as shown in Fig. 2.20. The step height corresponds to the energy deposit by a radiation. Input charges were stored in a capacitor. When charges were accumulated up to the maximum voltage allowed for the amplifier operation, the transistor switch was turned on. Then the change in the capacitor was discharged at once and the voltage was reset to zero level. At the timing of this discharge, the "reset signal" was produced. After the reset, input pulses cannot be processed correctly because of an undershoot caused by the reset signal in the shaping amplifier due to a rapid change of voltage. It took a few hundreds of microsecond to recover the base line of the shaping amplifier.

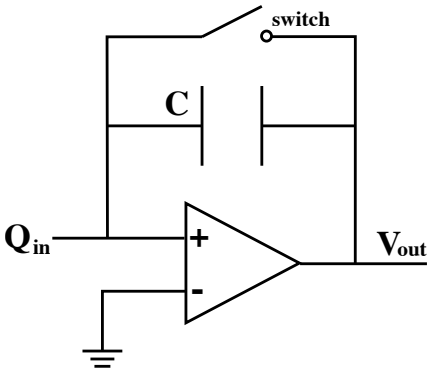

Figure 2.19: A circuit of a transistor-reset type preamplifier.

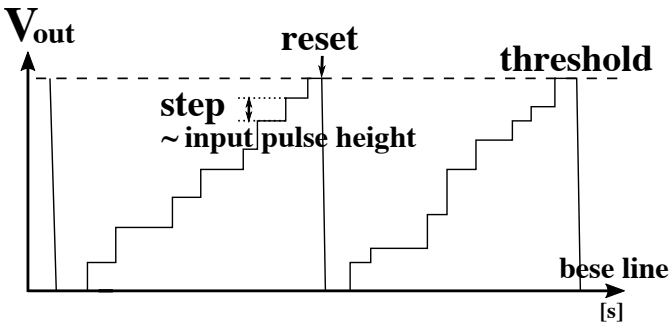

Figure 2.20: The output signal of a preamplifier.

2.6.2 BGO ($Bi_4Ge_3O_{12}$) detector

Each Ge detector was surrounded by BGO detectors for background suppression. When γ rays are Compton-scattered in the Ge detector or high energy charged particles from the beam penetrate

the Ge detector, they make background in the Ge detector. The BGO detectors were introduced in order to reject these background events by anti-coincidence of the Ge detector and the BGO detectors. As shown in Fig. 2.21, two types of the BGO detectors were used, one with 6 crystals and the other with 12 crystals. 9/8" PMTs were attached to each crystal. For the clover-type Ge detector, the 12-crystal BGO detector was used, and background events were rejected by coincidence between the Ge detector and 4 BGO crystals close to it. For the single-type detector, the 12 crystal-type or the 6 crystal-type BGO detector was used; coincidence hit in any of the 12 or 6 BGO crystals was checked. An iron shield was installed around the PMTs to reduce the effect of the magnetic field of the KURAMA magnet.

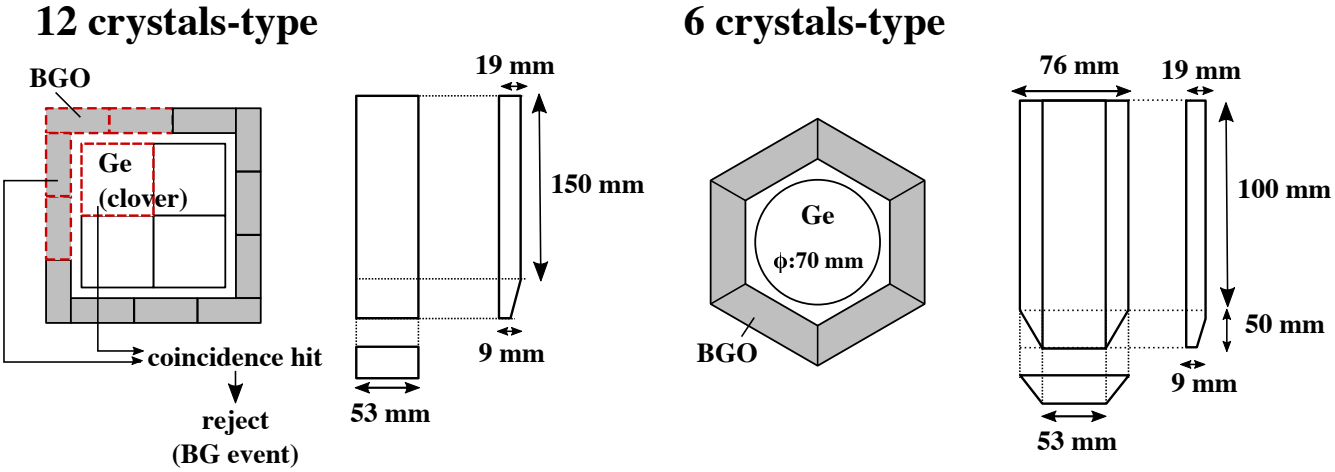

Figure 2.21: Schematic drawing of BGO detectors. Two types of BGO detectors, assembled in 12 or 6 crystals, were used. The 12 crystals-type detectors for the clover and single Ge detectors were installed in SLOT 1, 2, 3 and 4. The 6 crystals-type detectors for the single Ge detectors were installed in SLOT 5 and 6.

2.6.3 Readout system

The readout system of Hyperball-X is shown in Fig. 2.22. The output signal of the preamplifier for the Ge detector was divided into two lines; one was for TDC and the other was for ADC. One of the Ge preamplifier output signals was sent to the timing filter amplifier (TFA), ORTEC 579, and then sent to the constant function discriminator (CFD) in which the signal was discriminated at a timing independent of pulse height. The output signal of the CFD was sent to a multi-hit TDC. The CFD signals were also used for the trigger signal of the Ge detector hit. A noise due to electronics and low energy background radiation lead to an increase of the single rate of the Ge detector and dead time of the shaping amplifier. To prevent a high singles rate, the threshold for the input pulse height was set in CFD as shown in Table 2.8. The highest CFD threshold sets the lower limit of the ADC range to 120 keV. The single rate of the Ge detectors was 10∼20 kHz during the data-taking period.

Table 2.8: The threshold value set in CFD. Ge detector ID represents the SLOT number. For clover-type detector, the crystal number is written after the hyphen.

Ge detector ID	threshold [keV]	Ge detector ID	threshold [keV]
1-1	100	3	110
1-2	70	4	80
1-3	90	5	80
1-4	90	6	110
2-1	100		
2-2	110		
2-3	120		
2-4	90		

For the transistor-reset type preamplifier, the baseline of the shaping amplifier output signal was distorted over a few hundreds of μs after the transistor reset. To avoid data-taking during this period, the veto signal of 300 μs width was sent to the CFD. The reset timing signal from each Ge detector was used as a start timing of the veto signal. For the clover-type Ge detector, the reset timing signals were sent to a reset synchronizer module. When a reset happens in one of the four channels, this module sends signals to the other three preamplifier channels forcing them to reset. The other Ge preamplifier output signal was used for ADC. Firstly, it was sent to a shaping amplifier, ORTEC 671 with 2-μs shaping time, to produce a Gaussian shaped signal. Then the signal was sent to a peak-sensitive ADC, ORTEC AD413a. The trigger signal for X-ray detection was generated from the CFD output signal of the Ge detector in coincidence with the (K^-, K^+) reaction trigger (Ge$\cap$KK trigger). Two additional triggers explained in Section 2.6.5 were also generated for energy calibration.

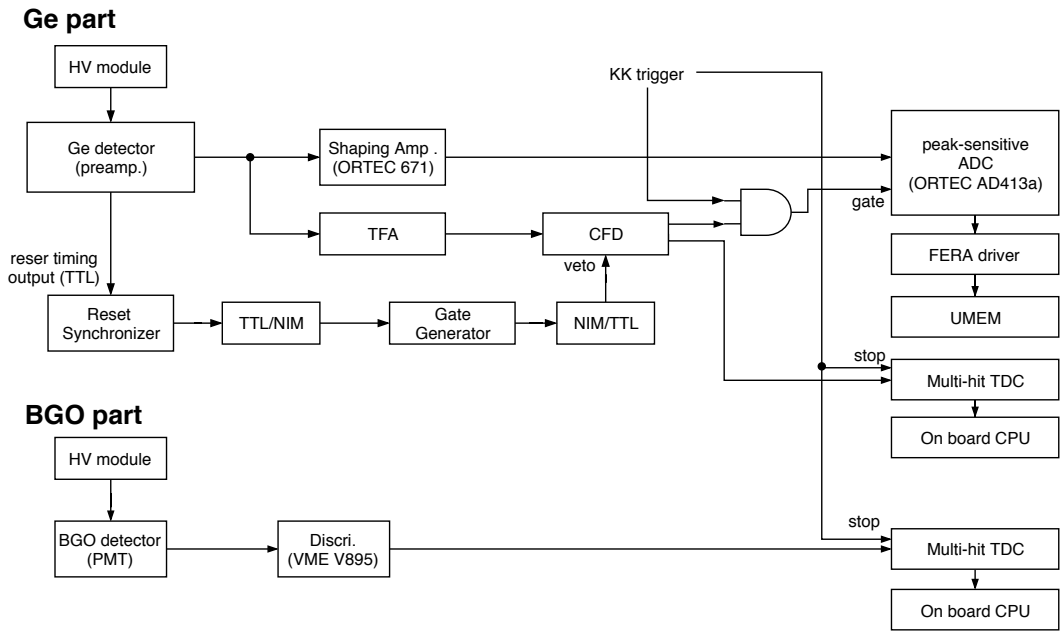

Figure 2.22: The diagram of readout system for Ge and BGO detectors.

For the BGO detector, only TDC data were taken. The output signal from a PMT was discriminated and sent to a multi-hit TDC. As a common stop signal of the TDC, the KK trigger was used.

2.6.4 Energy calibration system

When the Ge detectors are operated with high counting rate at the J-PARC K1.8 beam line, the γ-ray peak position is shifted a few hundreds eV between during the beam on and off period due to a huge beam background. This shift can not be negligible for measurement of the Ξ^-atomic X-ray energy shift expected to be $\sim$300 eV. Thus, an in-beam energy calibration was required. In addition, a high precision calibration was required so that the systematic error by energy calibration is comparable to or less than the expected statistical error of 150 eV. A new In-beam calibration method with a high accuracy using LSO triggerable sources and ^{22}Na sources was developed. There are four advantages for this calibration system.

- The in-beam calibration data can be taken.
- The calibration data can be taken simultaneously under the same condition as the main data taking.
- The reference peaks can be clearly identified even with a high counting rate due to high intensity beams.

- The X-ray energy region of our interest is calibrated by interpolation using the reference energies.

Firstly, the calibration data should be taken under the same in-beam condition as the main data taking. It is because a peak position shifts between the on-beam and off-beam periods due to baseline shift of the shaping amplifier. The spectra of 307-keV γ ray during on-beam and off-beam period for one hour data-taking is shown in Fig. 2.23. The calibration parameters for on-beam data were applied to both data. These γ-ray peaks were fitted with a gauss function plus linear function. For on-beam and off-beam data, the mean value was obtained to be 306.91 keV and 306.77 keV, respectively, with the errors of less than 10^{-3} keV. Thus the peak position shifted at least $\sim$100 eV.

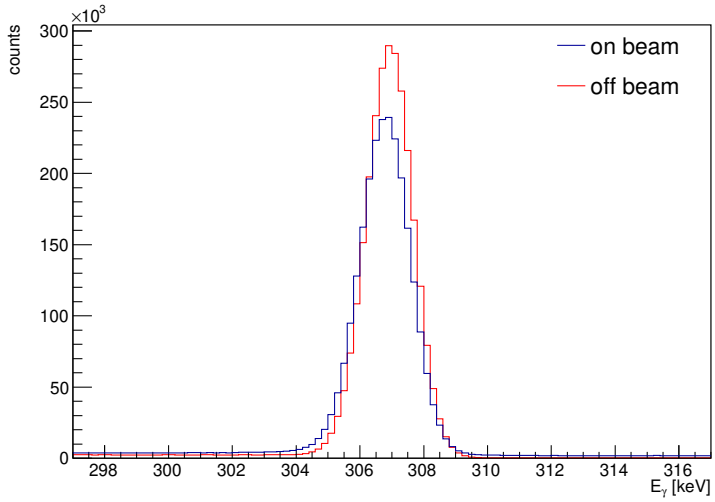

Figure 2.23: The 307-keV γ ray peak detected on-beam (blue) and off-beam (red) period.

Secondly, the calibration data should be taken simultaneously during the data taking to track the gain drift of the Ge detector readout system due to beam intensity and temperature changes. Such gain shift can not be tolerated for one month of the data-taking period considering an energy shift of the X ray less than sub keV. The shift of the mean value of the 307-keV γ ray from ^{176}Lu in LSO during data-taking period was plotted in Fig. 2.24. The calibration parameters for the first run were applied to all the runs. The peak position shifted by 200 eV.

Thirdly, the reference peaks should be identified without buried in huge in-beam background events. When performing a run by run calibration, use of a weak radiation source is desired in order to avoid increase of background in the X-ray spectrum. Thus, the data of the reference γ rays should be selectively acquired.

Fourthly, X-ray energies of our interest, 370 keV and 316 keV, should be calibrated by interpolation of the reference γ-ray energies. Therefore, for example, the ^{60}Co source emitting 1173 keV and 1332 keV γ rays were not suitable for this experiment.

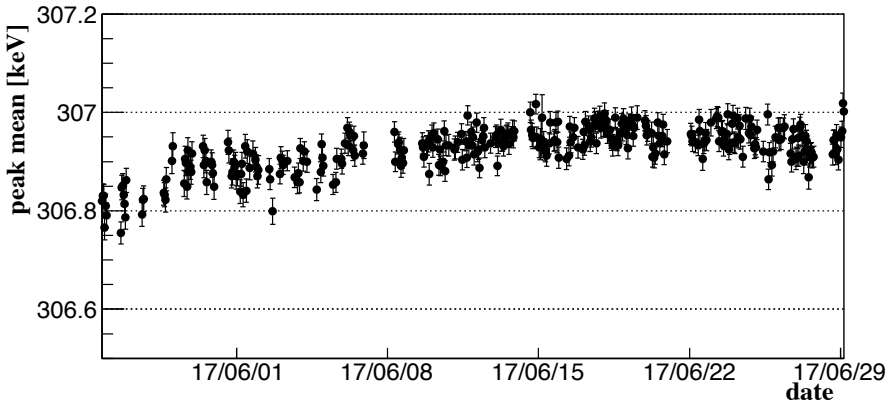

Figure 2.24: The shift of peak position of the 307-keV γ ray from LSO during the data-taking period.

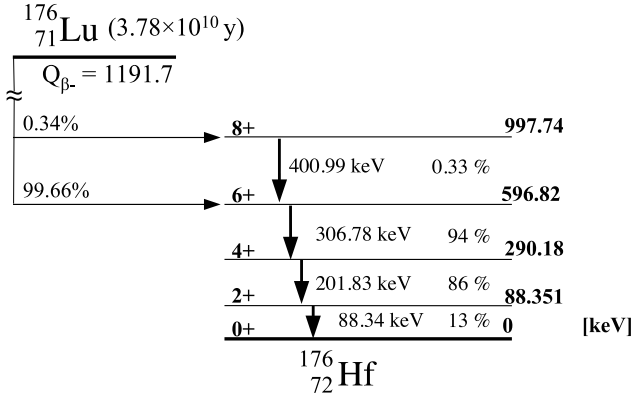

Figure 2.25: Decay scheme of ^{176}Lu [36]. The ^{176}Lu nucleus beta decays to excited states of ^{176}Hf. It decays to the ground state with cascade γ-ray emission. The 202-keV and 307-keV γ rays are used in the present calibration.

Triggerable calibration source : LSO system

LSO (Lu_2SiO_5) is a scintillator having self-activity of ^{176}Lu. As shown in the ^{176}Lu decay scheme (Fig. 2.25), ^{176}Lu beta decays (half life $\sim 3.7 \times 10^{10}$ y) followed by three γ-ray emissions in cascade (88.34 keV, 202.843 keV, and 306.791 keV). The activity of LSO amounts to 300 Bq/cm^3. The idea here is that we take β-γ coincidence between the LSO counter (β) and the Ge detector (γ) for β-decay events of ^{176}Lu [35]. The scintillation light from an LSO crystal was detected using a multi-pixel photon counter (MPPC) since it can be operational even in the magnetic field from the magnetic spectrometer installed just downstream.

The statistical accuracy of the peak position of the reference γ rays depends on the peak counts. When the peak counts are more than 300, the accuracy is $\sigma = 50$ eV at 400 keV which is good enough. The LSO counter was designed to detect 300 counts of γ rays in one-hour run taking into account the distance between the LSO counter and the Ge detector, the LSO crystal size, and the

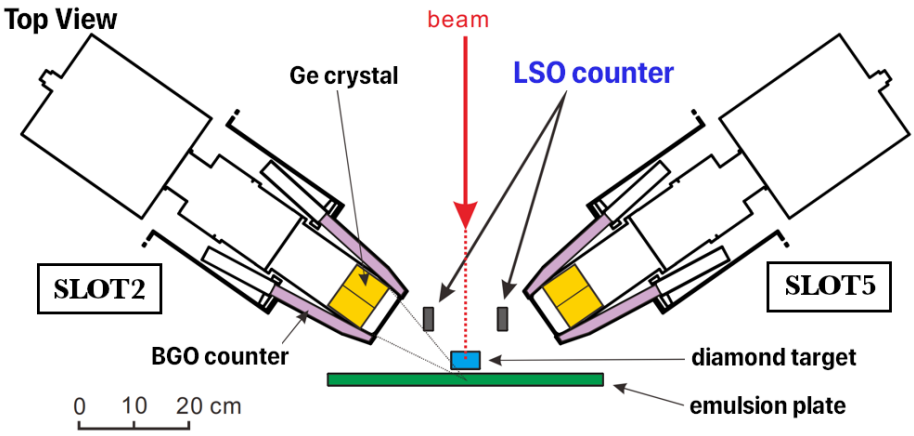

Figure 2.26: The location of the LSO counters. The distance between the LSO counter and the Ge detector on the beam height is about 5 cm.

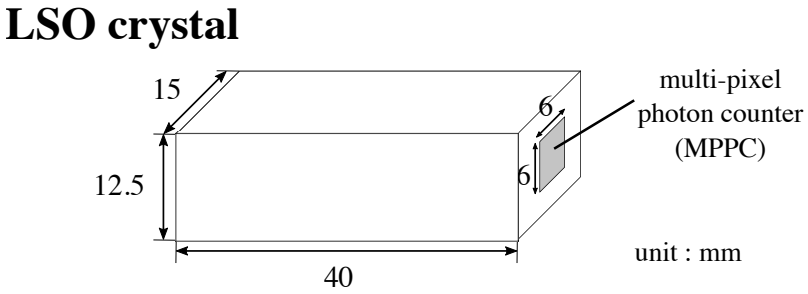

Figure 2.27: Schematic drawing of the LSO counter. The LSO crystal size was 12.5 mm × 15 mm × 40 mm (2250 Bq). The MPPC attached to the LSO crystal had a size of 6 mm × 6 mm and contained 6400 pixels.

light yield of the LSO scintillator.

A pair of LSO counters was installed near the Ge detectors as shown in Fig. 2.26. They were fixed to the Hyperball-X frame beside the two Ge detectors at the beam height (SLOT 2 and SLOT 5) via aluminum arms. The distance between the LSO counter and the Ge detector was about 5 cm. One LSO counter was used to take coincidence with the Ge detectors on the right half side (SLOT 1-3) and the other on the left half side (SLOT 4-6) of Hyperball-X.

The crystal size was determined so that sufficient peak counts of 300 for an hour could be obtained when installed in the position shown in Fig. 2.26 [3]. In this geometry, the expected absolute total photopeak detection efficiency for one clover-type Ge crystal was 0.07% at 370 keV. The required activity was then estimated to be 2500 Bq. We used two 2250 Bq LSO crystals (12.5 mm × 15 mm × 40 mm) as shown in Fig. 2.27, that is, 4500 Bq of activity in total.

The light yield of the LSO scintillator also affects the peak counts. The MPPC we used has a

[3]The beam is extracted every 5.5 seconds with the duration of about 2.2 seconds in the J-PARC accelerating cycle. Therefore, the total on-beam period is about 1400 seconds in an hour data taking.

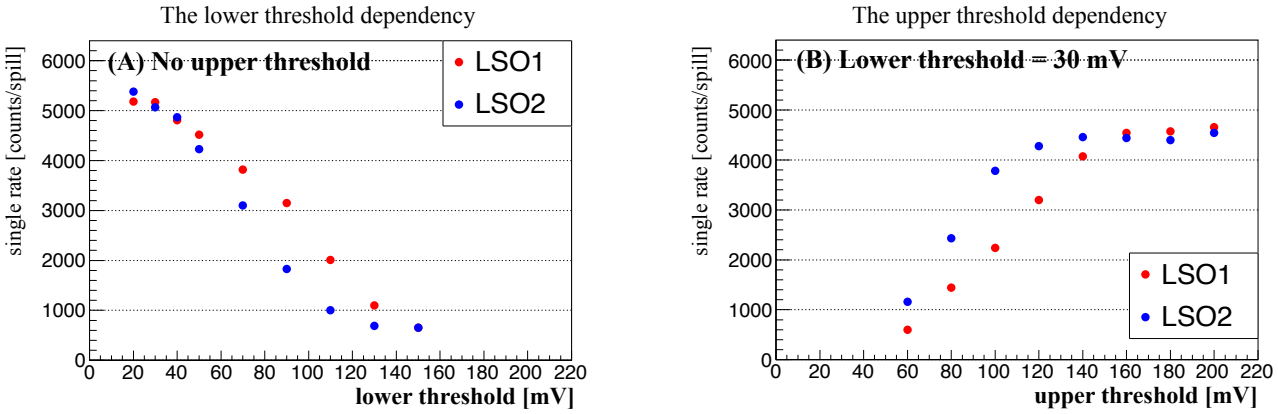

Figure 2.28: The threshold dependency of LSO singles rate. The lower threshold dependency without the upper threshold is shown in (A). The upper threshold dependence lower threshold of 30 mV is shown in (B).

size of 6 mm × 6 mm with 6400 pixels. The LSO crystal to which the MPPC was attached with silicone optical grease (BC-630) was wrapped with a teflon sheet. The waveform was observed on the oscilloscope to check amount of a dark current (a few photons) and γ rays from a ^{60}Co source. In the case of an LSO crystal which is twice in the volume of the actually used ones, about 1500 photons were observed for the 1173-keV γ ray from a ^{60}Co source. As shown in Fig. 2.25, the maximum β-ray energy of ^{167}Lu is 596 keV. It means that this β ray corresponds up to 800 photons. We found, therefore, that a maximum number of photons from the 596 keV β ray is well above that from dark current. In addition to the dark current of MPPC, high energy particles from the beam also produce signals in LSO. In order to reject these false events, we should set lower and upper thresholds for the LSO trigger event for the dark current and the high energy deposit, respectively. We optimized these threshold levels by studying the in-beam LSO singles count rate. The dependence of the LSO single rate on the lower/upper thresholds are shown in Fig. 2.28. In plot (A), the lower threshold dependence of the single rate is shown; the upper threshold is not applied. We set the lower threshold to 30 mV to suppress the dark current. Similarly, the plot (B) shows the upper threshold dependence with a lower threshold fixed to 30 mV. The upper threshold was set to 180 mV and 140 mV for the LSO1 and the LSO2, respectively, above which the single rate saturates because these levels correspond to the maximum energy deposit (1200 keV) by the ^{167}Lu β-decay event.

The peak counts of the ^{176}Lu γ rays detected in each Ge detector during one hour data-taking period are shown in Fig. 2.29. SLOT 1 and 2 were of the clover-type Ge detector. The LSO peak counts are larger for the Ge crystals in SLOT 2 and 5 since they are closest to the LSO counters. The γ rays could be self absorbed in the LSO scintillator. The 202-keV γ ray count is smaller than that of 307-keV γ ray because of a higher self-absorption probability for lower energy γ rays. At least 400 peak counts were attained for each of all the reference γ rays.

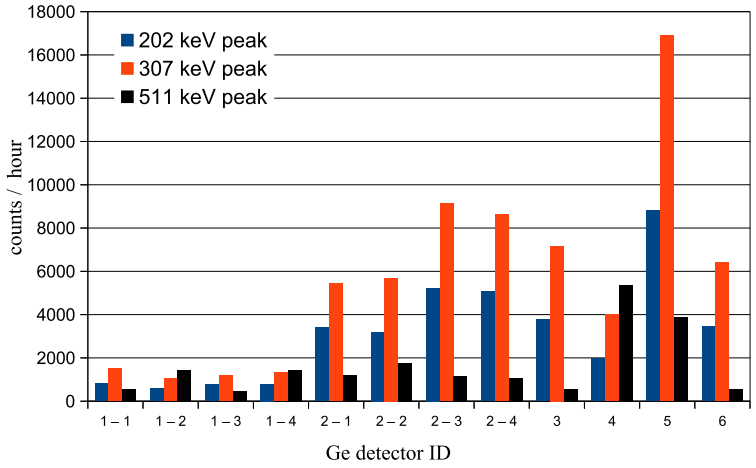

Figure 2.29: Peak counts detected by the Ge detectors for the reference γ rays from ^{176}Lu. Ge detector ID represents the SLOT number. For clover-type detector, the crystal number is written after the hyphen. For each reference γ ray, the peak counts are more than 400.

^{22}Na source

In order to calibrate 370-keV γ ray by interpolation, a reference point is required over 370 keV. The 511-keV γ ray produced by the disappearance of electron and positron come beam was not used because the peak shape was found to be distorted and broadened in the past study. Thus, a γ-ray from a reference ^{22}Na source was used. ^{22}Na emits a positron via β^+ decay, followed by emission of two back-to-back 511-keV γ rays. Using the 511-keV peak from ^{22}Na source as well as the LSO peaks, the energy region of our interest can be calibrated by interpolation. Two ^{22}Na sources were installed above and below the reaction target as shown in Fig. 2.18. Coincidence measurement was made between a pair of Ge detectors located on the left and right half of Hyperball-X (SLOT 1 and 5, SLOT 2 and 4, SLOT 3 and 6). The radioactivity of the two ^{22}Na sources were 3.7×10^3 Bq and 1.07×10^2 Bq, respectively. The ^{22}Na peak counts in an hour are also shown in Fig. 2.29. Even for the case of SLOT 3 and 6 with the weaker ^{22}Na source, the peak counts were more than 400.

2.6.5 Triggers for Hyperball-X

Data of the X rays from Ξ^- atoms and the three reference γ rays were taken by independent triggers. Three types of triggers were: (a) Ge-(K^-, K^+) coincidence trigger (Ge$\cap$KK), (b) Ge-LSO coincidence trigger (Ge$\cap$LSO), (c) Ge-Ge coincidence trigger for ^{22}Na (Ge$\cap$Ge). The diagram of these trigger logic circuits is shown in Fig. 2.30. The Ge CFD output signal explained in Fig. 2.22 was used as the Ge timing signal. The output signal of the LSO counter was sent to a discriminator to apply the lower/upper threshold discussed above. These trigger signals were sent as a start signal

to a multi-hit TDC (MHTDC) used in the common stop mode. The BH2 signal from the incident beam particles was used as the stop signal. Every event was registered together with its trigger type. Which trigger is used to record an event can be identified by checking a correlation between TDC data of these triggers and the Ge TDC data.

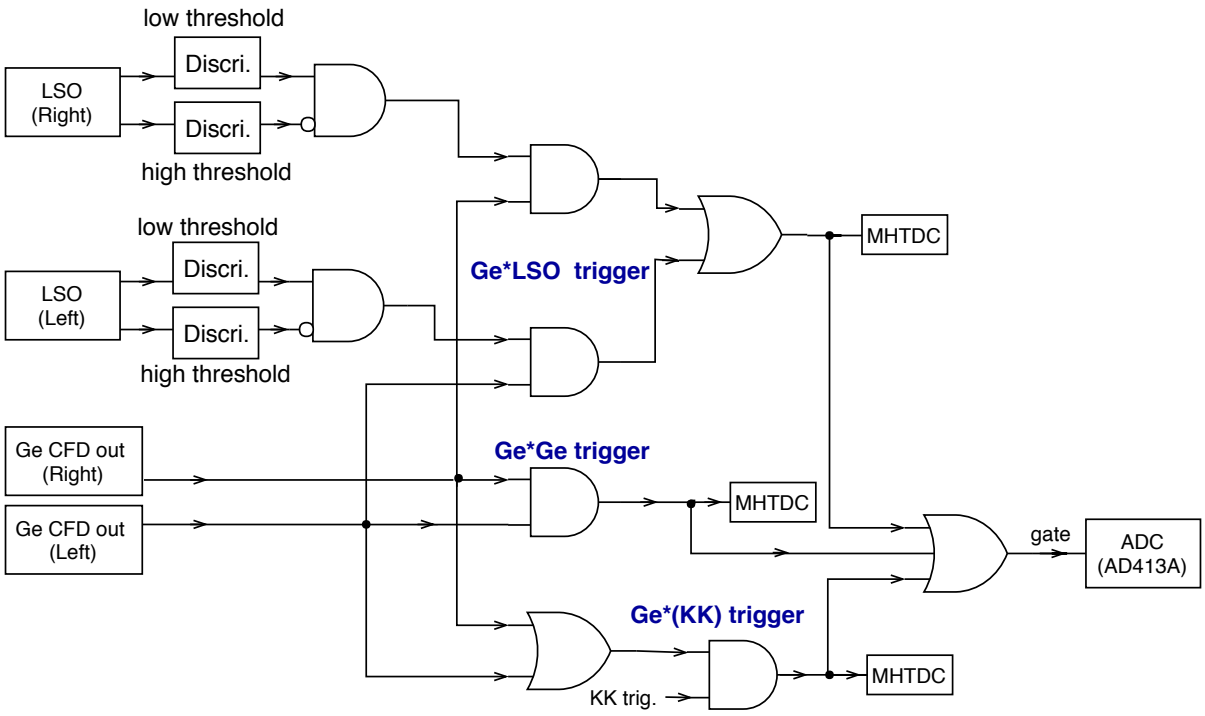

Figure 2.30: The diagram of the trigger logic circuit. Three trigger signals were generated from the CFD output signal of the Ge detector in coincidence with the LSO signal (Ge∩LSO), the other Ge signal (Ge∩Ge) or the (K^-, K^+) reaction trigger (Ge∩KK). The trigger signals were sent to the multi-hit TDC (MHTDC) so that every event was tagged with the trigger type.

The in-beam ADC spectra selected by these three triggers for one of the clover-type Ge crystals are shown in Fig 2.31. The beam intensity was 130 kHz for kaon plus 30 kHz for pion. After the events that a Ξ^- stopped in the emulsion are identified by the emulsion image analysis, Ξ^- atomic X rays should be visible in (a) of the Ge∩KK trigger. The (b) and (c) spectra are for the Ge∩LSO trigger and the Ge∩Ge trigger, respectively. With the β-γ or γ-γ coincidence, clean spectra for calibration data were obtained even in high background counting rates. Each peak was fitted with a Gaussian function and a quadratic function for background.

2.7 Data summary

The data taking was performed in 2016 and 2017. For the Ξ^- production run, the diamond target was irradiated with 11.4×10^{10} K^- beam in total. In 2016, 18 emulsion modules were exposed in

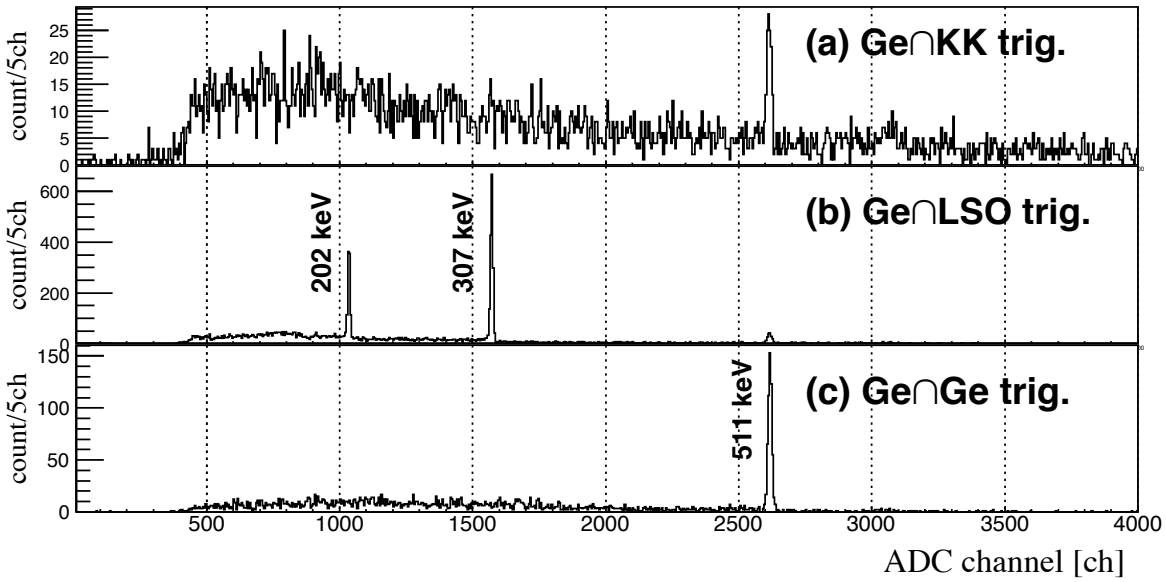

Figure 2.31: ADC spectra for one of the clover-type Ge crystals taken by three trigger conditions. The(a), (b) and (c) spectra are for the Ge∩KK trigger, the Ge∩LSO trigger and the Ge∩Ge trigger, respectively. They are from the in-beam X-ray measurement run data taken for an hour.

11 days, and in 2017, 100 emulsion modules were exposed in 38 days. For the calibration run, the polyethylene target was irradiated with 1.9×10^9 K^- beam.

Chapter 3

Analysis and Results

3.1 Overview

The data for X rays from Ξ^-Ag and Ξ^-Br atoms (case1) and Ξ^-C atoms (case2) were analyzed. The procedure of analysis is shown in the flowchart in Fig. 3.1.

The X-ray analysis was common to both cases and described in Section 3.2. The coincidence events between the (K^-, K^+) trigger and the Ge detectors were selected and analyzed. Using the Ge hit TDC, the Ge detector which triggered was selected. The Ge ADC was calibrated by the new calibration method using LSO counters and ^{22}Na sources. Background events were rejected by the BGO detectors. Analysis of the (K^-, K^+) reaction was also performed common to both cases. The incident K^- and the scattered K^+ were analyzed by the K1.8 beam line and KURAMA spectrometers, respectively. The missing mass was reconstructed, and the Ξ^- production events were selected. This is described in Section 3.3.

The events in which the Ξ^- stops in the emulsion were selected for Ξ^-Ag and Ξ^-Br atoms production. The Ξ^- track was analyzed by SSDs, and the vertex point of the $p(K^-, K^+)\Xi^-$ reaction was reconstructed. From the Ξ^- track, the Ξ^- injected point on the surface of the first layer of the emulsion was determined. Then a Ξ^- track was searched for in the developed emulsion image. The Ξ^-Ag and Ξ^-Br atomic X-ray spectra were obtained by combining the analysis for production of Ξ^-Ag and Ξ^-Br atoms and the X-ray analysis. This is described in Section 3.4.

For production of Ξ^-C atoms, those events in which a produced Ξ^- is expected to stop in the diamond target with a large probability were selected. Using information of SSD1 located downstream of the target, the events Ξ^- passing through the target were rejected. Then, by comparing to Geant4 simulation[1], Ξ^-s with a large probability of stopping in the target were selected. The Ξ^-C atomic X-ray spectra were obtained by combining analysis for production of Ξ^-C atoms and the X-ray analysis. This analysis is described in Section 3.5.

[1]Simulation tool which calculate the passage of particles using Monte Carlo method. Developed by CERN.

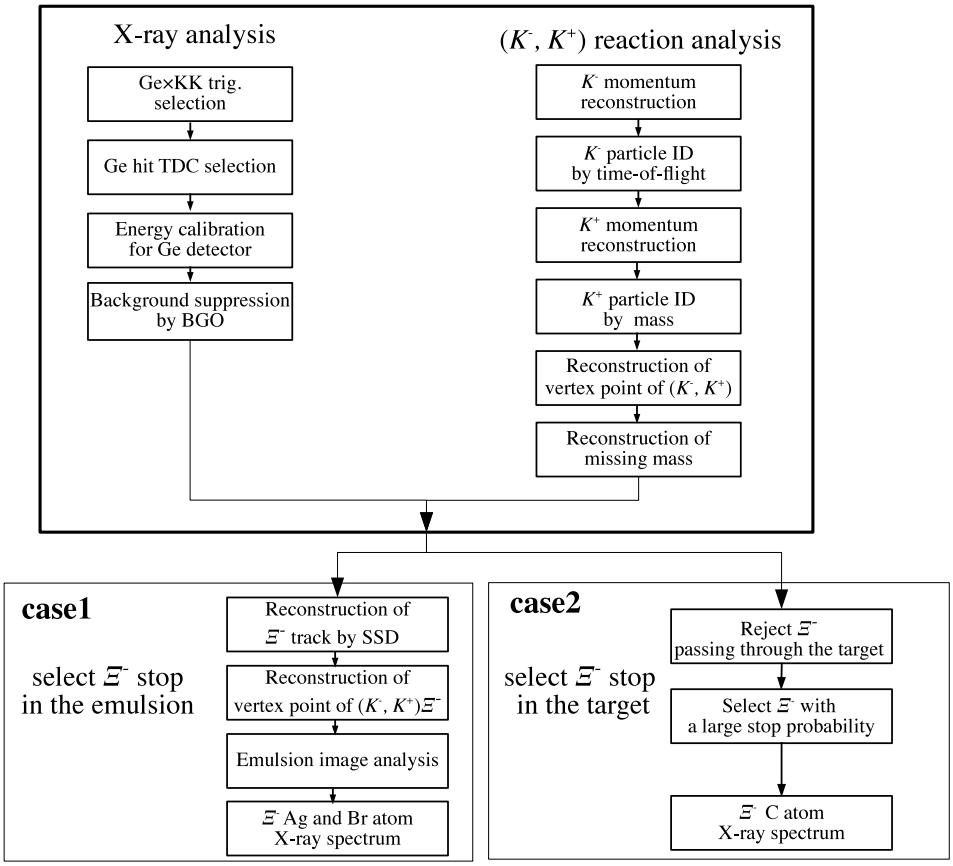

Figure 3.1: A procedure of analysis.

3.2 X-ray Analysis

In this section, analysis of Hyperball-X is explained. The analysis was carried out following the items listed below.

- Matching the data taken by HD- and HBX- DAQ
- Selection of Ge hit events with a TDC gate
- Energy calibration
- Background suppression by BGO

In addition, the performance of Hyperball-X, i.e, energy resolution and efficiency, is described in the later part of this chapter.

3.2.1 Event selection and calibration

Matching the data taken by HD- and HBX- DAQ

The data of Hyperball-X were taken by the HBX-DAQ system which was independent of the HD-DAQ system explained in subsection 2.4.3. On the HD-DAQ side, data were acquired with the KK trigger, while on HBX-DAQ, data were acquired with the Ge∩KK trigger. The data from each of the DAQs were synchronized using the spill and event numbers. In addition, a time stamp was distributed and its TDC value was recored by both DAQ systems. This TDC value was used to ensure that the data sets belong to the same KK trigger. The correlation between the time stamp TDC value taken in the HBX DAQ (clock_{HD}) and that taken in the HD DAQ (clock_{HBX}) is shown in Fig 3.2. This is for the data of one emulsion module. We accepted events in the area enclosed by the black lines as shown in the figure, and events within this area was used for each module.

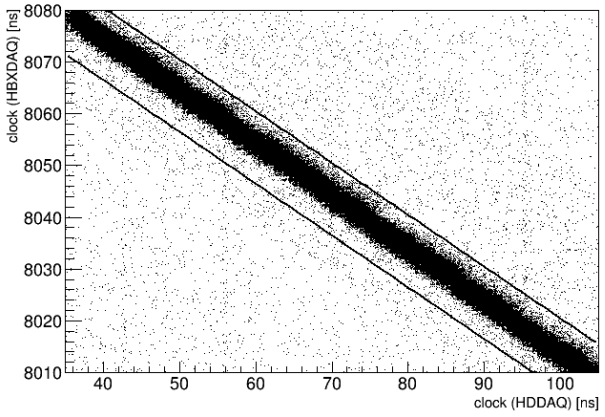

Figure 3.2: Correlation of clock values measured with HD DAQ and HBX DAQ.

Selection of Ge hit events with a TDC gate

For the data taken by the Ge∩KK trigger, the timing of Ge hit was selected to identify which Ge detector had a signal. The common stop signal for the Ge hit TDC was the Ge∩KK trigger. The timing resolution of the Ge detector depends on γ-ray energy. The TDC distributions of a clover-type and a single-type Ge detector are shown in Fig. 3.3. They depend on the ADC value. The distributions are shown for four ranges of ADC channels, (1) 0 - 500, (2) 500 - 1000, (3) 1000 - 1500, (4) 1500 - 8000 (unit is an ADC channel). Note that the gain of the Ge detectors was adjusted to ∼0.2 keV/channel. The four ranges are described in unit of keV, as (1) 0 - 100 keV, (2) 100 - 200 keV, (3) 200 - 300 keV, (4) 300 - 1600 keV. The timing resolution of clover-type and single-type detectors were 21 and 14 ns in FWHM at 200 - 300 keV, respectively. They were 80 ns and 140 ns, respectively, at 100 - 200 keV.

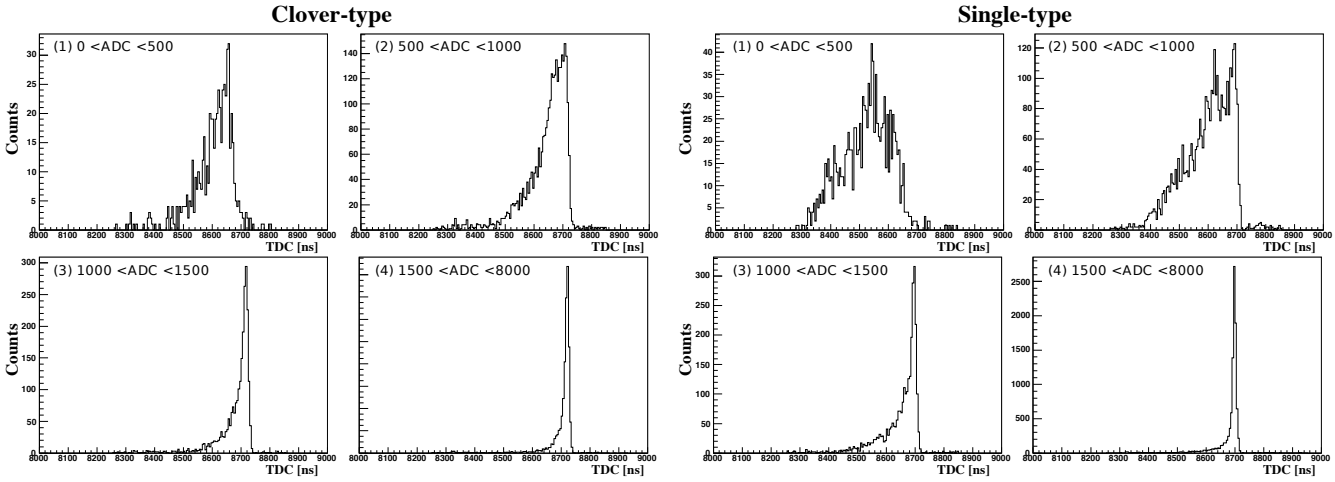

Figure 3.3: TDC distribution of Ge detector.

Accordingly, the gate width of TDC depends on the ADC value. A correlation between ADC and TDC for a clover-type detector is shown in Fig. 3.4. The TDC gate as shown in red lines was set for every Ge detector. The higher edge of the gate was fixed to t_0, which was tuned for each Ge detector. The lower boundary t_1 was given by a function of $t_1 = -C_2/(C_1 - t_0)$. The C_1 was adjusted to the peak position of the TDC distribution, and C_2 was a constant common to all the Ge detectors.

Energy calibration

For energy calibration of the Ge detectors, three reference γ rays from LSO (202 keV, 307 keV) and ^{22}Na (511 keV) were used. Usually, the ADC data for each Ge detector were calibrated every one hour. Each γ-ray peak was fitted with a Gaussian function and a quadratic function by the χ^2 method as shown in Fig. 3.5. Correlations between the peak mean value and the energy are

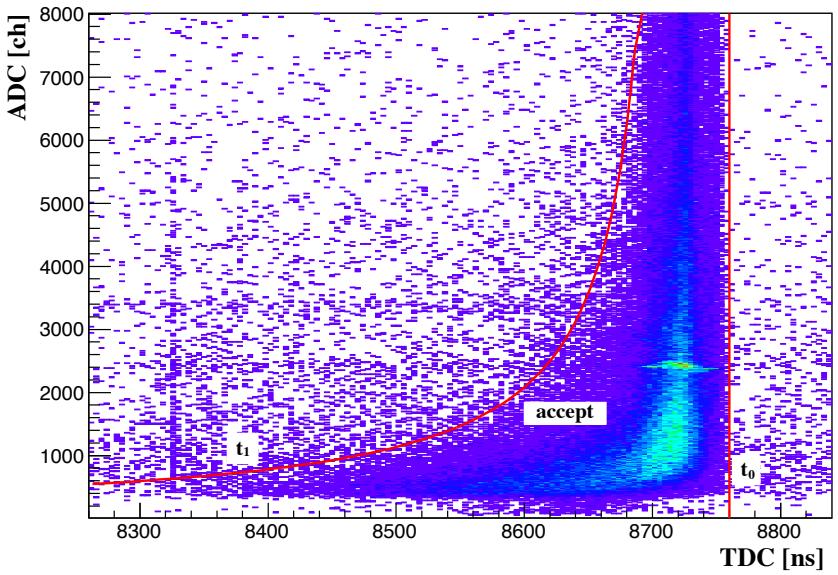

Figure 3.4: Correlation between ADC and TDC of Ge detectors.

fitted by the least squares method with a linear function as follow,

$$y[keV] = a \times x[ADCch] + b, \tag{3.1}$$

where a and b are calibration coefficients. The new calibration method enabled us to calibrate the Ge detectors run by run. The peak mean values of 307-keV γ ray are plotted in Fig. 3.6. The black dots represent the case of calibration with the common parameters for through out the runs, and the red dots is the case of calibration made run by run. The effect of Ge gain drifting in long-term data-taking was corrected for by the new calibration method.

When Eq. 3.1 is employed as a calibration function, the calibration error ($\sigma_{\rm calib}$) for this method can be calculated with an error propagation mothod as follows,

$$\begin{aligned} \sigma_{calib} &= \sqrt{\left(\frac{\partial y}{\partial a}\right)^2 \sigma_a^2 + \left(\frac{\partial y}{\partial b}\right)^2 \sigma_b^2 + 2\left(\frac{\partial y}{\partial a}\right)\left(\frac{\partial y}{\partial b}\right)\sigma_{ab}} \\ &= \sqrt{\left(\frac{y-b}{a}\right)^2 \sigma_a^2 + \sigma_b^2 + 2\left(\frac{y-b}{a}\right)\sigma_{ab}} \end{aligned} \tag{3.2}$$

where σ_a and σ_b are the errors on a and b, respectively, and σ_{ab} is a covariance. σ_a and σ_b are proportional to the peak mean accuracy. Thus, low statical peaks make calibration accuracy worse. As an example, an hour data taken by one of the clover-type Ge crystals (No.1-1) was calibrated, and the resulting residuals for each reference γ-ray energy are represented by black dots in Fig. 3.7. Errors on the points were obtained by peak fitting. The solid magenta line

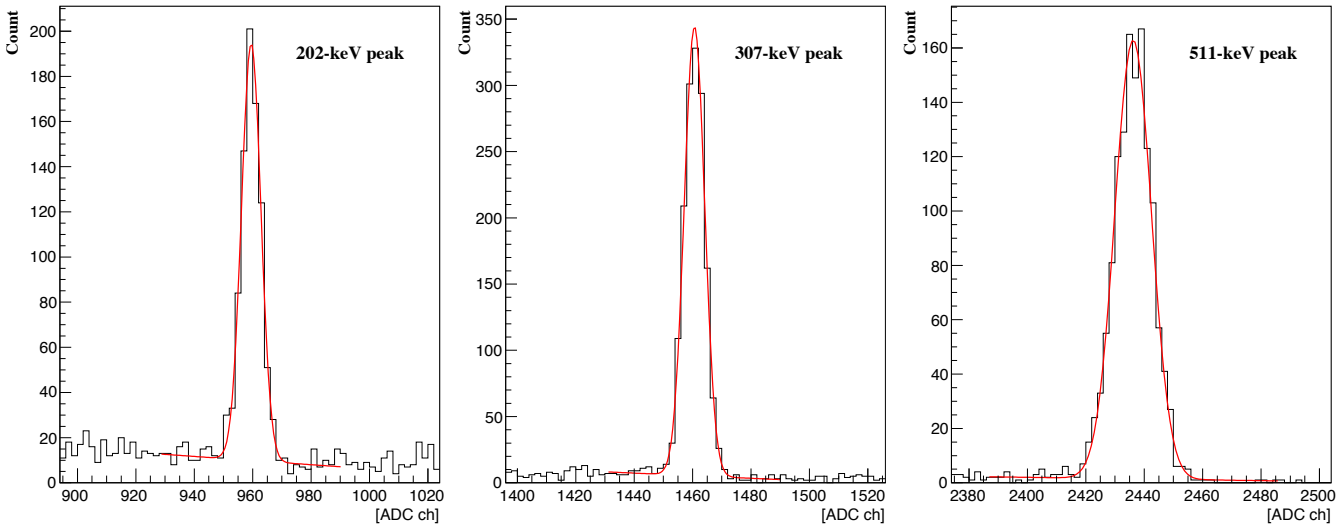

Figure 3.5: Peak fitting of reference γ rays.

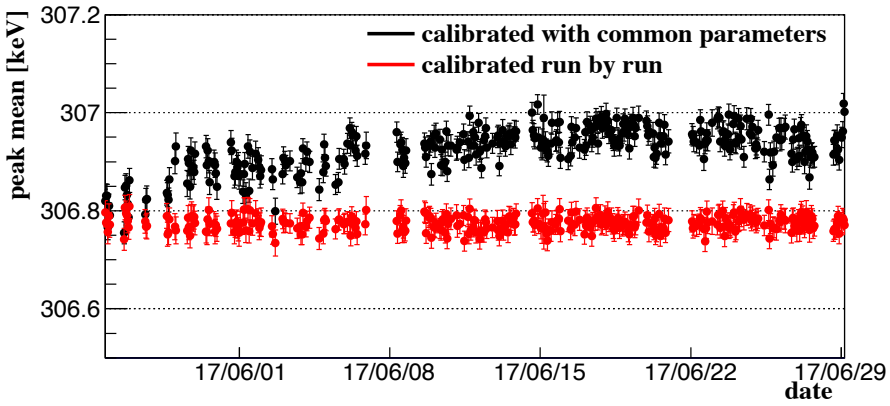

Figure 3.6: The gain drift of Ge detector

represents σ_{calib} calculated with Eq. 3.2. The σ_{calib} was less than ± 50 eV at the interpolated energy region, between 202 keV and 511 keV. For the case of 370-keV X ray, the σ_{calib} was ± 20 eV. Similar or better results were obtained for almost all the other crystals as shown in Fig. 3.8.

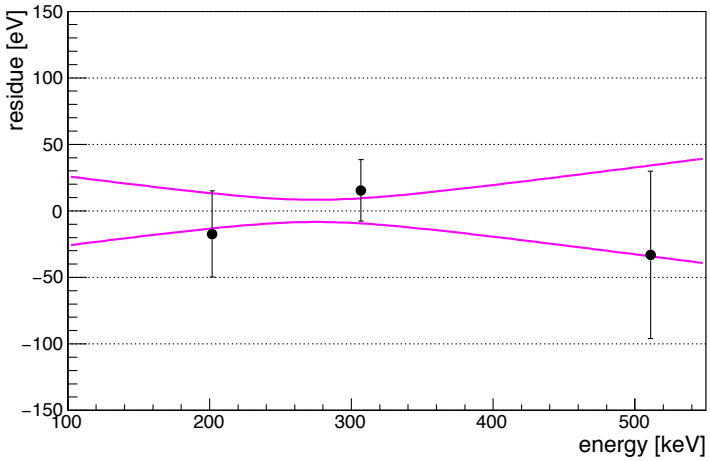

Figure 3.7: Residue for the three reference peaks. It is an hour data taken by clover-type Ge crystal (No.1-e). The calibration error calculated with the error propagation rule is shown in magenta.

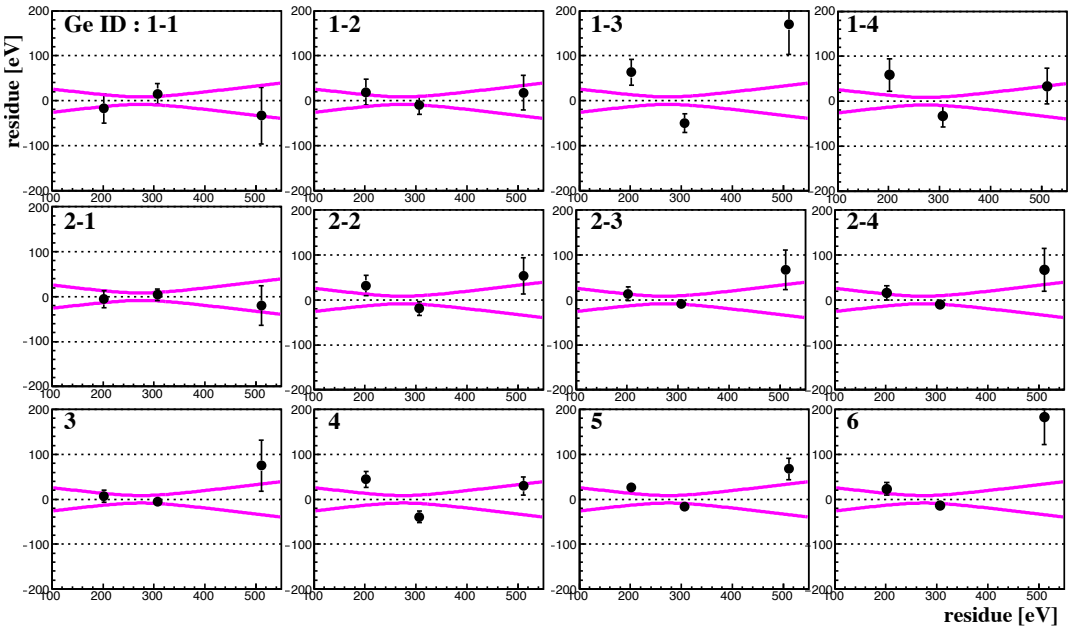

Figure 3.8: Residue for the three reference peaks for all the Ge crystals. This is for an hour data. The calibration errors are shown in magenta.

The validity of this calibration method was checked using γ rays from a ^{133}Ba source. For several hours, the in-beam data was taken with a ^{133}Ba source placed on the target. Four γ rays, between 200 and 400 keV, from ^{133}Ba shown in Table 3.1 were measured and calibrated with the three-point method. The residues were obtained as shown in Fig. 3.9. The black and red dots represent the residues for reference γ rays and γ rays from ^{133}Ba, respectively. This is the result for

one Ge crystal (No.1-1) and γ rays were calibrated with less than 50-eV accuracy. The results of all the other Ge crystal are shown in Fig. 3.10. For some Ge crystals, such as No.1-2 or No.6, the residue has correlation with γ-ray energy. It is possible that the fitting function was not optimized or the linearity of the ADC modules was not enough. As a result, γ rays were calibrated with at least 100-eV accuracy by any Ge detector.

Table 3.1: The γ rays from the ^{133}Ba source.

energy [keV]	intensity [%]
276.398	7.164
302.853	18.33
356.017	62.05
383.851	8.94

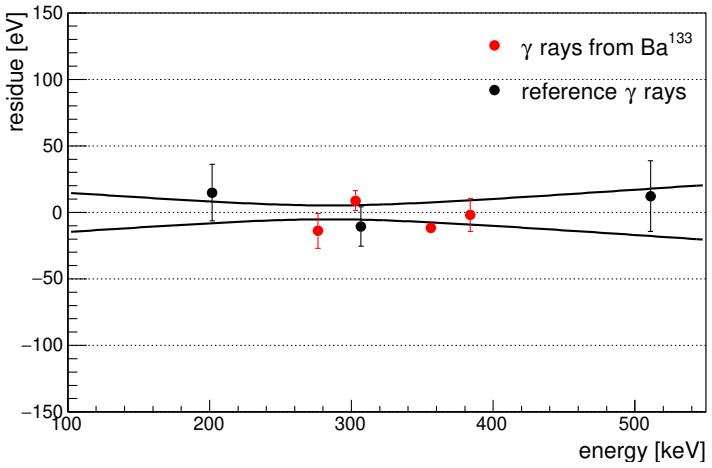

Figure 3.9: Residues for γ rays from ^{133}Ba (shown in red dots). It is an hour data taken by clover-type Ge crystal (No.1). Black dots represent residues for reference γ rays.

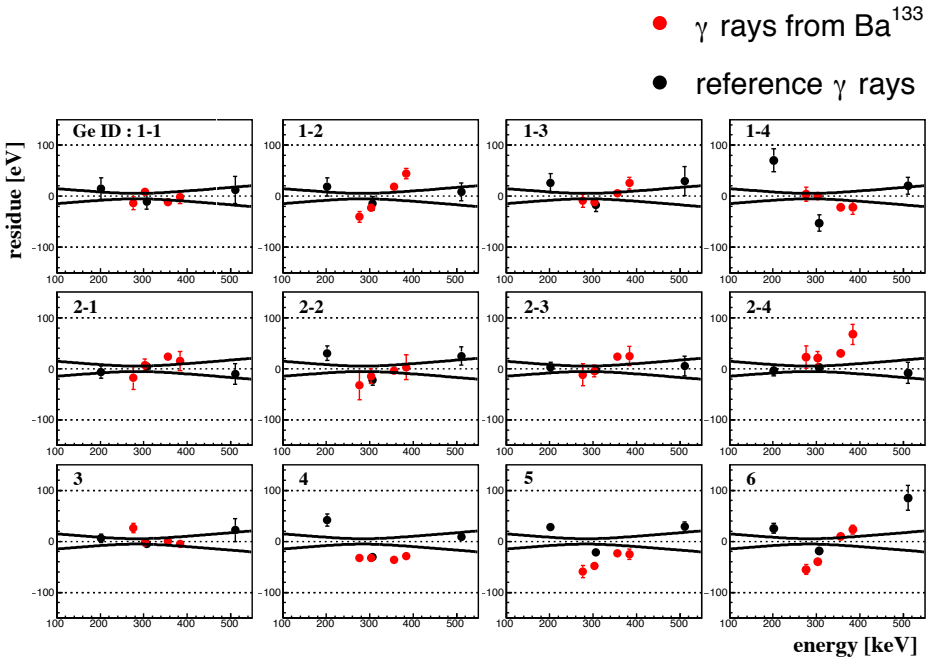

Figure 3.10: Residuals for γ rays from ^{133}Ba (shown in red) and for reference γ rays (shown in blalck) for all Ge crystals.

Finally, the calibration error for one X-ray event depends on a Ge detector that it is measured, thus, the weighted average of the calibration error for the obtained X rays should be regard as a systematic error.

Background suppression by BGO detectors

Using the hit information of the BGO detector, background events are rejected (BGO suppression). The TDC data of the BGO detectors are used as hit information. The TDC distribution is shown in Fig. 3.11, and some region is accepted as events which are synchronized with the Ge∩KK trigger. The upper edge of the gate is fixed to 790 channel. The suppression efficiency and the survival ratio of signals depend on the width of the gate. They are evaluated using 718-keV γ ray from ^{11}B produced by the beam on the ^{12}C target. In Fig. 3.12, the gate width dependence of the peak significance ($S/\sqrt{N}$) is shown. When the gate width is less than 50 ns, the $S/\sqrt{N}$ is increased greatly with expansion of the gate. On the other hand, when the gate width is larger than 50 ns, $S/\sqrt{N}$ is increased gradually and tends to plateau with over 70-ns width. Thus, 50-ns width is employed as the BGO gate.

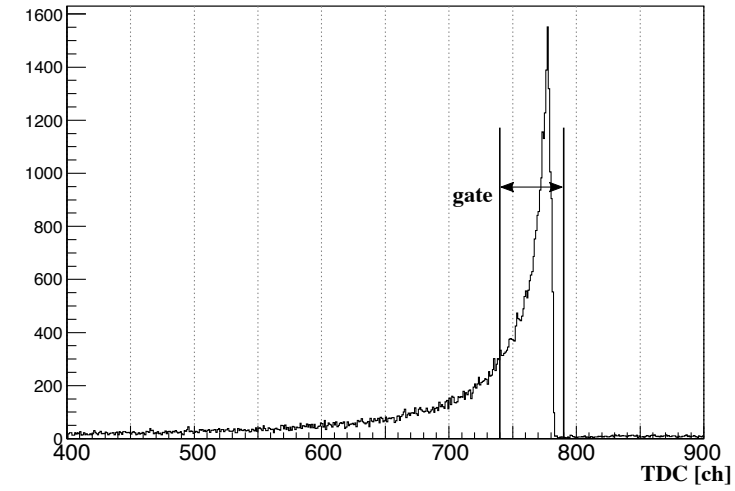

Figure 3.11: TDC distribution of the BGO detector.

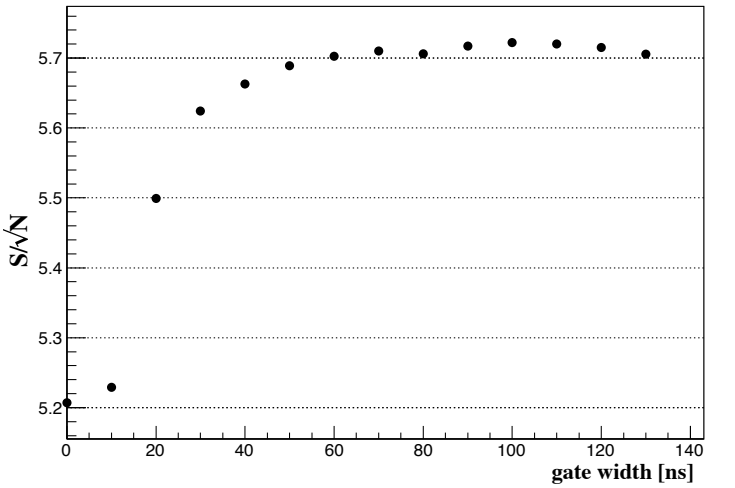

Figure 3.12: The gate width dependence of peak significance ($S/\sqrt{N}$).

The gate width dependence of the survival ratio for the 718-keV γ-ray signal is shown in Fig. 3.13. When the gate width is 50 ns, the survival ratio of signal is 84%.

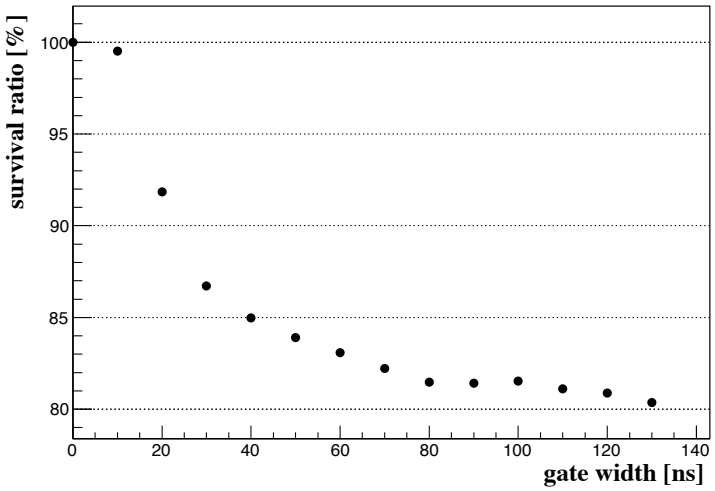

Figure 3.13: The gate width dependence of the 718-keV γ-ray signal survival ratio.

3.2.2 Performance of Hyperball-X

Energy resolution

The energy resolution of the Ge detectors is evaluated using γ rays from the ^{152}Eu nucleus as shown in Table 3.2. The energy dependence of the resolution (in FWHM) is shown in Fig. 3.14. This correlation can be written in the following equation.

$$\delta E = aE_{\gamma}^{1/2} + bE_{\gamma} + c \tag{3.3}$$

where a, b and c are coefficients, E_{γ} is the energy. The first term which depends on the square root of the γ-ray energy represents uncertainty of the number of electron-hole pairs produced by γ-ray interaction. Empirically, uncertainty in carrier collection is proportional to the energy. The third constant term is caused by electric noise which is independent of the energy. The fitted value of a,

Table 3.2: The γ rays from the ^{152}Eu source.

energy [keV]	Intensity [%]
121.78	28.58
244.6975	7.583
344.2785	26.5
443.965	2.821
778.9040	12.942
964.079	14.605
1112.074	13.644

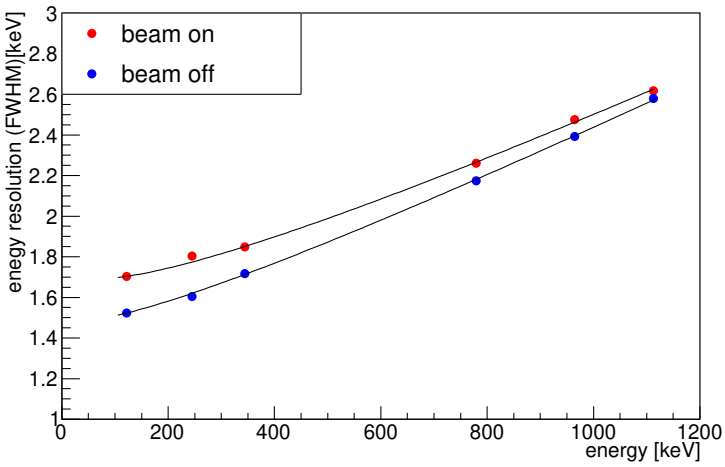

Figure 3.14: Energy dependence of energy resolution. The resolution is evaluated using γ-ray peaks of ^{152}Eu.

b, and c are $2.3 \times 10^{-2}, 1.5 \times 10^{-3}$, and 1.8, respectively, for the on-beam data and the resolution is 1.9 keV (FWHM) at 370 keV.

The live time of Ge detector

Operating the Ge detectors under high counting rate environment lowers their live time. Energies are processed incorrectly in the readout electronics when the signals input to ADCs are piled up and distorted. In addition, high reset rate increases a dead time due to the baseline distortion after a transistor reset. Counting rates of the Ge detectors were 2$\sim$3 kHz for the clover-type and 4$\sim$5 kHz for the single-type detector. The intensity of the beam supplied from the accelerator was not stable. At the time when the instantaneous beam intensity is extremely high, it is possible that pile up and a reset rate increase significantly. The live time under such a beam environment was evaluated using γ rays from a ^{60}Co source. It is defined as

$$\text{Live time} = \frac{\text{counts of } \gamma \text{ rays which wave correctly processed by readout electronics}}{\text{counts of original } \gamma \text{ rays giving a signal in the Ge detector.}} \tag{3.4}$$

To evaluate the live time under the data-taking condition, γ rays were counted with the "beam trigger" which was a pre-scaled timing signal of the beam hodoscope (BH2). Since the original γ rays were not able to be counted, the data in which the live time achieves 100% were also taken as a reference. The counts of γ rays detected during the off-beam period was regarded as that of the original γ rays. The data was also taken with the "random trigger" which was a clock signal and has no correlation to the instantaneous beam intensity during both on-beam and off-beam periods. The conditions and results are summarized in Table 3.3. The live time for Ξ^- atomic X rays synchronized to the beam was found to be 88$\pm$1%. On the other hand, the live time for γ

Table 3.3: Live time of Ge detectors.

	trigger	beam	live time [%]
(1)	clock	off	reference
(2)	clock	on	95±1
(3)	beam (pre-scaled)	on	88±1

rays from the LSOs and ^{22}Na sources, corresponding to the condition of the random trigger, was 95±1%. The error comes from statistics of the γ rays.

Photo-peak efficiency

The photo-peak efficiency ($\epsilon_{\rm photopeak}$) depends on where X rays are generated and absorbed by materical. It is evaluated for X rays from the emulsion and from the target separately.

Efficiency for X rays from the center position of the emulsion

The photo-peak efficiency for X rays emitted from the emulsion was evaluated considering both of absolute value and energy dependence.

Firstly, the absolute value of the efficiency was measured. Cascading two γ rays from a reference source were detected by a Ge detector and a reference detector, respectively. A NaI detector was used as a reference detector. The efficiency was calculated as the ratio of the number of γ rays detected by the NaI detector to that detected by the Ge detector. Advantage of this method is that the absolute value is determined even without knowing the source intensity exactly. As reference γ rays, 1173-keV and 1332-keV γ rays from ^{60}Co were used. They are emitted in cascade with a branching ratio of 99.9% (see Fig. 3.15). The efficiency is given by

$$\text{eff.} = (N_{\gamma 1173\text{Ge}} - N_{\gamma 1333\text{Ge}})/N_{\gamma 1333\text{NaI}}, \tag{3.5}$$

where $N_{\gamma 1173\text{Ge}}$ is the number of counts of the 1173-keV γ rays detected by the Ge detector, $N_{\gamma 1333\text{NaI}}$ is the number of counts of the 1333-keV γ ray detected by the NaI detector. The γ-ray spectra detected by the NaI and Ge detectors are shown in (a) and (b) in Fig. 3.16, respectively. As shown in (a), a region from 1330 to 1450 keV is selected as the 1333-keV γ ray ($N_{\gamma 1333\text{NaI}}$) in order to avoid contamination of the 1173-keV γ ray. A γ-ray spectrum detected by the Ge detectors when the 1333-keV γ ray was selected is shown in (b). As shown in (b), there were 1333-keV γ rays detected in accidental coincidence. The 1173-keV peak should have a similar amount of accidental contamination to be subtracted. The number of detected 1173-keV γ rays by the Ge detector should be corrected considering the following two points. The two γ rays from ^{60}Co have an angular correlation. It is corrected depending on the angle between the Ge detector and the NaI detector. In addition, a correction for the live time of the Ge detector should be considered. The live time of the Ge detector decreased due to the ^{60}Co source activity of about 4.2×10^5 Bq. It

was evaluated to be 84±1% using 306-keV γ ray from the LSO during the off-beam period. Thus, the absolute efficiency for all the Ge detectors was measured to be 0.84±0.05(stat.)% at 1117 keV. Only statistical error for γ rays detected by the Ge detector was employed because the others were small enough to be ignored.

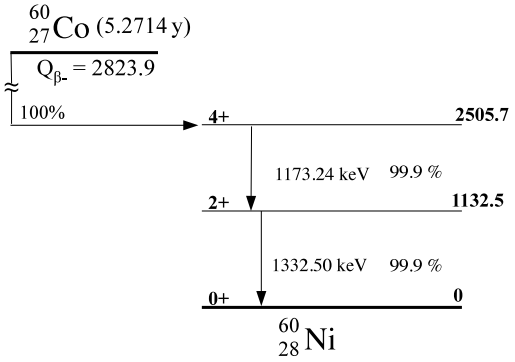

Figure 3.15: The decay scheme of ^{60}Co.

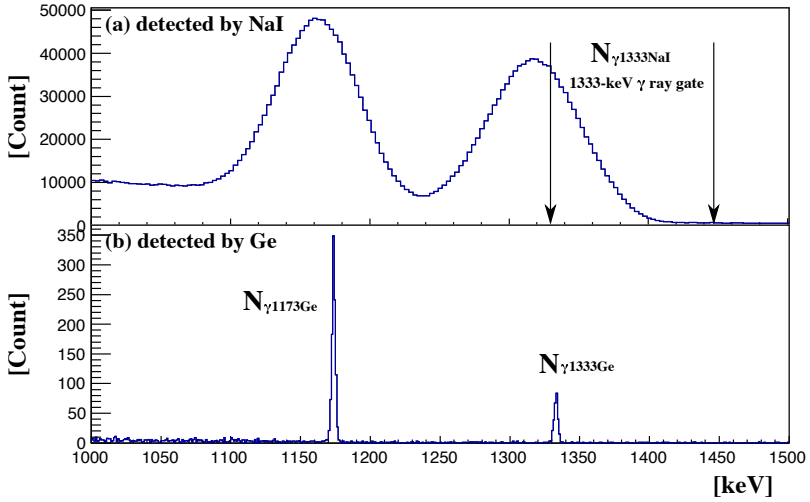

Figure 3.16: The γ-ray spectrum of 1173-keV and 1333-keV γ rays from ^{60}Co by a NaI detector (a) and a Ge detector (b) for the measurement of the absolute efficiency.

Secondly, the energy dependence of the photo-peak efficiency is studied using γ rays from ^{152}Eu during the off-beam period. The energies of six reference γ rays from ^{152}Eu are shown in Table 3.2. A ^{152}Eu source was put at the center of the emulsion module, in which emulsion was not installed. The activity of the ^{152}Eu source was 1.27×10^4 Bq with 3.8% uncertainty at the time of the measurement. The efficiencies measured for these reference γ rays are shown in black dots in Fig. 3.17. This result is reproduced by a Geant4 simulation. The efficiency curve estimated by the simulation is shown in red in the figure. Note that the result of the simulation is scaled to the measured data. This is because the effective volume of each Ge detector which depends on the

electrodes and detailed shape of the crystal was not reproduced completely in Geant4 simulation. In order to reproduce the measured efficiency shown in Table 2.7, the result of the simulation was multiplied by a factor of around 0.8. The simulated value for the 1117-keV γ ray is different by 0.13% from the measured value, as shown in a blue dot of the absolute efficiency. This is because the intensity of a ^{152}Eu source had an uncertainty. The simulation result is scaled to reproduce the measured absolute efficiency within the error, and the scale factor is 1.18.

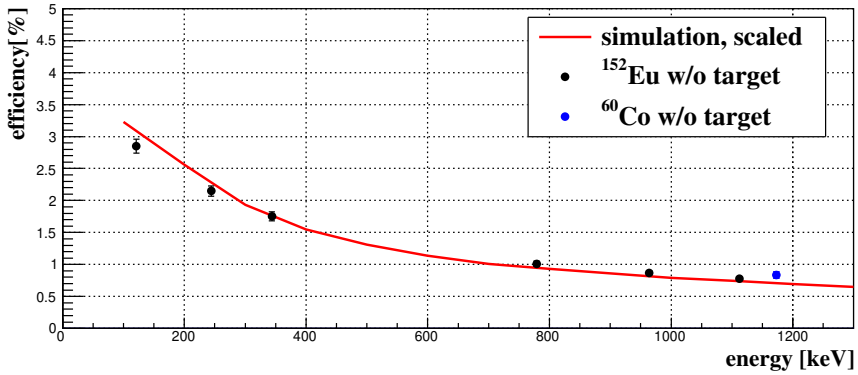

Figure 3.17: The efficiency curve for γ rays emitted from the center position of the emulsion. The measured energy dependence of the efficiency without the target is plotted in black dots. The absolute value for 1173-keV γ ray measured with a ^{60}Co standard source is shown in a blue dot. The simulated efficiency curve without the target is shown in red.

Thirdly, γ-ray absorption by material is studied. Absorption by the diamond target was measured. The efficiencies with and without the target are shown in black cross and dots, respectively, in Fig 3.18. These results are compared to the simulated efficiency curves with and without target, as shown in blue and red line in the figure. For the case with the target, the efficiencies of the data and the simulation are different by 0.05% at 344 keV. This is considered as a systematic error.

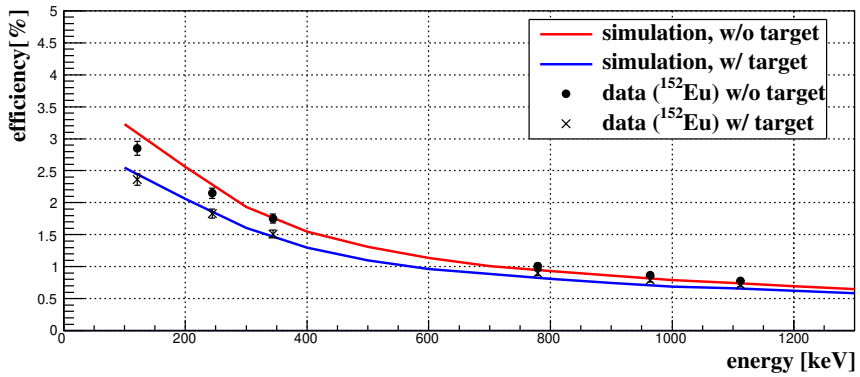

Figure 3.18: The effect of γ-ray absorption by the target. The dots and crosses represent a measured efficiency with and without the target.

Finally, the photo-peak efficiency which also takes into account the absorption by the emulsion was estimated by simulation. Considering the scale factor to reproduce the absolute value, the estimated efficiency curves (1) without material, (2) with the target, and (3) with the target and the emulsion, are shown in red, blue and black line, respectively, in Fig.3.19. About 50% of 300-keV γ ray from the center of the emulsion module is absorbed by the target or the emulsion. After all, the efficiency for the 370-keV γ ray was obtained to be 0.99 $\pm$ 0.05(stat.) $\pm$ 0.05(sys.)%.

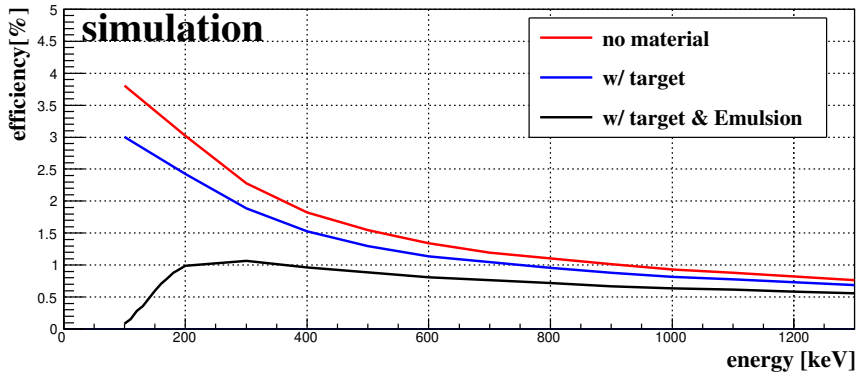

Figure 3.19: The simulated efficiency curves. They are estimated for the conditions (1) without material, (2) with the target, and (3) with the target and the emulsion, as shown in red, blue and black, respectively.

Efficiency for X rays from the target

The efficiency for X rays generated in the diamond target was also estimated. This was evaluated for the 150-keV X ray from Ξ^-C atom. The efficiency for the reference γ rays from ^{133}Ba and ^{152}Eu sources on the empty target holder was measured. The result is shown by black dots in Fig. 3.20 and, it is consistent with the result of Geant4 simulation represented by a red line, although the

curve is scaled considering the same reason as already discussed. The difference from the measured efficiency comes from the uncertainty of ^{152}Eu source intensity was considered as same as discussed above. By considering absorption by the target, the efficiency for γ ray generated uniformly inside the target was estimated by simulation as shown in the blue curve in Fig. 3.20. After all, the efficiency for the 154-keV γ ray was obtained to be 1.55 $\pm$ 0.05(stat.) $\pm$0.05(sys.)%.

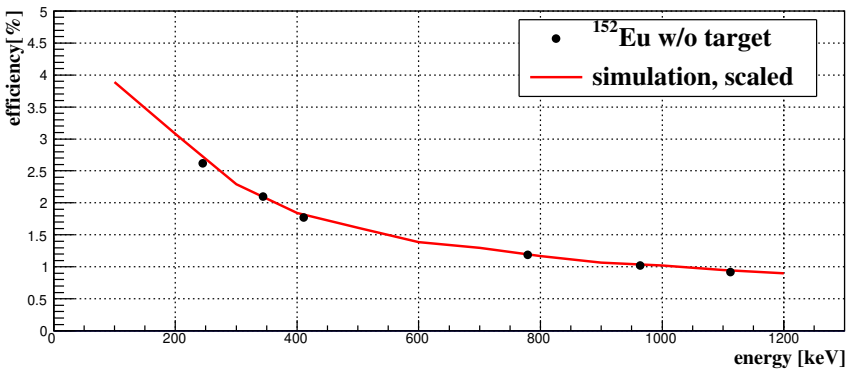

Figure 3.20: The efficiency curve for γ rays emitted from the target. The measured efficiency without the target is plotted in dots. The simulated efficiency curves with and without absorption by the target are shown in red and blue, respectively.

Total efficiency

Finally, the total efficiency of Hyperball-X is given by a produce of the live time of the Ge detectors, the photo-peak efficiency and the DAQ efficiency as follows,

$$\epsilon_{\mathrm{Total}} = live\ time \times \epsilon_{\mathrm{photopeak}} \times \epsilon_{DAQ}. \tag{3.6}$$

The DAQ efficiency during the Ξ^- production period was 95%. The total efficiency was 0.83 $\pm$ 0.07% at 370 keV for X rays from the center of the emulsion and 1.30 $\pm$ 0.07% at 154 keV for X rays from the target.

3.3 Analysis of the (K^-, K^+) reaction

In this section, the analysis of the (K^-, K^+) reaction is described. It was applied to both of case1 and case2 analysis. The momentum of beam particles and scattered particles were analyzed by the beam line spectrometer and the KURAMA spectrometer, respectively. Then, K^- and K^+ particles were identified by the time-of-flight value or the mass calculated by the velocity. The vertex point of the (K^-, K^+) reaction was reconstructed by the K^- and K^+ tracks, and the missing mass and the momentum were also reconstructed. Detailed items for the analysis are listed as follow.

- Momentum reconstruction of K^-
- Incident K^- identification by time-of-flight
- Momentum reconstruction of K^+
- Scattered K^+ identification by a mass
- Reconstruction of a vertex point of the reaction
- Reconstruction of the missing mass.

The procedure of analysis was the same in both cases but the selection conditions were different. Details of the optimized selections for case1 and case2 are explained in Section 3.4 and Section 3.5, respectively.

3.3.1 Analysis of K^-

Reconstruction of K^- track and momentum

The position (x, y), angle (x', y'), and momentum (p) of the incident particle at upstream of Q10 $(x_{up}, y_{up}, x'_{up}, y'_{up}, p)$ and at downstream of Q13 $(x_{down}, y_{down}, x'_{down}, y'_{down}, p)$ are related by the transfer matrix (M) corresponding to the magnetic fields of the magnets of the K1.8 beam line spectrometers (QQDQQ) as follows,

$$\begin{pmatrix} x_{up} \\ y_{up} \\ x'_{up} \\ y'_{up} \\ p \end{pmatrix} = M^{-1} \begin{pmatrix} x_{down} \\ y_{down} \\ x'_{down} \\ y'_{down} \\ p \end{pmatrix}. \tag{3.7}$$

M was calculated by TRANSPORT. M^{-1} is the inverse matrix of M. We had five simultaneous equations. When the five values $(x_{up}, x_{down}, y_{down}, x'_{down}, y'_{down})$ were given from measurement, the four unknowns $(y_{up}, x'_{up}, y'_{up}, p)$, were calculated from Eq. 3.7. At upstream of the Q10 magnet,

x_{up} was measured by BFT. At downstream of Q13, $(x_{down}, y_{down}, x'_{down}, y'_{down})$ was obtained by tracking analysis of BC3 and BC4. BC3 and BC4 each having 4 layers measured the hit positions of the beam particle. The beam track was obtained as a straight track with the least χ^2 fitting method by using hit positions at BC3 and BC4. The χ^2 value is defined as

$$\chi^2 = \frac{1}{n}\sum_{i=1}\left(\frac{P_i - f(x_i)}{\sigma_i}\right)^2, \tag{3.8}$$

where n is the degree of freedom, P_i is the hit position of the i-th layer, $f(x)$ is the assumed linear function, σ_i is the position resolution of i-th layer. When there were multiple hits in BFT, BC3, and BC4, multiple tracks were considered for all combinations. After analysis of BFT, BC3, and BC4, the four unknowns $(y_{up}, x'_{up}, y'_{up}, p)$ were obtained. The obtained momentum of the incident particle is shown in Fig. 3.21.

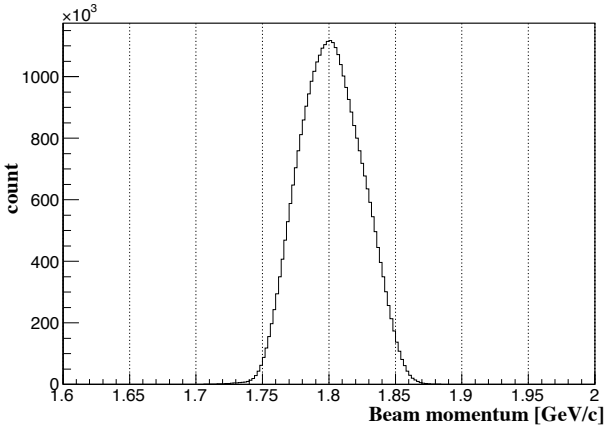

Figure 3.21: The reconstructed momentum of incident particles.

K^- identification by time-of-flight

The mass of the beam particle is calculated from the time-of-flight and the measured momentum. The momentum bite of the beam line spectrometer was as small as ±3%. The time-of-flight between BH1 and BH2 which mainly contribute to the mass distribution was used to identify the K^- beam. The distance between BH1 and BH2 was 11.2 m. For the case of beam particles of 1.8 GeV/c momentum, the difference of the time-of-flight was 1.27 ns between K^- and π^-. The distributions of the time-of-flight are shown in Fig. 3.22. Black and red show the distributions taken by the BH2 trigger and the KK trigger, respectively. The peak seen only in red represents the K^- particles.

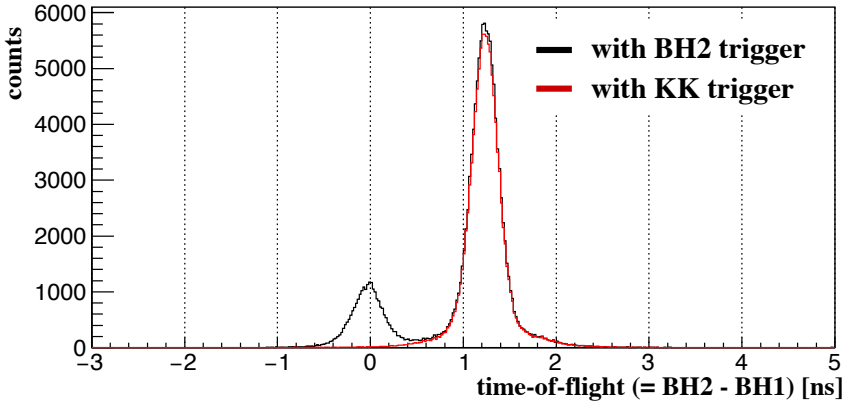

Figure 3.22: The distribution of time-of-flight (=BH2-BH1).

3.3.2 Analysis of K^+

Reconstruction of K^+ track and momentum

The track of the scattered K^+ was obtained by analysis of the KURAMA spectrometer. Firstly, the track of the scattered particle was reconstructed at upstream and downstream of the KURAMA dipole magnet (KURAMA-Up and -Down side), independently. At the KURAMA-Up side, there were three types of trackers, SSD, SDC1 and SCH, having 15 layers in total. At the KURAMA-Down side, there were two drift chambers, SDC2 and SDC3, having 8 layers in total. In local tracking at the Up side and the Down side, a track was fitted by a linear function. Then a track under the magnetic field was reconstructed by solving the equation of motion over a certain step, of which solution is used to calculated the next step; the numerical method so-called Runge-Kutta method [37] was employed. As initial values, the particle position and the velocity reconstructed by the KURAMA-Down side tracking were used. The magnetic field of the KURAMA magnet was calculated using TOSCA code [38] with the finite element method. The strength of the magnetic field was being monitored by an NMR probe during the experiment. The reconstructed track is validated based on χ^2_{KURAMA} given as

$$\chi^2_{KURAMA} = \frac{1}{n}\sum_{i=1}^{n}\left[\frac{x_i^{data} - x_i^{tracking}}{\sigma_i}\right]^2, \tag{3.9}$$

where n is a number of the layer, x_i^{data} is the measured hit position on the i-th layer, $x_i^{tracking}$ is the reconstructed hit position on the i-th layer. The distribution of χ^2_{KURAMA} is shown in Fig. 3.23. Tracks with χ^2_{KURAMA} less than 30 were accepted.

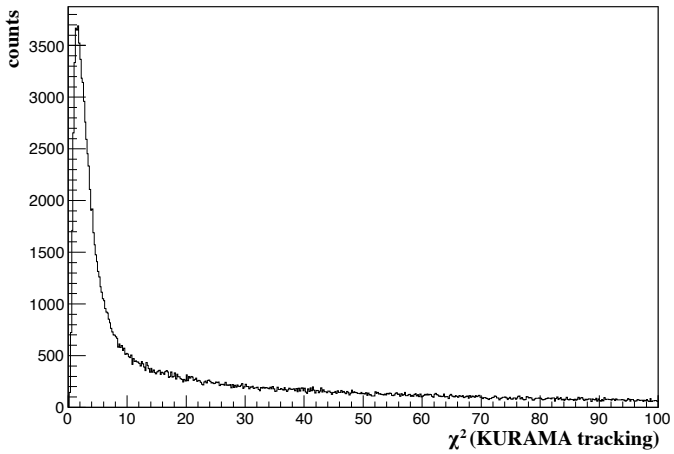

Figure 3.23: χ^2 of the KURAMA tracking.

Identification of K^+ by mass

The mass of scattered particles (M_{sca}) is calculated from β and momentum (p_{sca}), as follows,

$$M_{sca} = \frac{p_{sca}}{\beta}\sqrt{1-\beta^2}. \tag{3.10}$$

The flight path length between the target and the TOF detector was calculated from the KURAMA tracking. The time of flight between them was also measured, and thus β of scattered particle was calculated. As seen in the mass squared distribution of positive charged particles shown in Fig 3.24, the scattered K^+ was contaminated with π^+ and proton. For particle identification, the mass squared was selected in both of case1 and case2.

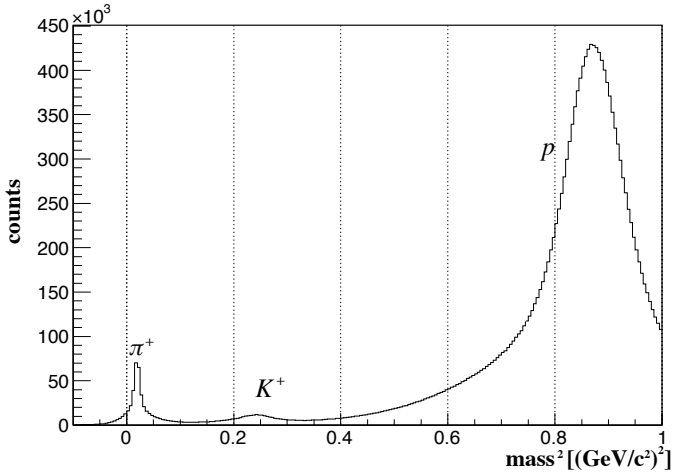

Figure 3.24: The mass square distribution of positive charged particles.

The obtained momentum distribution of scattered K^+ is shown in Fig. 3.25. For this distribution, the mass of the scattered particles was roughly selected, $0.19 < mass^2 < 0.29$ $[(\mathrm{GeV}/c^2)^2]$,

as a K^+ particle.

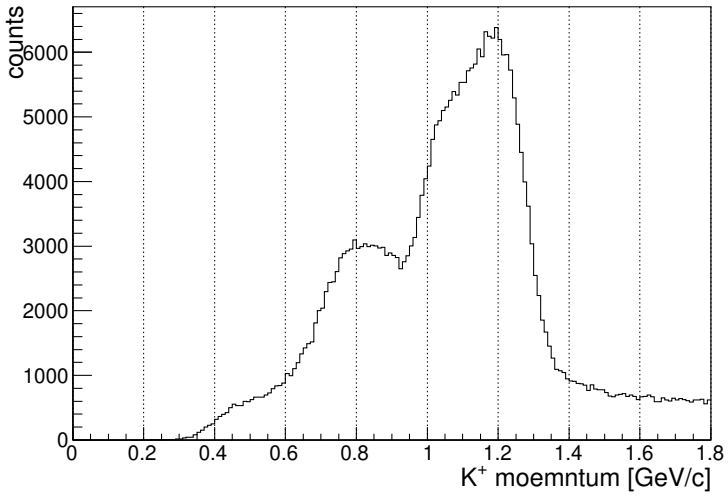

Figure 3.25: The momentum distribution of scattered K^+.

Several (K^-, K^+) processes contribute to this momentum distribution. They were investigated in the past experiment and reported in references [6][8]. For the obtained missing mass distribution, the contribution of the other possible one-step quasifree processes in the (K^-, K^+) reaction is estimated. The possible (K^-, K^+) processes are

- (a) $K^- p \to K^+ \Xi^-$,
- (b) $K^- p \to K^+ \Xi^{-*}(1530)$,
- (c) $K^- p \to K^+ \Xi^- \pi^0$,
- (d) $K^- p \to K^+ \Xi^0 \pi^-$.

Next, meson-induced two step strangeness exchange process,

$$K^- N \to \pi Y,$$
$$\pi N \to K^+ Y,$$

where Y is Λ, Σ or $\Sigma^{\pm}$ also contribute.

According to a reference [8], Λ production associated with scaler and vector mesons may exist as follows,

$$K^- p \to f_0(975)\Lambda,\ a_0(980)\Lambda,\ \phi\Lambda$$
$$f_0/a_0/\phi \to K^- K^+.$$

The peak around $p_{K^+} = 1.2$ GeV/c is mainly due to Ξ^- production via the process (a).

3.3.3 Reconstruction of the (K^-, K^+) reaction

Using the obtained K^- and K^+ tracks, the (K^-, K^+) reaction was reconstructed. That is, the reaction angle, the vertex point, the missing mass and the missing momentum were obtained.

Reconstruction of the reaction angle

When the K^- beam reacted downstream of the target, it was possible that some of the tracking detectors measure the K^- track. In that case, a wrong θ_{K^+} made a background peak in the forward direction. The distribution of the reaction angle (θ_{K^+}) which is the angle between tracks of incident K^- and scattered K^+ is shown in Fig. 3.26. To reject the background, $\cos\theta_{K^+}$ less than 0.996 was selected as the scattered angle.

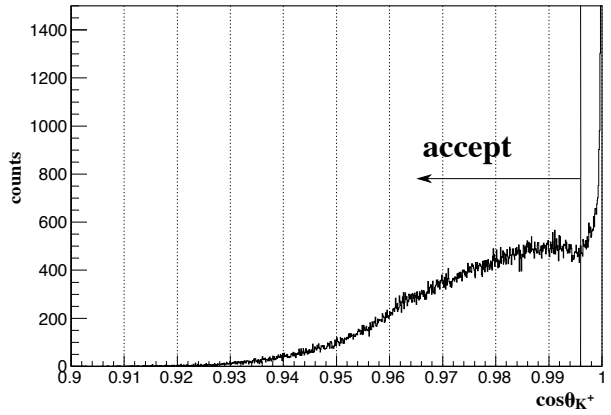

Figure 3.26: Reaction angle (θ_{K^+}) distribution.

Reconstruction of the vertex point

The vertex point was reconstructed as the center of the closest distance of the K^- and the K^+ tracks. The distribution of the closest distance is shown in Fig. 3.27.

By the reconstructed vertex point, those events in which the K^- reacted at the target region were selected. The vertex x distribution is shown in Fig. 3.28 and the target region was $-25 < x < 25$ mm. The target size was limited, and it did not cover the beam region completely. There was a sudden drop at x of 25 mm, corresponding to the edge of the target. The vertex y distribution is shown in Fig. 3.29 and the target region was $-15 < y < 15$ mm.

The obtained vertex z distribution is shown in black in Fig 3.32. SSD1, which had 4 layers ($xyx'y'$), and the emulsion were located downstream of the target. Thus, not only the events in which K^- reacted at the target, but also at SSD1 and the emulsion were included.

Distribution of the vertex in the target, SSD1, and the emulsion was separately obtained when the events were strictly selected using a residue between a SSD1 hit position and a KURAMA

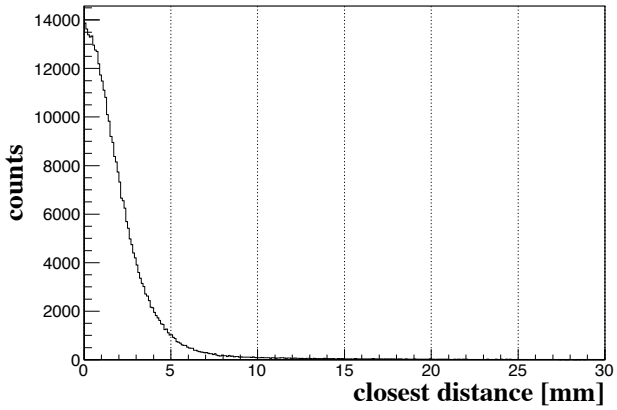

Figure 3.27: The closest distance between K^- and K^+ tracks.

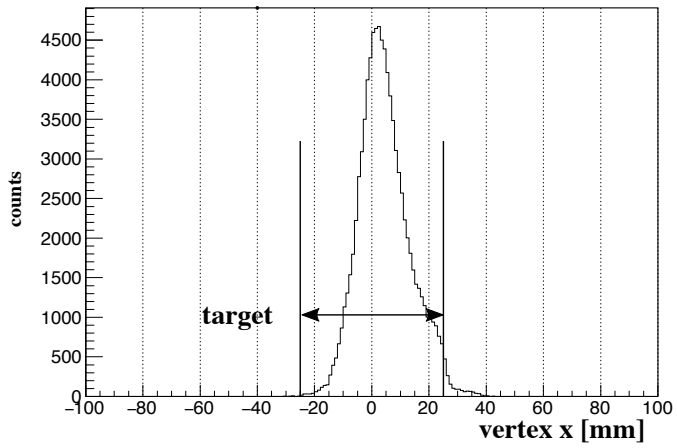

Figure 3.28: The reconstructed vertex point x

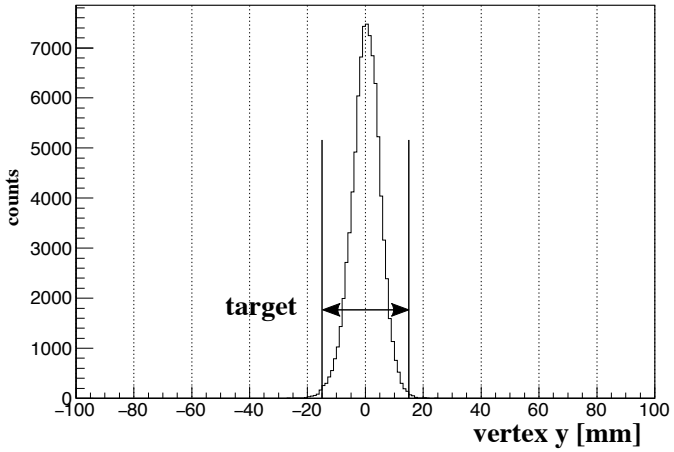

Figure 3.29: The reconstructed vertex point y

track. The residue at the first layer of SSD1 is shown in Fig 3.30. When the K^- reacted at the target as shown in (1) of Fig. 3.31, the residue should be small. By selecting the event that the residues were less than 0.1 mm at all the 4 layers, the distribution was obtained as shown in red. This distribution is consistent with the location of the target that is at the $-15 < z < 15$ mm. When the K^- reacted at layer x' or y' of SSD1 as shown in (2) of the figure, the residues should be small but that of layer x or y should be large. By selecting the event that the difference between the residues of the layer x and x' (y and y') were larger than 0.1 mm, the distribution was obtained as shown in blue. The distribution is consistent with the location of the SSD1 which is at the $20 < z < 22$ mm region. When the K^- reacted at the emulsion as shown in (3) of the figure, the residues at all layers should be large. In the case of a large scattering angle of K^+ , the residue of the first layer may be much larger than that of the fourth layer. By selecting the event that the residue of the fourth layer was less than 0.1 mm and that of the first layer was larger than 0.1 mm, the distribution was obtained as shown in magenta. The distribution is consistent with

the location of the emulsion that is at the $23 < z < 34$ mm region.

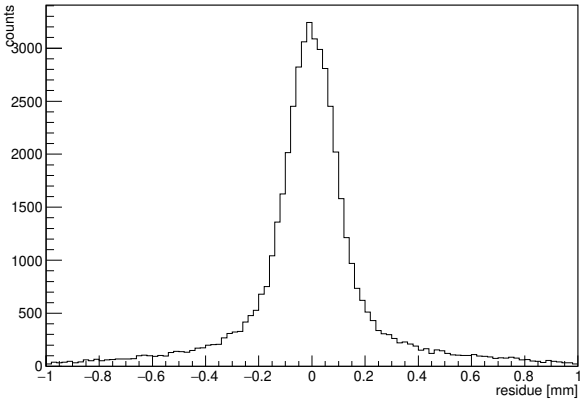

Figure 3.30: The distribution of residue between the Ξ^- track reconstructed by KURAMA analysis and the hit position at the first layer of SSD1.

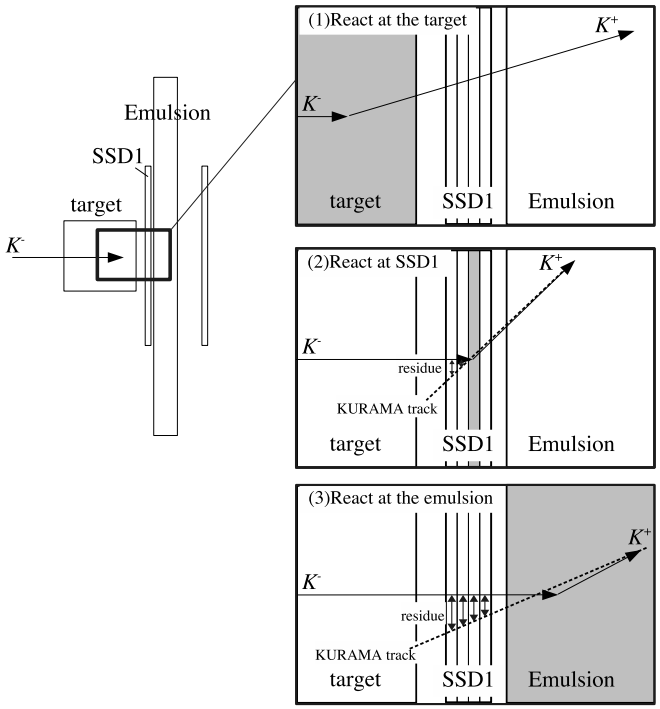

Figure 3.31: The schematic drawing around SSD1. When the K^- reacts at the target as shown in (1), the residues at SSD1 are small. In (2), a dashed line represents the K^+ track reconstructed by KURAMA analysis. When the K^- reacts at SSD1, only the residues at downstream layer of SSD1 are small. As shown in (3), the residues of all the layers are large in particular when the K^- reacts at the emulsion.

For the vertex point of z in the beam direction, a correlation with the reaction angle (θ_{K^+}) was

checked. The resolution of the vertex in z did not depend on the reaction angle strongly as shown in Fig 3.33. Therefore, z of the vertex point was selected regardless of the reaction angle.

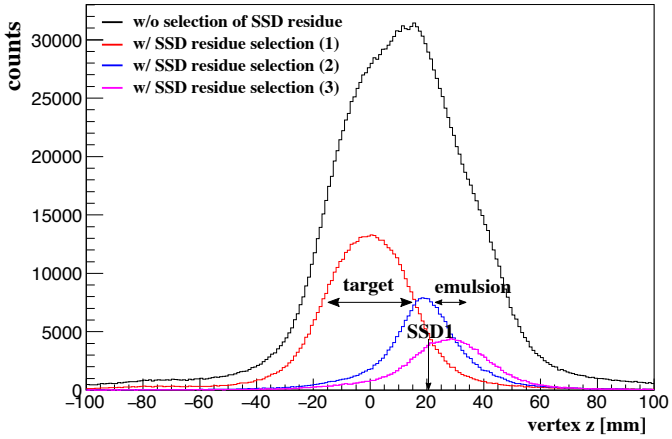

Figure 3.32: The reconstructed vertex point z

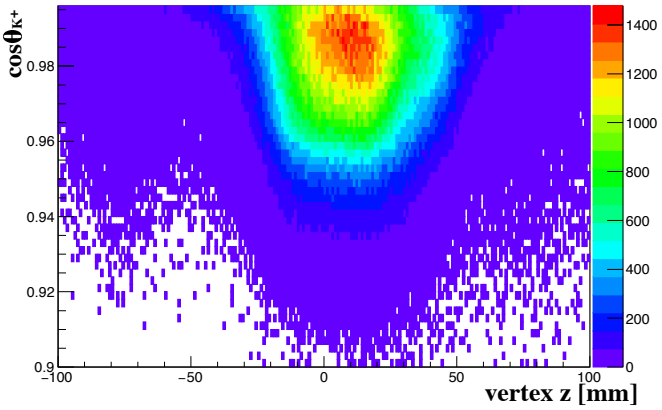

Figure 3.33: Correlation between vertex z and reaction angle θ_{K^+}

Reconstruction of the missing mass

The missing mass (M_X) of the produced particle X via the $p(K^-, K^+)X$ reaction is given as

$$M_X = \sqrt{(E_K^+ + M_p - E_{K^-})^2 - (\overrightarrow{p_{K^-}} - \overrightarrow{p_{K^+}})^2}, \tag{3.11}$$

where $E_{K^+}(E_{K^-})$ and $\overrightarrow{p_{K^+}}(\overrightarrow{p_{K^-}})$ are the energy and momentum of $K^+(K^-)$, and M_p is a proton mass. Actually, K^- reacts with a proton in a nucleus with a fermi motion, but the proton was assumed to be at rest because it cannot be measured in the experiment. The reconstructed missing mass distribution is shown in Fig. 3.34.

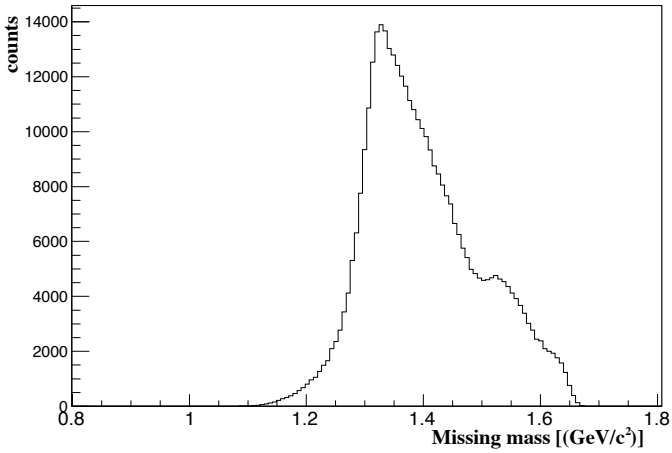

Figure 3.34: The missing mass distribution for the (K^-, K^+) reaction.

3.4 Method 1 in Chapter 1: Analysis and results for Ξ^-Ag and Ξ^-Br atomic X rays

In this section, analysis and results for case1, that is, X rays from Ξ^-Ag atom and Ξ^-Br atom which were generated in the emulsion, are described.

The last orbit of Ξ^-Ag and Ξ^-Br atoms are theoretically expected to be the $7I$ and $6H$ states, respectively. The levels of Ξ^-Ag atom is shown in Fig. 3.35. The energies of the last transitions calculated assuming $t\rho$ potential and the branching ratio of the last transition calculated by A. Gal are listed inTable. 3.4 [22]. The energies for the preceding transition calculated assuming just Coulomb interaction alone and a point charge are also shown. In the experiment, the value of $P_{\Xi(n,l)} \times BR(E1;(n,l) \to (n-1,l-1))$ was obtained from X-ray yield. From the last transition, the $BR(8J \to 7I)$ is evaluated if $P_{\Xi(8J)}$ value is known. Since $BR(9K \to 8J)$ is considered to be $\sim$100%, $P_{\Xi(8J)}$ is evaluated from the preceding transition.

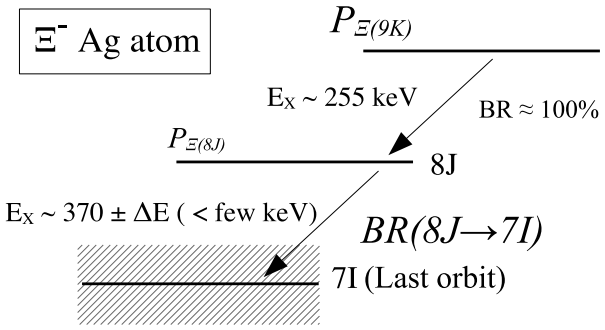

Figure 3.35: The levels of Ξ^-Ag atom.

Table 3.4: The theoretically estimated X-ray energy for the last and the previous transitions. The energies and the branching ratios of the last transitions were calculated using the $t\rho$ potential [22].

	transition	energy [keV]	shift [keV]	width [keV]	branching ratio
Ag	9K→8J	255			
	8J→7I	370	0.28	0.15	0.88
Br	8J→7I	206			
	7I→6H	316	0.73	0.44	0.73

3.4.1 Selection of Ξ^-Ag and Ξ^-Br atom production

For Ξ^-Ag and Ξ^-Br atoms production, the events in which the produced Ξ^- stops in the emulsion were selected with steps as shown below.

1. Selection of the (K^-, K^+) reaction
2. Reconstruction of the Ξ^- track
3. Rejection of Ξ^- passing through the emulsion using SSD2
4. Selection of Ξ^--stop events by emulsion image analysis

Firstly, the Ξ^- production via the (K^-, K^+) reaction was selected by analysis of the magnetic spectrometers (step 1). Then, the Ξ^- track was analyzed by SSD, and the Ξ^- hit position and angle at the surface of the emulsion were predicted. The reaction was reconstructed and selected by the three particles, K^-, K^+ and Ξ^- (step 2). Using hit information of SSD2 located downstream of the emulsion, the Ξ^- passing through the target was rejected (step 3). Then, based on the Ξ^- position on the surface predicted by the Ξ^- track analyzed in step 2, the Ξ^- track was searched for at the developed emulsion (step 4). The reaction analysis by the magnetic spectrometers and the Ξ^- track analysis by SSD make the time for the emulsion image analysis shorter. This is called the counter-emulsion hybrid method. Four levels of Ξ^--stop selections were set by the reaction analysis. The selection (1) was the most strict, and the selected Ξ^--stop events were with good S/N. In order to analyzed the Ξ^--stop events which were missed in the selection (1), the selection (2) was set to be looser. With the selection (2), the number of events to be analyzed in the emulsion is huge, and it will take more time than the selection (1). But the final S/N after emulsion analysis will be the same. More events were selected in the selection (3) with a worse S/N but all Ξ^--stop events are selected. The selection (1) is explained below and all the four conditions are summarized at the end.

Selection of the (K^-, K^+) reaction

For the case1, after applying the selection for the (K^-, K^+) reaction, the Ξ^- track was analyzed by SSD, and the (K^-, K^+)Ξ^- reaction was reconstructed.

The K^+ momentum region of less than 0.9 GeV/c was rejected, in which Ξ^{-*} and $\Xi\pi$ were produced dominantly, in order to reject contamination of Ξ^0. The region of more than 1.5 GeV/c was also rejected because there was a large proton contamination. To select Ξ^- stopped in the emulsion, the K^+ momentum region of $0.9 < p_{K^+} < 1.45$ GeV/c was accepted. In addition, the $\pm 3\sigma$ region of the K^+ peak in the mass square distribution, which depends on the K^+ momentum, was accepted. The correlation of the K^+ mass square and the momentum is shown in Fig. 3.36. The accepted region is shown in black line.

Reconstruction of the Ξ^- track

Here, analysis of the (K^-, K^+)Ξ^- reaction to select the events in which Ξ^- stopped in the emulsion is described. The Ξ^- track was reconstructed by using hit information of SSD1. When there were hits in all the four layers, at least one hit in each layer except for the hit by the scattered K^+ was

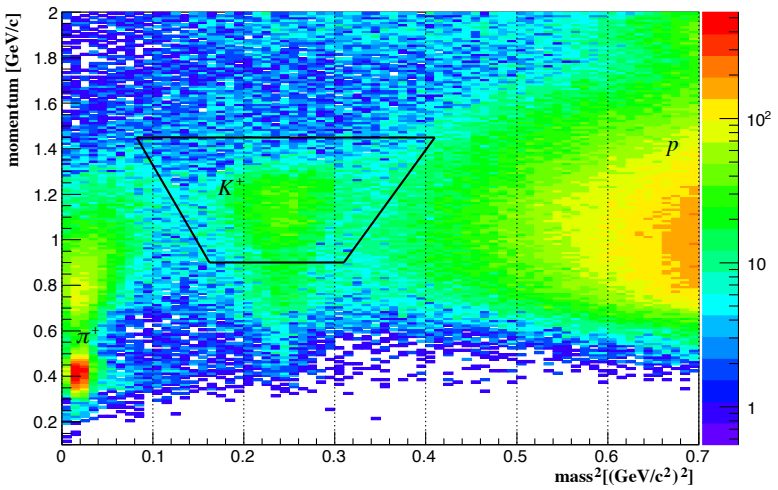

Figure 3.36: Correlation between the mass square and the momentum of scattered particles. The region surrounded by the black line is accepted as the scattered K^+.

required for the Ξ^- track reconstruction. When there were multi-hit planes, multi candidate tracks were obtained using all the combinations. The reaction point is reconstructed using tracks of K^-, K^+ and Ξ^-. Firstly, the vertex point was determined by two tracks, namely Ξ^- and K^+ tracks. The distributions of reconstructed vertex point are shown in Fig. 3.37. The accepted region was set to $-28 < x < 28$ [mm], $-20 < y < 20$ [mm] and $-20 < z < 20$ [mm].

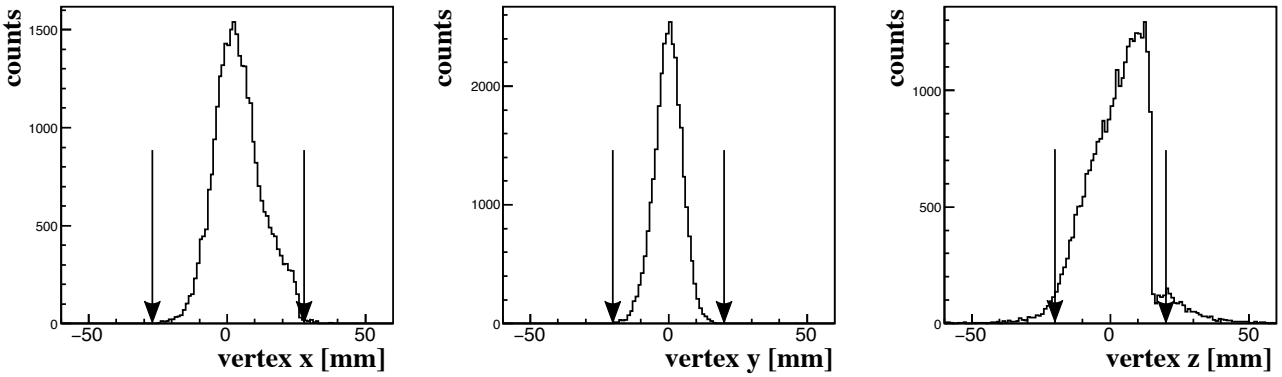

Figure 3.37: The vertex point distributions reconstructed by the K^+ and Ξ^-tracks.

Residue of vertex point

Consistency between the x and y positions of K^- at the target and the vertex point reconstructed by K^+ and Ξ^- tracks was checked. The residue is shown in Fig. 3.38. Events in the $\pm 2\sigma$ region of

the residual peaks were accepted since they were considered to have three tracks consistent with the $(K^-, K^+)\Xi^-$ reaction.

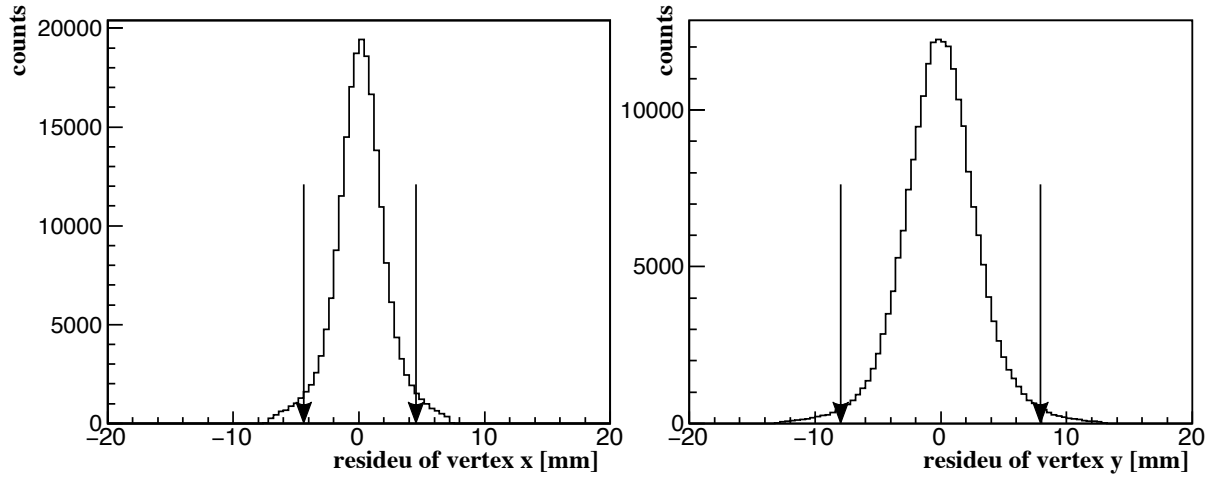

Figure 3.38: Residue of the vertex point.

Residue of angle for Ξ^- track

The track of Ξ^- was obtained from the analysis of SSD. On the other hand, from the missing momentum of Ξ^- reconstructed by the (K^-, K^+) reaction analysis, the angle of the Ξ^- track when it is incident on SSD1 was predicted. Consistency between the reconstructed Ξ^- emission angle and the direction of the missing momentum $(\overrightarrow{p_{\Xi^-}})$ was checked. The residues of the angles in x and y directions are obtained as shown in Fig.3.39, and events in the $\pm 6\sigma$ regions of the peaks were accepted.

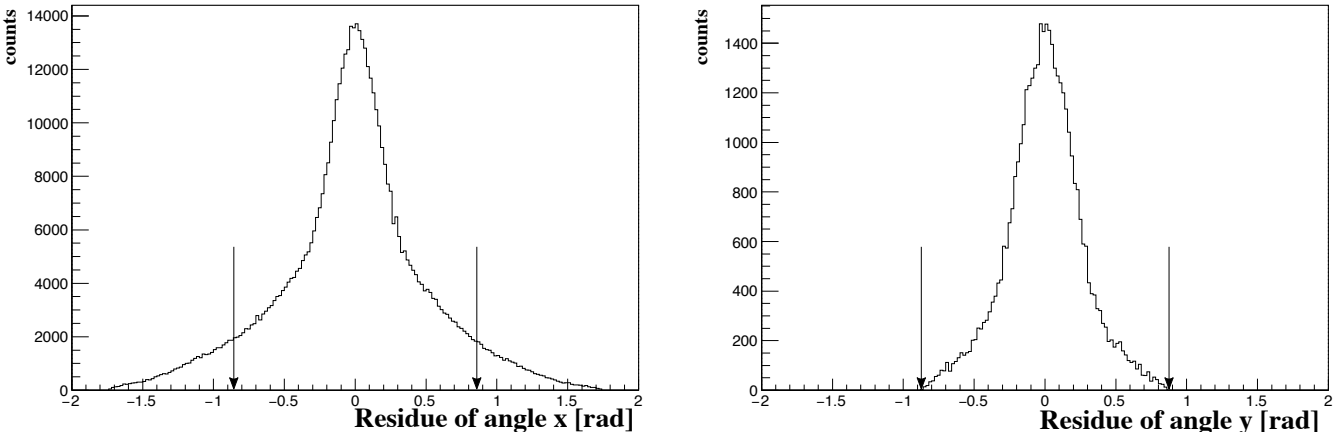

Figure 3.39: Residue of the angle of Ξ^-.

Rejection of Ξ^- passing through the emulsion using SSD2

To reject events in which Ξ^- particles passed through the emulsion module, SSD2 located downstream was used as a veto detector. A hit position was predicted from the track reconstructed by SSD1. When there was a hit excluding K^+ hit within 3 mm from the predicted position, this was regarded as a hit by the Ξ^- particle and the event was rejected.

Summary of selections in reaction analysis

The above selection conditions are summarized as selection (1) in Table 3.5. Selection (1) was applied in the present analysis described in this thesis. The number of candidates for Ξ^- stop was 8×10^3. Using Geant4 simulation [40], 80% of all Ξ^--stop events are estimated to be selected by the selection (1).

As shown in Table 3.5, some other selection conditions with wider regions were also considered. Selection (2) and (3) contain 94% and 100 % of the Ξ^--stop events, respectively. Selection(4) contains all the Ξ^- production events. Analysis will be completed when the selection (3) is applied, and the longest time is required to analyze the emulsion images due to lots of candidate events. Thus, these events selected by selection (1) for which emulsion image analysis was finished are discussed in this thesis.

Table 3.5: Summery of the selection conditions

	selection			
	(1)	(2)	(3)	(4)
χ^2 KURMA	30	10000	10000	10000
K^+ mass^2	$\pm3\sigma$	$\pm5\sigma$	$\pm5\sigma$	$\pm5\sigma$
vertex residual	$\pm3\sigma$	$\pm5\sigma$	$\pm5\sigma$	$\pm5\sigma$
angle residual	$\pm6\sigma$	$\pm12\sigma$	$\pm12\sigma$	$\pm12\sigma$
SSD2	no Ξ^- hit	no Ξ^- hit	no Ξ^- hit	
SSD1 dE	>60000	>40000	>30000	
track / mod	440	850	6200	16000
Ξ^-stop	80 %	94 %	100 %	100 %

Selection of Ξ^--stop events by emulsion image analysis

Based on the predicted position from the SSD analysis, the candidates of Ξ^- tracks were searched for in the first layer of the emulsion sheets by an optical microscope. Then, the tracks of the candidate particles were traced until they stop. Just before the particle stops in the emulsion, a thick track is observed because of a large energy deposit. In addition, the track gets dizzy due to a

multiple Coulomb scattering. When these two features were observed at the stop point of a track, the event was considered as a "stop-event". After Ξ^- stopped in the emulsion, it is captured by an atom, and at the end, it is absorbed in the nucleus as $\Xi^- p \rightarrow \Lambda\Lambda$ and the nucleus is break up to fragments. Sometimes a double-Λ hypernucleus, or one or two single-Λ hypernuclei are produced as fragments, sometimes the produced Λs not bound to a nucleus and mesonic decay as $\Lambda \rightarrow p\pi^-$ or $\Lambda \rightarrow n\pi^0$. Then, Λ inside a nucleus decays as $\Lambda p \rightarrow pn$ or $\Lambda n \rightarrow nn$. The stop events were classified into two types according to their visible structure at the stop point.

1. "σ-stop" event
   If one or more charged fragments are produced, one or more charged tracks are observed at the stopping point as shown in Fig. 3.40. Such an event is called a "σ-stop" event. The arrow represents a Ξ^- track with "dizziness". Then, for the case of Fig. 3.40, three charged tracks are seen from the Ξ^- stop point.

2. "ρ-stop" event
   In this case, no charged particle track is observed except for an Auger electron at the stop point as shown in Fig. 3.41. If only neutral particles, n, Λ, and π^0 are produced as fragment, there is no tracks at the stopping point. Or, if heavy fragment is produced, the track was too short to be observed. Such an event is called a "ρ-stop" event.

If Ξ^- is absorbed in the nucleus and form hypernuclei, it is observed as a σ- or ρ-stop event.

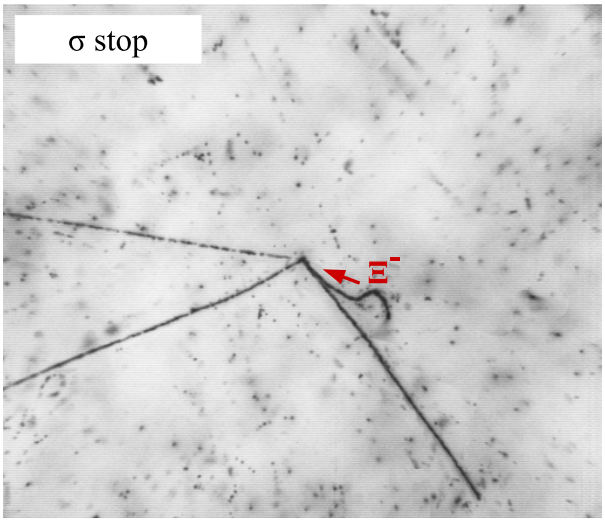

Figure 3.40: An example of the Ξ^- "σ-stop" event. A Ξ^- was observed as a dizzy track and there were three charged tracks from the Ξ^--stop point.

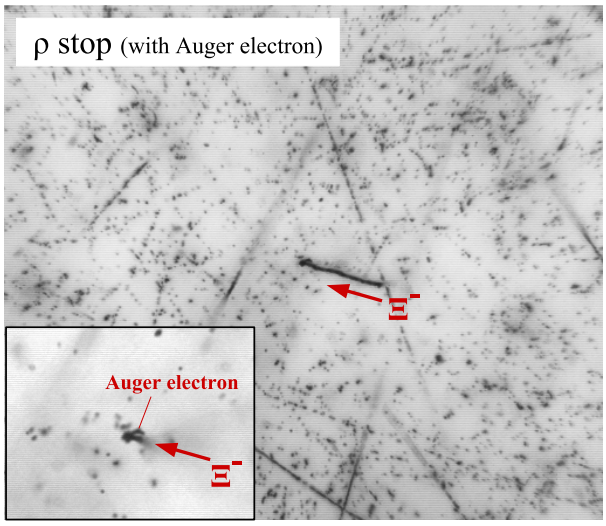

Figure 3.41: An example of the Ξ^- "ρ-stop" event. An expanded picture of the stop point is shown in the lower left. An Auger electron was observed from the stop point.

At present, the image analysis for 67 emulsion modules has been completed with the selection (1). The number of confirmed "σ-stop" and "ρ-stop" events are 1319 and 6317, respectively. The number of the σ-stop events corresponds to 20% of the estimated total σ-stop events. For Ξ^- stop events, the ratio of the σ-stop and ρ-stop events is $\sim$2:1 [7]. Many of the ρ-stop events are not Ξ^- but backgrounds such as protons. The ρ-stop events are further classified based on absence or presence of an Auger electron. By selecting "ρ-stop with an Auger electron" events, contamination of the proton ρ-stop events can be rejected. When there were three or more grains within 3 μm from the Ξ^--stop point, it is regarded as a track of an Auger electron. For the Ξ^- ρ-stop, the probability of the Auger electron emission is about 50% [7]. At present, for the 44 emulsion modules, 37 "ρ-stop with Auger electron emission" events were found.

The number of σ-stop events

When the Ξ^- atomic X-ray yield is discussed, the number of captured Ξ^-s ($N_{\Xi capture}$) is needed. Thus, as a systematic error for $N_{\Xi capture}$, the effect of the human error is evaluated. The human error means the probability that the observer of emulsion image makes misjudgment in the event classification. Five people (A, B, C, D, and E) analyzed the same event set as cross-check. When the result analyzed by A disagrees with the majority of the others, it was regarded as the error by A. The number of σ-stop events analyzed by each observer and his/her error is listed in Table 3.6. The weighted average of the error is 13.8%. For 1319 event, the error was 154 events. In addition, the amount of contamination of non Ξ^--stop events, that is, π^- σ-stop events, is estimated to be 3% [41]. Considering both of the human error and the π^- contamination, the number of observed Ξ^- σ-stop events was 1279_{-149}.

Table 3.6: The number of analyzed σ-stop events by each observer.

person	σ-stop events[event]	Error [%]	Error [event]
A	223	6	13.4
B	12	20	2.4
C	220	24	52.8
D	286	11	31.5
E	448	8	35.8
F	79	no data	10.9
G	46	no data	6.3
H	3	no data	0.4
I	2	no data	0.3
	total	average	total
	1319	13.8	153.8

The following results in this thesis are based on Ξ^--stop events obtained from analysis of 67

emulsion modules (see Section. 3.4.1). The number of classified events and that of coincidence events with Hyperball-X are listed in Table. 3.7. The error for the ρ-stop events, including Auger emission, was not evaluated. It is not used in the following discussion in this thesis.

Table 3.7: The number of classified events.

	HBX coin [events]	Total [events]	error [%]
σ-stop of Ξ^-	457	1279	$\pm$12
ρ-stop	1685	5822	-
ρ-stop with Auger emission	37	Not analyzed	-

The stopped Ξ^- particle is captured by light nuclei such as C, N and O, or by heavy nuclei such as Ag and Br in the emulsion. According to the previous experiment (KEK E176[7]), the capture probability of Ξ^- by light and heavy nuclei is $42.3^{+4.5}_{-9.6}$% and $57.7^{+6.1}_{-9.6}$%, respectively. The same situation is assumed in this experiment. The ratio of the capture probabilities by Ag and Br can be assumed to be proportional to the atomic number Z. In the current analysis, the expected yields of Ξ^-Ag atom and Ξ^-Br atom with the $\sigma-$stop selection are 421 ± 63 counts and 317 ± 48 counts, respectively, as summarized in Table 3.8. The X-ray yield of the Ag($8J \to 7I$) transition detected by Hyperball-X is estimated as

$$yield = N_{\Xi capture} \times P_{\Xi(8J)} \times BR(8J \to 7I) \times \epsilon_{HBX} \times \epsilon_{BGO} \tag{3.12}$$

where ϵ_{BGO} is the survival ratio of the BGO detector. Assuming that $P_{\Xi(n,l)}$ is 0.6, the yield of 370-keV X ray is estimated to be $421 \times 0.6 \times 0.88 \times 0.0083 \times 0.84 = 1.55$ counts at present analysis.

Table 3.8: Summary of Ξ^- atom yield.

		event	ratio[%]	error [%]
	$\Xi^-\sigma$-stop	1279		12
	Light Ξ^- atom	541	42.3	9.6
	Heavy Ξ^- atom	738	57.7	9.6
	Ag		57	
	Br		43	
total	Ξ^-Ag atom	421		15
	Ξ^-Br atom	317		15

3.4.2 X rays from Ξ^-Ag and Ξ^-Br atom

The X-ray spectra for (a) σ-stop, (b) ρ-stop with an Auger emission, (c) σ- and ρ-stop with an Auger and (d) all the selection (1) events are shown in Fig. 3.42. The spectra with and without the BGO suppression with the 50-ns gate are shown in red and black, respectively.

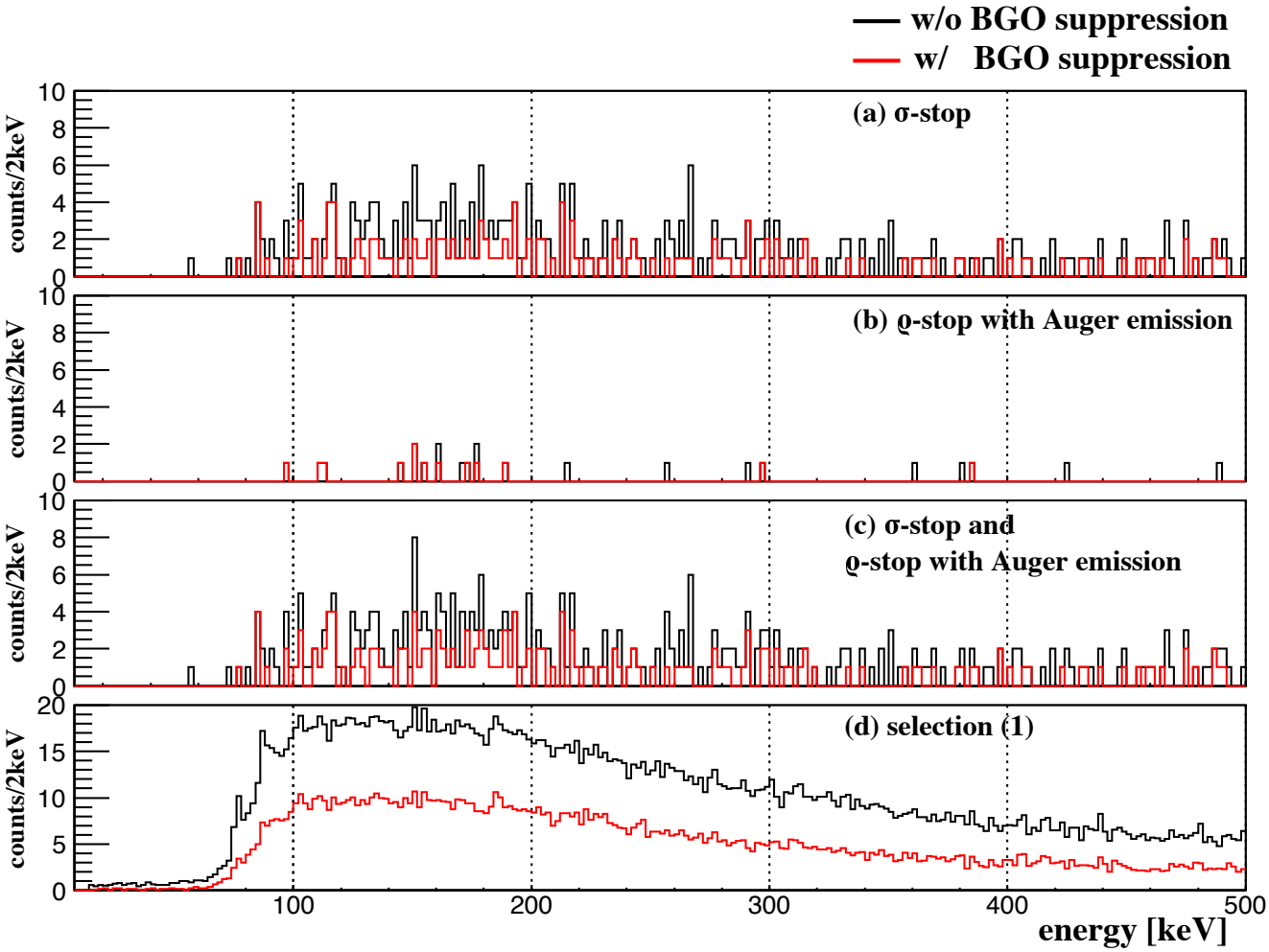

Figure 3.42: X-ray spectra in coincidence with emulsion image analysis. (a) is a spectrum for the σ-stop events, (b) is for the ρ-stop events with an Auger emission, (c) is for the σ- and ρ-stop with the Auger events and (d) is for all the events of selection (1). The spectra with and without the BGO suppression are shown in red and black, respectively.

Search for X-ray peaks

X-ray peaks were searched for in the region from 100 to 500 keV which includes the theoretically expected energies. Using the likelihood method, the spectrum (c) for the σ-stop events with the

BGO suppression was fitted by a Gaussian plus a background function,

$$\mu(x) = AMP \exp\left(-\frac{(x - mean)^2}{2\sigma_{Gauss}}\right) + C \tag{3.13}$$

where x is X-ray energy, AMP, mean and σ_{Gauss} are the amplitude, mean and sigma value of the Gaussian function, and C is a constant background. Assuming the X-ray counts follow a Poisson distribution, the L value is given as

$$L = \prod_i \frac{\mu_i^{y_i} e^{-\mu_i}}{y_i!} \tag{3.14}$$

where y_i is X-ray counts at x_i (i-th bin). σ_{Gauss} was fixed to the resolution of 0.8 keV and AMP was constrained to be 0 or more. As shown in Fig. 3.43, for example, the mean value was fixed to E_{mean}, and a fit range ($2\Delta E_{range}$) was 40 keV. The AMP and C values were obtained to maximize the $logL$. The peak significance is defined as follows using AMP and its fitting error, AMP_{error},

$$\text{peak significance} = \text{AMP}/\text{AMP}_{\text{error}}.$$

The mean value (E_{mean}) was changed from 100 to 500 keV with 1-keV step.

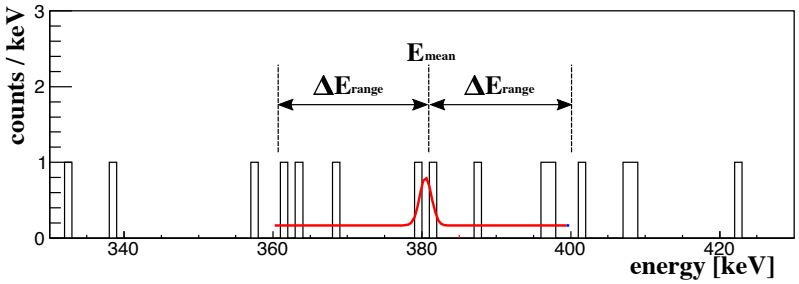

Figure 3.43: An example of the peak fitting at Ξ^-Ag atomic X-ray spectrum. The spectrum was fitted by a Gaussian plus a constant function. E_{mean} and ΔE_{range} represent the mean value of the gaussian function and the fitting range, respectively.

The evaluated peak significance as a function of E_{mean} was plotted in Fig. 3.44. No evident peak with 3 sigma significance was found.

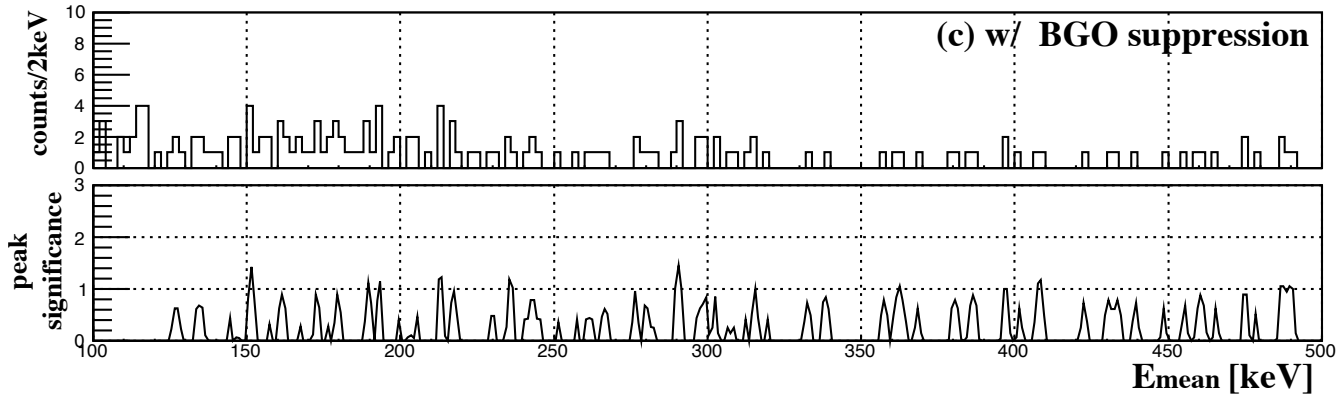

Figure 3.44: The obtained peak significance. The top is the spectrum (c) for σ-stop and ρ-stop with an Auger electron, and the bottom shows the evaluated peak significance.

X-ray spectrum for high energy region (500 keV $< E_{mean}$)

The spectrum of the energy region over 500 keV under the condition of σ-stop and ρ-stop with an Auger electron is shown in Fig. 3.45. The BGO suppression was applied. Although statistics is low, it seems that there is a peak structure around 661 keV. According to the National Nuclear Data Center[2], none of the nuclei contained in the material around the detector emits the corresponding γ ray. It should be explained whether it is statistical fluctuation or some signal when statistics is increased in future analysis.

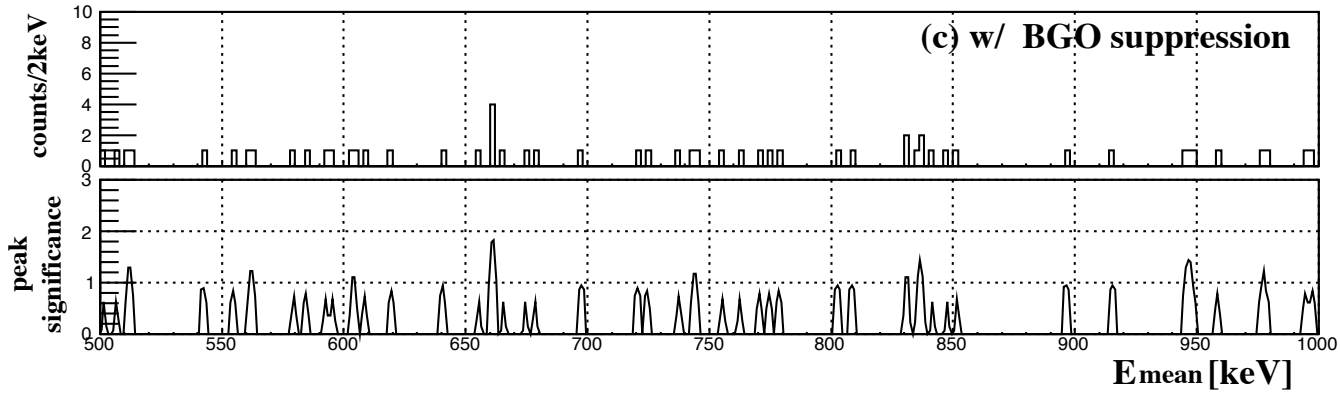

Figure 3.45: The X-ray spectrum (c) of the over 500 keV region for σ-stop and ρ-stop with an Auger electron is shown at top, and the peak significance was obtained as shown at bottom.

X rays from Ξ^-Ag atom

The expanded spectrum with the BGO suppression around 370 keV, which corresponds to the X-ray energy of the last transition of the Ξ^-Ag atom, was obtained as shown in top of Fig. 3.46.

[2]Nuclear physics data base. All the known nuclear levels and γ-ray energies are compiled [42].

Assuming that the signal was small enough, the spectrum (a) was fitted with a constant. From the fitting result, the background level was obtained to be $0.17^{+0.57}_{-0.10}$ counts/keV in this region as overlayed in a black line in the spectrum (a). Note that Poisson distribution was assumed for evaluation of the statistical errors 68% confidence level.

Since there was no evident peak as mentioned above, the upper limit of the X-ray yield was evaluated. The X-ray yield (N_{Xrays}) and the number of Ξ^- stopped and captured by atom ($N_{\Xi capture}$) were experimentally obtained and ϵ_{HBX} was evaluated. From these, the following value is given,

$$BR(E1,(n,l) \to (n-1,l-1)) \times P_{\Xi^-(n,l)} = \frac{N_{Xrays}}{N_{\Xi capture} \times \epsilon_{HBX}} \tag{3.15}$$

where $BR(E1,(n,l) \to (n-1,l-1))$ is branching ratio of $E1$ transition and P_{Ξ^-} is the ratio of the number of Ξ^-s which reach the (n,l) orbit to the total number of Ξ^-s captured in the atom. In the present analysis, the value of $N_{\Xi capture}$ was obtained only with the condition of the σ-stop selection. Thus, assuming that X-ray peak was observed, the spectrum (a) was fitted with a Gaussian function plus a constant. For the Ag$(8J \to 7I)$ transition, this value was evaluated using the number of $\Xi^-\sigma$-stop events and the efficiency taking the lower value of their errors as shown in bottom of Fig. 3.46. The central value is plotted by cross, and the error comes from that of X-ray yield (68%). The axis converted to $BR(8J \to 7I)$ assuming that $P_{\Xi(8J)}$ is ~ 0.6 [23] is also shown on the right side of the figure as a reference. The upper limit of $P_{\Xi(8J)} \times BR(8J \to 7I)$ is found to be over 1 in the region of energy shift less than 10 keV due to poor statistic.

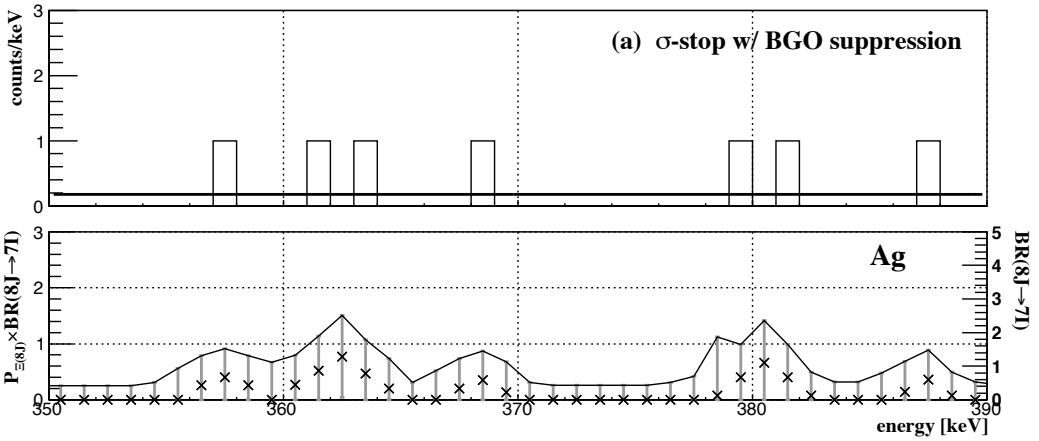

Figure 3.46: The expanded X-ray spectrum for the $(8J \to 7I)$ transition of Ξ^-Ag atom shown in top. The X-ray energy is 370 keV without the strong interaction. The constant background obtained by fitting is shown in solid line. The upper limit of $P_{\Xi(8J)} \times BR(8J \to 7I)$ with error of 68% confidence level was obtained as shown at bottom.

For the preceding transition Ag$(9K \to 8J)$, the expanded spectrum around the expected energy, 255 keV, is shown in top of Fig. 3.47. The background level was obtained to be 0.32 counts/keV in this region as overlayed in a black line in the spectrum (a). The evaluated $P_{\Xi^-(9K)} \times BR(9K \to$

$8J$) is also shown in bottom, and this can be considered to be nearly equal to $P_{\Xi^-(9K)}$ because $BR(9K \to 8J)$ shold be ∼100%.

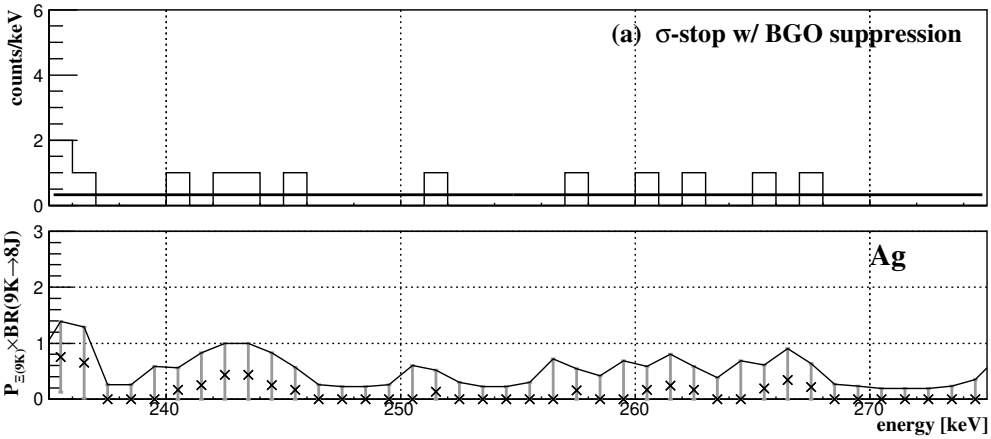

Figure 3.47: The expanded X-ray spectrum around the expected energy, 255 keV, of the $(9K \to 8J)$ transition of Ξ^-Ag atom shown in top. The upper limit of $P_{\Xi(9K)} \times BR(9K \to 8J)$ with the error of 68% confidence level was obtained as shown in bottom.

X rays from Ξ^-Br atom

For the last and the preceding transitions of Ξ^-Br atom, the X-ray spectra around the energy for $(7I \to 6H)$, 316 keV, and for $(6H \to 7I)$, 206 keV without the strong interaction.

The expanded spectrum with the BGO suppression around 316 keV was obtained as shown in top of Fig. 3.48. The background level was obtained to be 0.30 counts/keV in this region as overlayed in a black line in the spectrum (a). The upper limit of $P_{\Xi(7I)} \times BR(7I \to 6H)$ with error of 68% confidence level was obtained as shown in bottom.

For the preceding transition Br$(8J \to 7I)$, the expanded spectrum around the expected energy, 206 keV, is shown in top of Fig. 3.49. The background level was obtained to be 0.76 counts/keV in this region as overlayed in a black line in the spectrum (a).

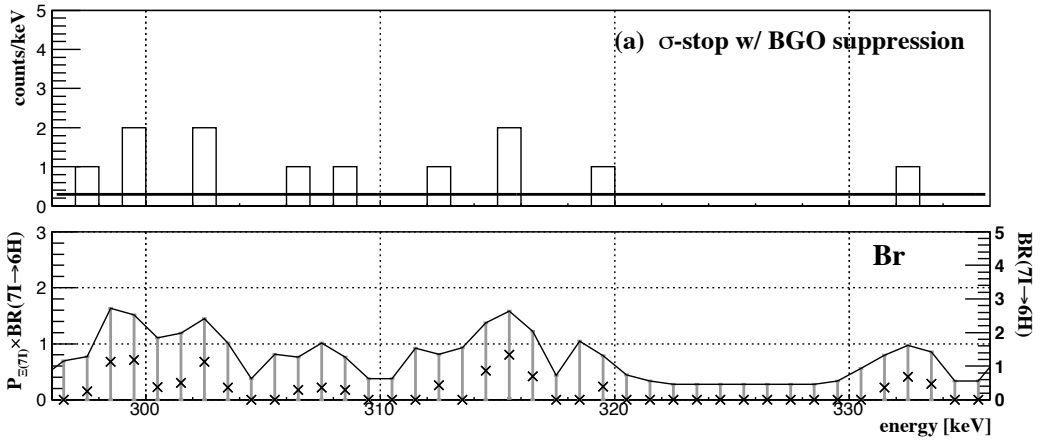

Figure 3.48: The expanded X-ray spectrum for the $(7I \to 6H)$) transition of Ξ^-Br atom shown in top. The X-ray energy is 316 keV without the strong interaction. The background constant obtained by the fitting is shown in solid line. The upper limit of $P_{\Xi(7I)} \times BR(7I \to 6H)$) with the error of 68% confidence level was obtained as shown in bottom.

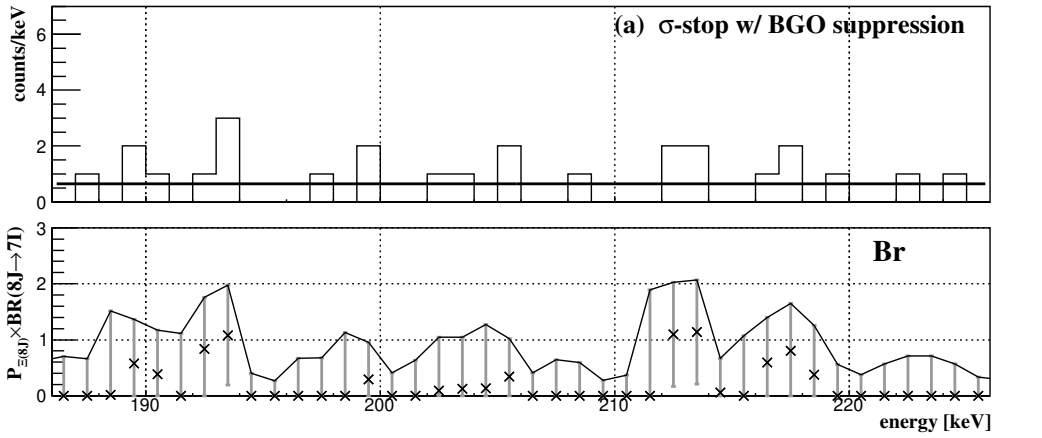

Figure 3.49: The expanded X-ray spectrum around the expected energy, 206 keV, of the $(8J \to 7I)$ transition of Ξ^-Br atom shown in top. The upper limit of $P_{\Xi(8J)} \times BR(8J \to 7I)$ with the error of 68% confidence level was obtained as shown in bottom.

3.5 Method 2 in Chapter 1: Analysis and results for Ξ^-C atom

In this section, the analysis and result for X rays from Ξ^-C atom is described. When the produced Ξ^- was stopped in the diamond target, a Ξ^-C atom was formed and X rays were emitted. The energies of Ξ^--C bound states are theoretically calculated considering only Coulomb potential as shown in Table 3.9. For the light nuclei such as C, N and O, the $3D$ orbit is considered as the last orbit, that is, most of Ξ^-s are absorbed by the ^{12}C nucleus from the $3D$ orbit [23]. The Ge detector had no sensitivity for X rays less than 100 keV because the experiment was designed to measure X rays of 300 - 400 keV. The X-ray energy of the last transition $^{12}\mathrm{C}(4F \rightarrow 3D)$ is $55 + \Delta E$ keV, and this is out of the sensitive energy region of the Ge detector. However, the X-ray energy of the $(3D \rightarrow 2P)$ transition with the Coulomb interaction alone is 154 keV, and this is in the sensitive region. According to A. Gal [23], a few % of Ξ^-s are not absorbed from the $3D$ state. When the Ehime potential as shown in Fig. 3.50 is employed as the ΞN potential, for example, the energy shift of the $(3D \rightarrow 2P)$ transition is calculated to be 454 keV [21]. Analysis and results on X rays of the $(3D \rightarrow 2P)$ transition is described in this section.

Table 3.9: The energies of the Ξ^--C bound system with only Coulomb interaction.

state	energy [MeV]
1S	0.940
2P	0.283
3D	0.126
4F	0.070
5G	0.045

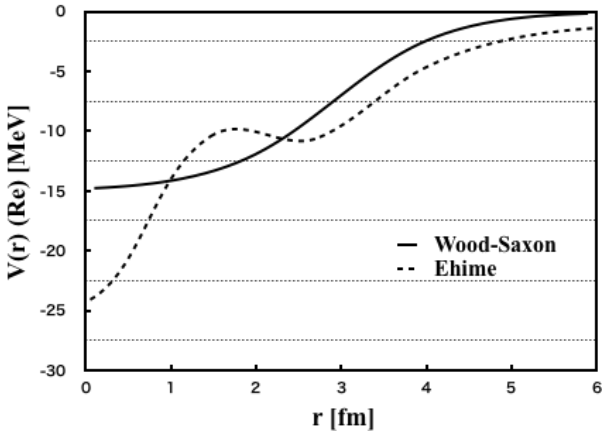

Figure 3.50: The Ehime [21] and the Woods-Saxon type potentials to describe the Ξ-nucleus interaction.

3.5.1 Selection of Ξ^-C atom production

Since the experiment was not optimized to detect Ξ^-C atomic X rays, most of Ξ^-s were not stopped inside the target, and the stopped Ξ^- was not directly identified by dedicated detectors. The events in which the produced Ξ^-s were likely to stop inside the target were extracted using information of existing detectors following the procedure below, and the X-ray spectrum of Ξ^-C atom was obtained.

1. Selection of the (K^-, K^+) reaction
2. Rejection of Ξ^- passing through the target using SSD1
3. Selection of a vertex point
4. Select Ξ^- with a large stopping probability in the target
5. Reconstruct the missing mass

Firstly, the Ξ^- production was selected by analysis of the magnetic spectrometers (step 1). Then, the Ξ^- which was produced in the target and had a large probability to stop inside the target was selected (step 2, 3, 4). SSD1 located downstream of the target was used as a veto detector for a Ξ^- passing through the target. Using the vertex point, Ξ^-s produced in SSD1 and the emulsion were rejected. Since the Ξ^- produced with a low momentum was likely to stop, its behavior in the target was simulated, and the Ξ^- with a large stop probability was selected. Then, to select the Ξ^-s produced via the $K^-p \to K^+\Xi^-$ reaction, the missing mass was reconstructed and the Ξ^--peak region was selected (step 5).

Selection of the (K^-, K^+) reaction

K^- and K^+ were analyzed as described in Section 3.3, and they were selected with the conditions explained as follows.

K^- was identified by the time-of-flight between BH1 and BH2 shown in Fig. 3.51. The distributions taken by the KK trigger are shown and there was no π^+ peak. Thus, the lower end of the gate was set to 0.6 ns, that is, 5σ from the mean of the K^- peak. The higher end of the gate was set to 4 ns because there is no contamination in the region. The region of 0.6 < time-of-flight < 4 ns was accepted.

The scattered K^+ was selected by a calculated mass square. The mass square distributions are obtained depending on their momentum as shown in Fig. 3.52. The mass resolution was worse in the high momentum region. Since the mass resolution depends on momentum, the K^+ selected region was set for each momentum region. The K^+ peak was fitted by a Gaussian plus a quadratic function, and the $\pm 3\sigma$ region of the K^+ peak, which are shaded regions in Fig. 3.52, was accepted. As seen in the lowest distribution of Fig. 3.52, K^+ with a momentum over 1.4 GeV/c was not

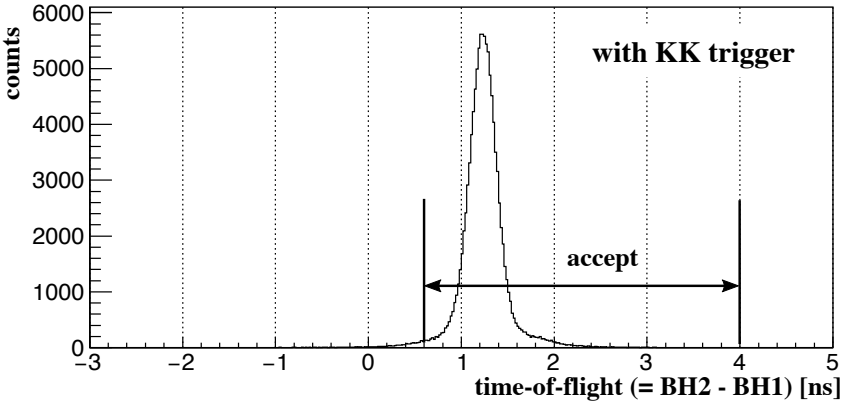

Figure 3.51: Selection of the time-of-flight between BH1 and BH2.

produced, which shows that the threshold of the (K^-, K^+) process was around 1.4 GeV/c. The K^+ of the momentum less than the threshold, namely $0 < p_{sca} < 1.4$ GeV/c, was selected since the processes in which a Ξ^- was produced, e.i., the process (a) and (c) (cf. pp65), were accepted. Since in the process (b), Ξ^{-*} is produced and it partly decays to Ξ^- , the process (b) was also accepted.

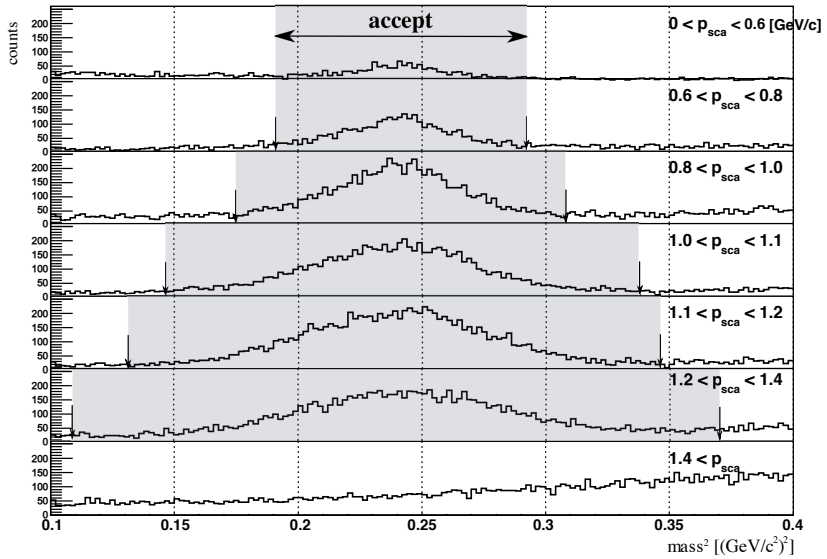

Figure 3.52: The mass square distribution of the scattered particle for various p_{sca} (momentum of the scattered particle). K^+ peak is fitted by a gaussian plus a quadratic function. The $\pm 3\sigma$ region of the K^+ peak shown in the figure was accepted as K^+.

Rejection of Ξ^- passing through the target using SSD1

The Ξ^-s which did not stop in the target and hit SSD1 were rejected. As sketched in the Fig. 3.53, they were classified into two cases,

(1) Ξ^-s reached the emulsion module,

(2) Ξ^-s stopped in a layer of SSD1.

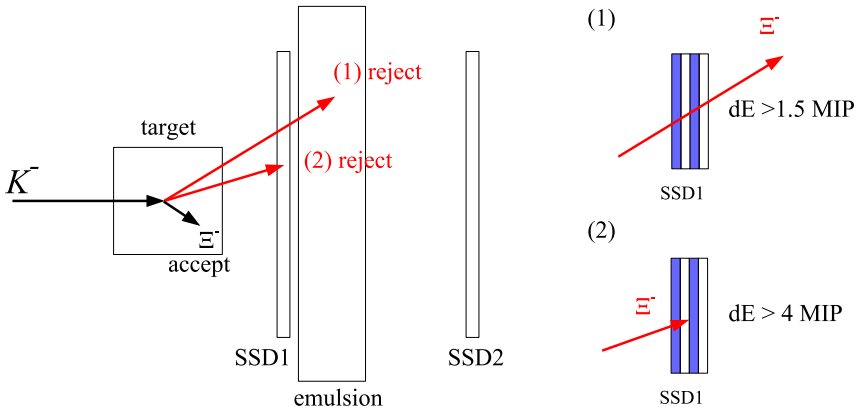

Figure 3.53: Examples of the SSD1 rejection. The Ξ^-s reached at the emulsion (1) and stopped in SSD1 (2) were rejected.

The hit at SSD1 was analyzed using an energy deposit value (dE). The signal wave form was acquired in SSD, and its integrated value corresponds to dE. The dE distribution at SSD is shown in Fig 3.54, especially for the cases with a low missing momentum (p_Ξ). Each distribution is scaled for comparison. The horizontal axis indicates dE in SSD1, and dE value of 1×10^4 corresponds to MIP (minimum ionizing particle energy). Note that the data for the scattered K^+ is excluded in this distribution. The correlation of the missing momentum and the energy deposit at the most upstream layer of SSD1 is shown in Fig. 3.55. In the case (1), when a dE value was larger than 1.5 MIP, it was regarded as a hit. For the Ξ^- with high momentum passing through SSD1, its track was reconstructed successfully using the hit information of all the four layers of SSD1. In the case (2), when the Ξ^- with a low momentum, Ξ^- slows down sufficiently but not stops in the target, they can be identified by a large energy deposit value. In Fig 3.55, the dE distribution of the case of the $0.7 < p_\Xi < 0.8$ GeV/c is shown in blue. There are relatively many events with dE more than 3×10^4. This structure is due to the Ξ^- just before stopping. The lower momentum at production gives the larger dE at SSD1. Indeed, this tendency is seen in the dE distribution of low momentum ($p_\Xi < 0.7$ GeV/c), shown in red and black. For the case of $0 < p_\Xi < 0.6$ GeV/c, shown in black, the structure from Ξ^- is seen in the region where dE is more than 4×10^4. Therefore, the threshold of dE was set to 4×10^4. When any layer of SSD1 has a signal of dE more than this

threshold, that event was rejected. The Ξ^-s that fit to these cases were rejected, and this is called the SSD1 rejection in this thesis.

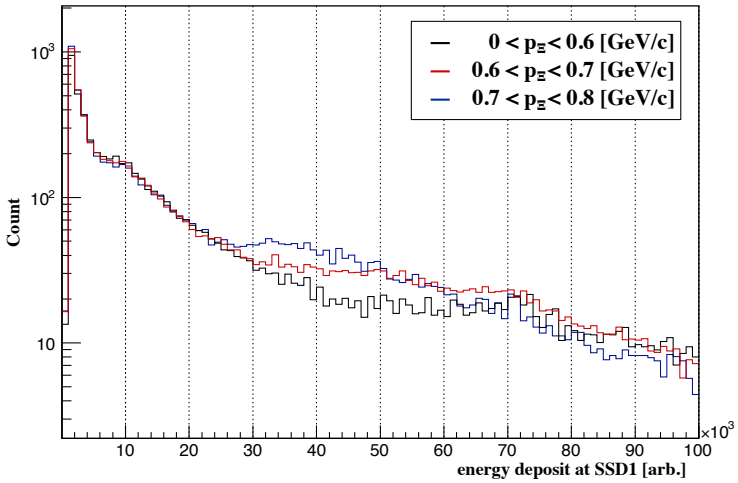

Figure 3.54: The energy deposit at SSD1 for the various missing momentum.

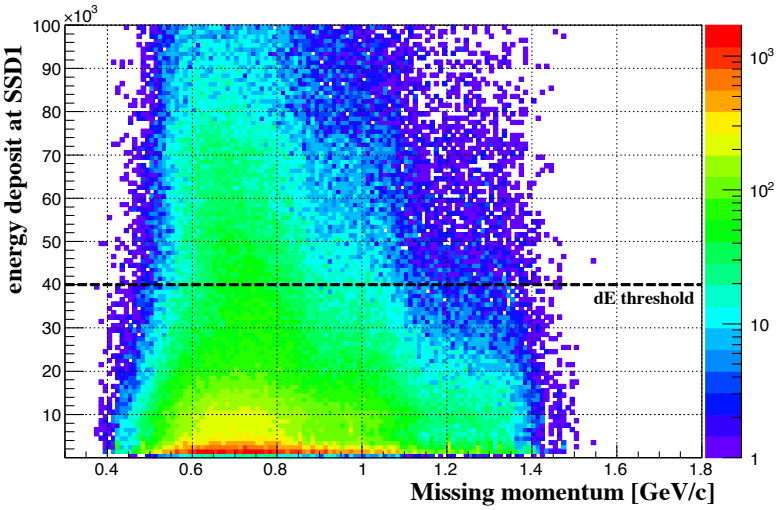

Figure 3.55: Correlation of the missing momentum and the energy deposit at SSD1.

Selection of vertex point

The K^- reacted in the target, SSD1 or the emulsion. To select Ξ^- produced in the target, the vertex z point was reconstructed from the K^- and K^+ tracks. When the SSD1 rejection was applied, the vertex z distribution is obtained as shown in blue in Fig. 3.56. As described in Section 3.3.3, when

the events with the residue in SSD1 less than 0.1 mm were selected, the distribution for the target reaction events was obtained. The obtained distribution was scaled and shown in red in the figure. The total data (black) was fitted by the scaled distribution (red) plus constant in the region of $-50 < z < -20$ mm. The scale factor and the constant value were optimized so that the difference between two distributions in that region was minimum. As a result, the difference between the total data (black) and the fitted distribution for the target (red) was obtained as shown in blue. The fitted distribution for the target was regarded as a signal, and the lower end of the selected region was set to -50 mm. The upper end was set to achieve the best significance ($S/\sqrt{N}$) that was 0 mm.

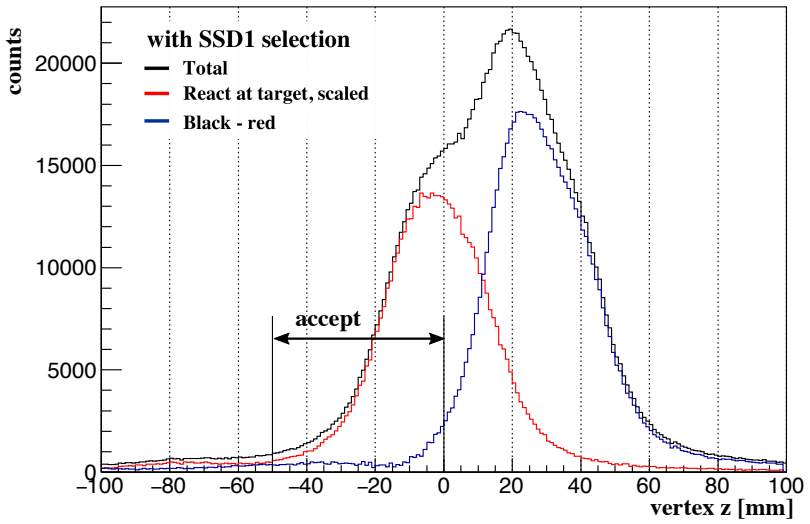

Figure 3.56: The vertex point in z direction with the SSD1 rejection (black). The scaled distributions in the case of Ξ^- produced in the target and in SSD or the emulsion are shown in red and blue, respectively.

Select Ξ^- with a large stopping probability in the target

The probability that the produced Ξ^- particle stopped inside the target was estimated for each event using Geant4 simulation. The missing momentum of the produced particle (X) is given as

$$\overrightarrow{p_X} = \overrightarrow{p_{K^-}} + \overrightarrow{p_p} - \overrightarrow{p_{K^+}}. \tag{3.16}$$

The fermi motion of a proton in the nucleus ($\overrightarrow{p_p}$) which reacted with the K^-should be taken into account. The momentum distribution of a proton in a ^{12}C nuclear was assumed as the same as to that assumed in the JAM code as shown in Fig. 3.57[3]. Because of the vertex resolution and the fermi motion of a proton, both of the z position of the vertex and the missing momentum had uncertainties. Therefore, motion of the produced particle in the target was simulated 100 times under different assumptions of the generated point and the momentum. In the simulation, all the

[3]JAM is a program to simulate relativistic nuclear collisions [39]. In the program, the Fermi motion of nucleons is assigned according to the local fermi momentum which depends on the nuclear density distribution.

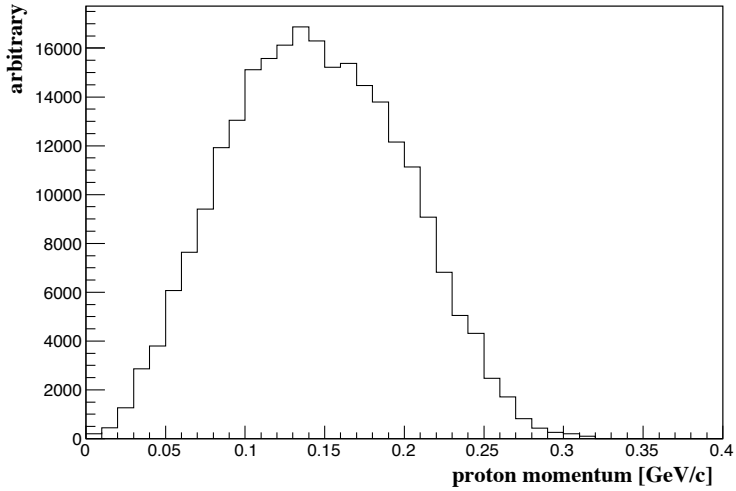

Figure 3.57: The momentum distribution of a proton in a ^{12}C nucleus.

produced particles were assumed to be Ξ^- particles, and their decay in flight was considered. As a result, "the stop probability" that the Ξ^- stops inside the target is obtained as shown in Fig. 3.58. As is seen in the correlation between the stop probability and the missing momentum shown in Fig 3.59, a Ξ^- with the lower momentum less than 0.7 GeV/c has the higher stop probability.

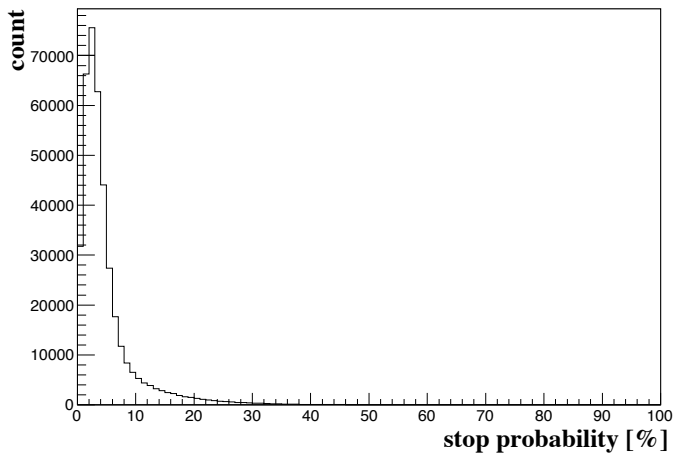

Figure 3.58: The stop probability of Ξ^-particles.

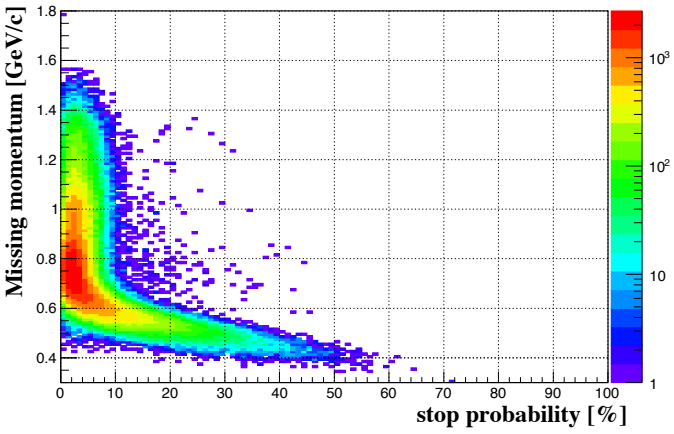

Figure 3.59: Correlation between the stop probability and the missing momentum of Ξ^-.

To select events in which a Ξ^- stopped in the target with a high probability, the threshold of the stop probability was set. When a Ξ^- stops inside the target, the event is regarded as signal (S) because it is possible to emit X rays from a Ξ^- atom. Otherwise, it is assumed to be a noise

(N) because of possible γ-ray or neutron emission as follow,

$$\begin{aligned} \Xi^- &\rightarrow \Lambda + \pi^- \\ \Lambda &\rightarrow \pi^0 n/p\pi^- \\ \pi^0 &\rightarrow \gamma\gamma \\ and,\ \pi^- + A &\rightarrow n + X/\gamma + X'. \end{aligned}$$

The expected number of events above the threshold was defined as S and the other was defined as N. The threshold was determined to achieve the best significance ($S/\sqrt{N}$). The significance depending on a threshold for the stop probability is plotted in Fig. 3.60. When the threshold is set at 9%, the best significance was achieved. In this thesis, selecting events with 9% or more stop probability is called the "kinematical selection". As you can seen in Fig. 3.59, this selection is almost equivalent to selecting the Ξ^- momentum less than 0.6 GeV/c.

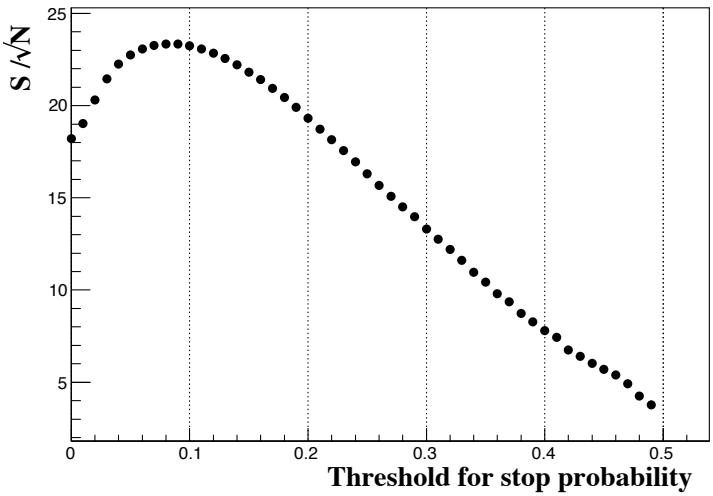

Figure 3.60: The stop probability threshold dependence of $S/\sqrt{N}$ where the number of events above the threshold for the stop probability is defined as S and the other is defined as N.

It was impossible to identify the type of the (K^-, K^+) process event by event. Thus, the process (a) was assumed for all the events in the simulation. Thus, the stopping probability of particles produced via the other processes was not estimated correctly. It is justified, however, because almost only the process (a) was selected later by the missing mass as described below.

Reconstruct the missing mass

The missing mass distribution reconstructed from K^- and K^+ momentum is shown in Fig. 3.61. The black one represents all the (K^-, K^+) processes, and the red one represents the events with the SSD1 rejection and the kinematical selection.

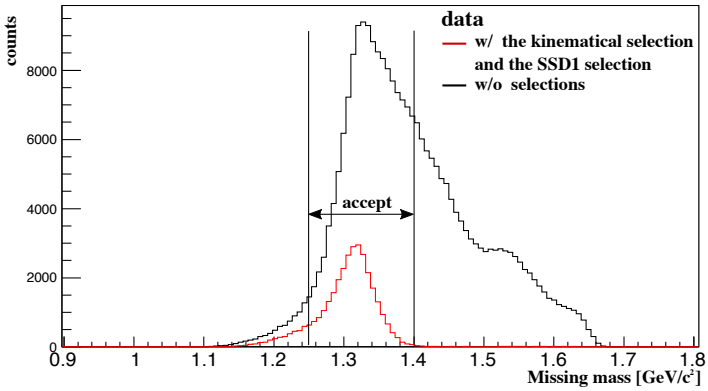

Figure 3.61: The reconstructed missing mass distribution. The distribution in black is with the (K^-, K^+) reaction, the distribution in red is with the SSD1 rejection and the kinematical selection.

To select the produced Ξ^- via the process (a), the missing mass distribution was estimated by simulation. The processes (a)-(d) were simulated following the uniform phase space of two-body and three-body decays taking into account as the followings.

- Proton momentum
  The momentum of a proton ($\overrightarrow{p_p}$) in a nucleus was assumed to follow the same distribution as in Fig.3.57 since it cannot be measured.

- Proton mass
  The energy should be conserved among the proton and the spectator, ^{11}B.
  The proton mass (M_p) was calculated as,

$$M_p^2 = \left(M_{^{12}\mathrm{C}} - \sqrt{{M_S}^2 + \overrightarrow{p_S}^2} \right)^2 - \overrightarrow{p}_p{}^2 \tag{3.17}$$

  where $M_{^{12}\mathrm{C}}$ is the mass of the ^{12}C nucleus and M_S and $\overrightarrow{p_S}$ are the mass and the momentum of the spectator .

- The (K^-, K^+) reaction angle
  K^+ was assumed to be emitted uniformly in the CM system for all the processes.

- Cross section
  The ratio of each process was based on the experimental data of the cross section. The total cross sections of (a), (b), (c), and (d) processes were 175 ± 16, 126 ± 6, 16 ± 4, and 34 ± 4 μb when the incident K^- momentum was 1.7 GeV/c [5].

- Experimental acceptance
  The geometrical acceptance of the KURAMA spectrometer was taken into account.

In the simulation, the (c) and (d) processes were treated as the same because the mass of produced particles, that is, $\Xi^-\pi^0$ and $\Xi^0\pi^-$ were not so much different. When the acceptance of the KURAMA spectrometer was considered, the simulated missing mass distribution was obtained as shown in Fig. 3.62. According to the simulation, the process (a) shown in red was dominant, and the other processes shown in blue and magenta contribute less than 1% in the region of the missing mass less than 1.4 GeV/c^2. Thus, the upper value of the selected region was set to 1.4 GeV/c. To achieve the best $S/\sqrt{N}$, the lower value was set to 1.25 GeV/c considering a contamination of background events (see Fig. 3.75).

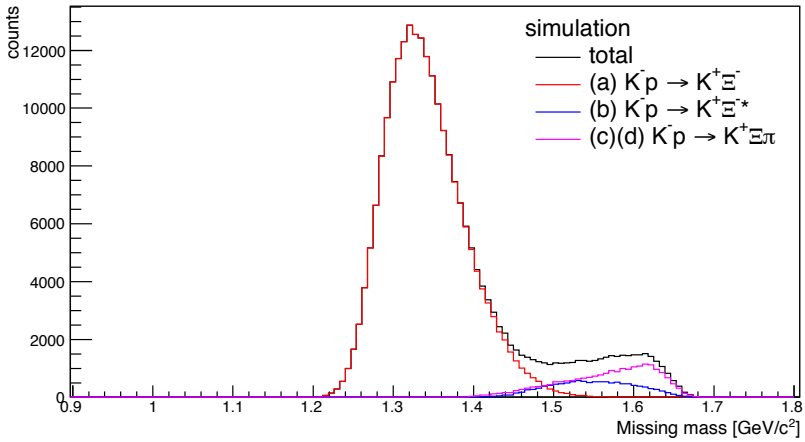

Figure 3.62: The simulated missing mass distribution for the each (K^-, K^+) processes.

3.5.2 X ray from Ξ^-C atom

The X-ray spectra obtained by the coincidence analysis of the magnetic spectrometers and Hyperball-X are shown in Fig. 3.63 with the following three conditions,

(a) with the (K^-, K^+) reaction,

(b) with Ξ^- production via the process (a),

(c) with a large probability of Ξ^- stopping in the target.

In the condition (a), the event set with the (K^-, K^+) reaction was selected. In the condition (b), Ξ^- production events were selected in the reconstructed missing mass distribution (1.25 - 1.4 GeV/c^2) in addition to the condition (a). In the condition (c), events with a large probability of Ξ^- stopping in the target were selected. That is, in addition to the condition (b), the SSD1 rejection and the kinematical selection were applied. The data was summed up for all the Ge detectors. The lower limit of a valid energy region of the spectrum, 120 keV, was set by the CFD threshold. The BGO suppression was always applied with a TDC gate of 50 ns.

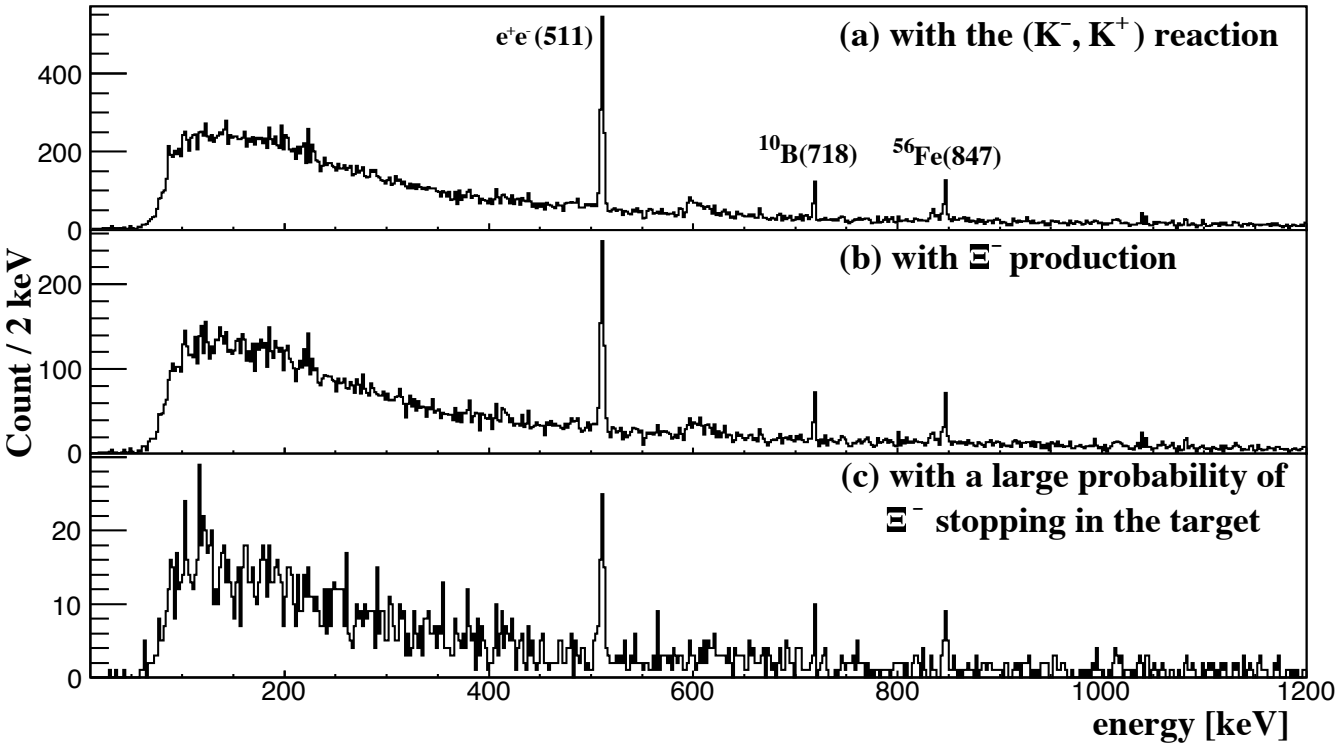

Figure 3.63: The X-ray spectrum with the (K^-, K^+) reaction. (a) is for the event set with the (K^-, K^+) reaction. (b) is for Ξ^- production, that is, missing mass selection is applied. (c) is for events with a large probability of Ξ^- stopping in the target, that is, the kinematical selection and the SSD1 rejection are applied.

Peak search

In the X-ray spectrum (c), the Ξ^-C atomic X-ray peak was searched for in the region from 100 to 470 keV. Since the shape of the background γ-ray distribution was not obvious, the shape of the spectrum (b) was approximated as a background shape of (c) since the S/N of (b) was much worse than that of (c). The expanded X-ray spectrum of (c) is shown in Fig. 3.64, and a scaled spectrum (b) is overlayed. To represent the difference between the scaled (b) and the (c) spectrum, the value $\Delta = \sum_i (y_i - y_i^{BG})^2$ was defined where y_i and y_i^{BG} represent counts in $i-$th bin of the (c) and the scaled (b), respectively. The scale factor was determined to minimize this Δ in the region from 500 to 800 keV, and it was 0.107.

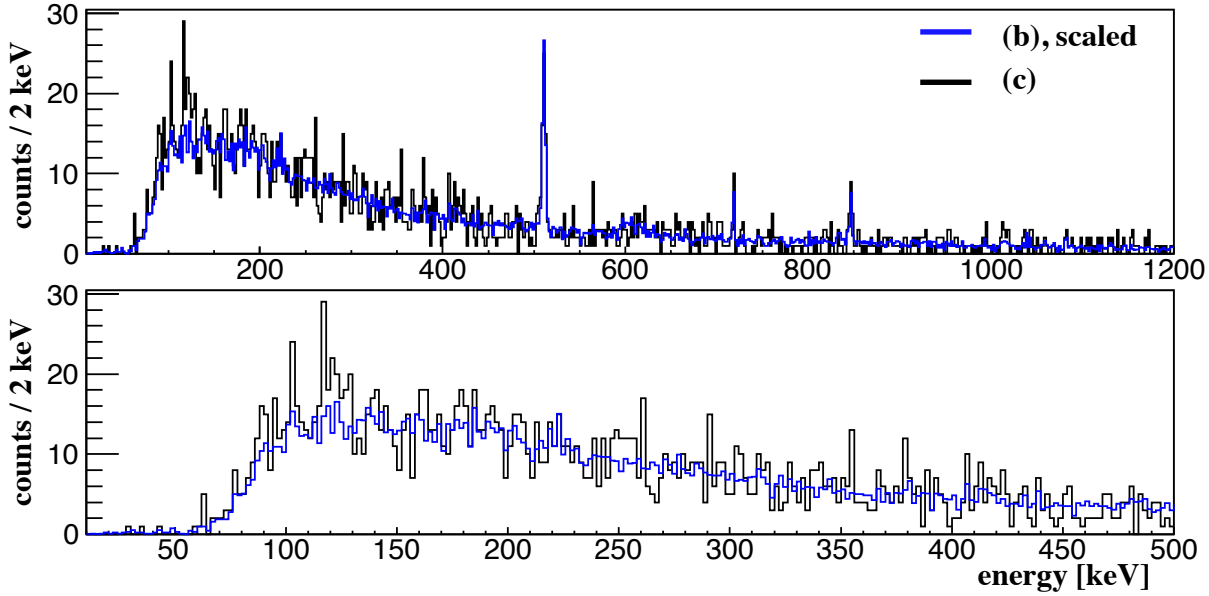

Figure 3.64: The X-ray spectra of the whole and expanded regions. The spectrum (b) for the events in coincidence with Ξ^- production is scaled and overlayed to spectrum (c) for the events in coincidence with Ξ^- with a large stop probability in the target.

The scaled (b) was fitted with a quadratic function as background in the fitting range $E_{mean} \pm \Delta E_{range}$, where E_{mean} was the center value of the fitting region ($2\Delta E_{range}$). An example of the fitting is shown in Fig. 3.65. The validity of a background fitting was evaluated with a reduced χ^2. The reduced χ^2 values as a function of E_{mean} were shown in Fig 3.66 when (b) was fitted in various ranges, that is, $2\Delta E_{range}$=100, 140, 180, and 250 keV where the degree of freedom (DOF) were 97, 137, 177 and 247, respectively.

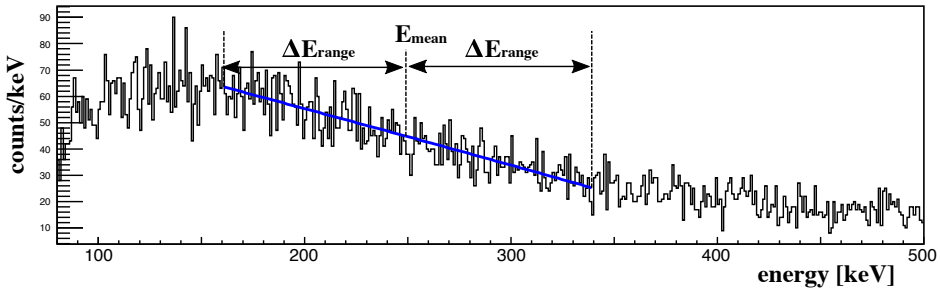

Figure 3.65: The example for the background fitting. E_{mean} is the center value of the fitting and fit region is $E_{mean} \pm \Delta E_{range}$.

To search for a X-ray peak, the spectrum (c) was fitted with the maximum likelihood method. A Gaussian plus a quadratic function were employed as peak fit function. The mean and sigma values of the Gaussian function were fixed in the fitting. The fixed mean value was changed from 100 to 470 keV with a 1-keV step. The AMP value was constrained to be 0 or more. The X-ray

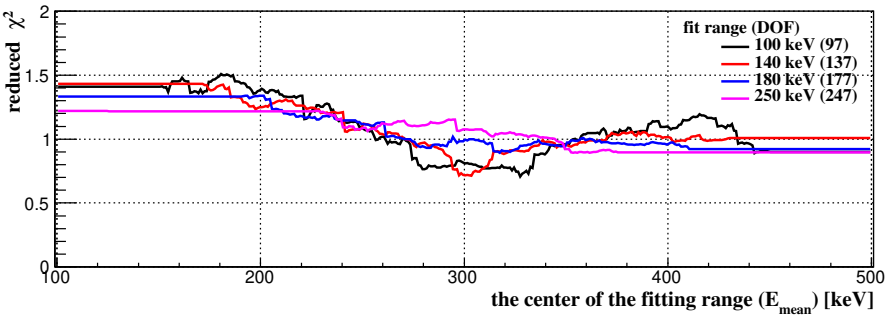

Figure 3.66: The reduced χ^2 of the background fitting as a function of the center of the fitting range, E_{mean} for the fit ranges of 100, 140, 180 and 250 keV. The horizontal axis represents the central of fit region. When the fit region over a valid ADC region, fit region is expanded to the other side.

peak count (N_{Xray}) was obtained with $\pm 1\sigma$ error. Peaks with a narrow width less than 10 keV in sigma as well as with a wide width more than 10 keV were searched for.

I) Search for a peak with a narrow widths ($\sigma_{Gauss} \leq$ 10 keV)

Peaks with narrow widths, that is, σ_{Gauss} =0.8, 1.2, 3, 5, and 10 keV, were searched for. Note that the width of 0.8 keV corresponds to the energy resolution of Hyperball-X. A peak was fitted in the range of 140 keV, namely mean $\pm$ 70 keV. The parameters of the background function obtained from the spectrum (b) were used as initial values of fitting.

As a result of the peak search, the peak significance was obtained as shown in Fig 3.67. No clear peak with 3σ significance was found. In the case of the 3 -10 keV width, a slightly enhanced structure was seen around 420 keV. However it was not claimed to be an evident peak because the peak significance was less than 3σ. In the case of the 0.8 keV width, there was a structure with a peak significance of 2.4σ around 116 keV. In this region, some Ge detectors had low efficiency due to a CFD threshold. It is possible that a statistical fluctuation or a dropping of the Ge efficiency makes this structure. Re-measurement with higher statistics is desired to confirm whether those enhancements are real peaks or not.

II) Search for a peak with a wide width ($\sigma >$ 10 keV)

Peaks with wide widths, that is, σ_{Gauss} =20, 40, 50, 60 and 80 keV, were also searched for. The spectrum was fitted to a Gaussian plus a background function in the range of 250 keV, that is, mean $\pm$ 125 keV by the maximum likelihood method. As the background, a quadratic function obtained from the spectrum (b) was employed and fixed. As a result of the peak search, the peak significance was obtained as shown in Fig 3.68. There was no evident peak structure in any cases. For the case of 20 - keV width, enhancement was seen around 180 keV and 420 keV. As mentioned above, the structure of around 420 keV was more enhanced when it is fitted with narrow widths.

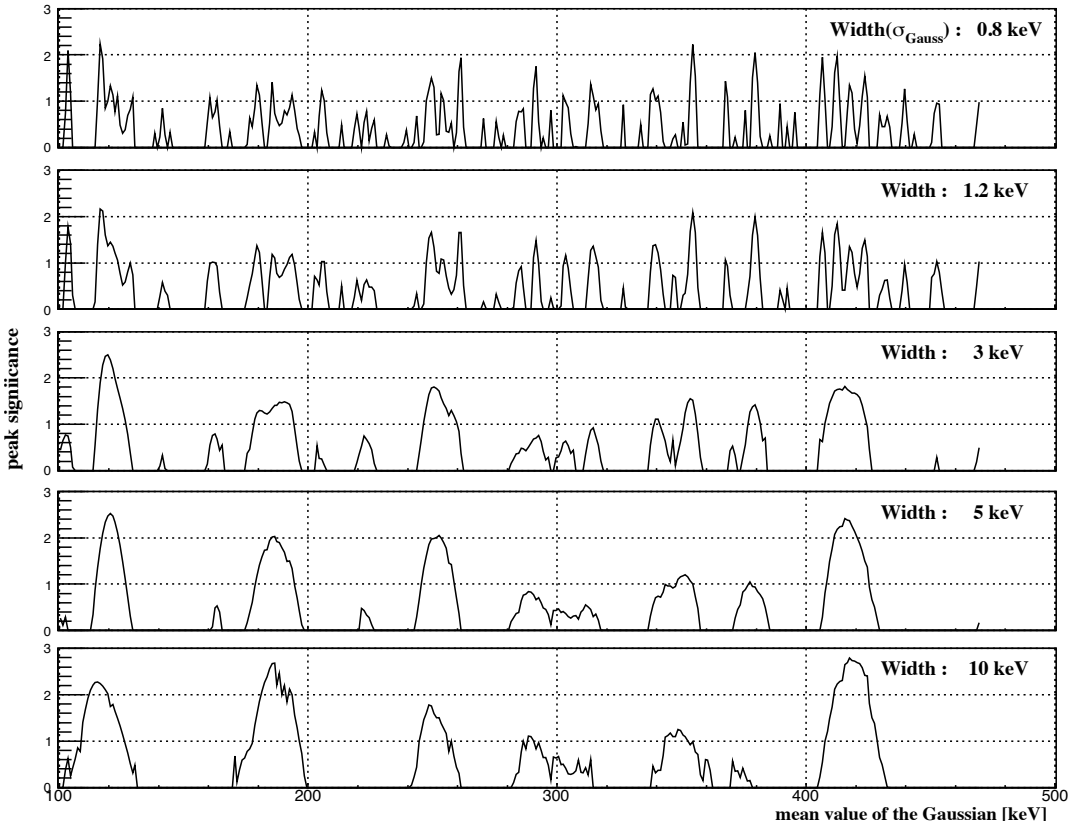

Figure 3.67: The peak significance for Ξ^-C atomic X rays assuming narrow widths.

3.5.3 Branching ratio ($3D \to 2P$)

No evident peak of Ξ^-C atomic X ray was observed. The upper limit of the X-ray yield of the $3D \to 2P$ transition from experimental observations and then information on the width of the $3D$ state was obtained. If the $3D$ state is the last orbit, its width may be broadened from being affected by strong interaction as shown in Fig. 3.69. The branching ratio of the $E1$ transition ($3D \to 2P$) is related to the partial widths of the $E1$ transition ($\Gamma_{E1}^{3D\to 2P}$) and the absorption from the $3D$ state ($\Gamma_{abs.}^{3D}$) as

$$BR(E1; 3D \to 2P) \;=\; \frac{\Gamma_{E1}^{3D\to 2P}}{\Gamma_{E1}^{3D\to 2P} + \Gamma_{abs}^{3D}} \tag{3.18}$$

The width of the $3D$ state, Γ^{3D}, is the sum of $\Gamma_{E1}^{3D\to 2P}$ and $\Gamma_{abs.}^{3D}$.

The imaginary part of the optical potential represents the effect that Ξ^- is absorbed by the nucleus via the reaction of $\Xi^- p \to \Lambda\Lambda$. The imaginary part of the eigenenergy (E_{Im}) is related to the total width of the sate as $E_{Im} = -\frac{i}{2}\Gamma$. Therefore, the width of the state is obtained by solving the Schrödinger equation assuming the Ξ^--nucleus potential, which can be constructed from a ΞN interaction potential. For example, using a real part of ΞN interaction in the Ehime potential and assuming an imaginary part as $W(r) = W_0 \exp(-r^2/\beta^2)$ with $\beta = 1$ fm, Ξ^--C potential is

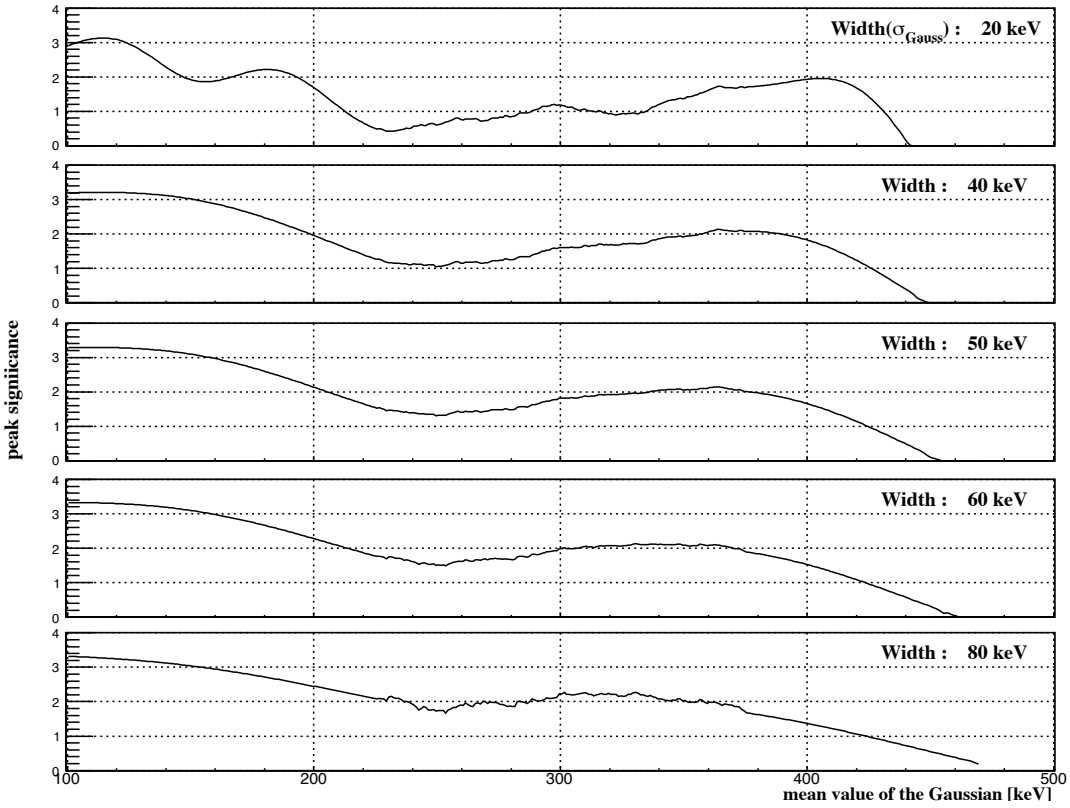

Figure 3.68: The peak significance for Ξ^-C atomic X rays assuming wide widths.

constructed and the binding energies of the Ξ^--C bound states are calculated [21] as listed in Table 3.10.

By comparing the branching ratio obtained by the experiment and that obtained by calculating $\Gamma_{E1}^{3D\to 2P}$, $\Gamma_{abs.}^{3D}$ can be extracted and further W_0 can be determined. In case1, $P_{\Xi(8J)} \cdot BR(8J \to 7I)$ can be evaluated from the X-ray yield (N_{Xrays}), the number of Ξ^- stopped and captured by atom ($N_{\Xi capture}$) and ϵ_{HBX}. Similarly, in the present case, the X-ray yield of the $3D \to 2P$ transition was also evaluated from the peak search and the efficiency of HBX was studied (see Section 3.2.2). The statistical error for X-ray yield derived from the fitting error of peak amplitude in the maximum likelihood method was typically 40% with 68% confidence level. $N_{\Xi capture}$ is evaluated below.

The number of Ξ^- stop events

From the event set selected to obtain the Ξ^-C atomic X-ray spectrum, the number of Ξ^- stopped in the target was estimated. The following three contaminations should be considered, that is,

- Ξ^- produced at SSD and the emulsion
- misidentification of p and π^+ in the scattered particle analysis

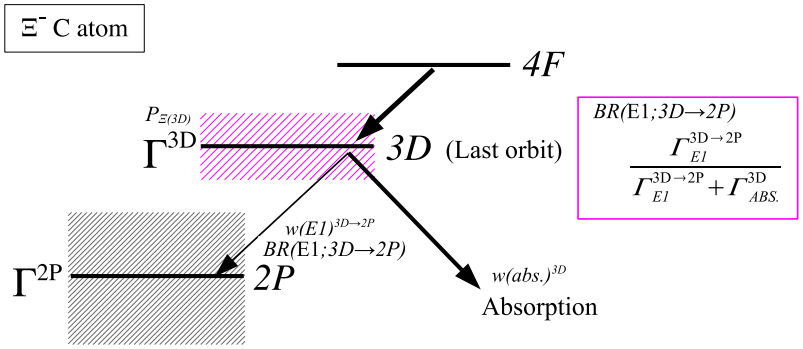

Figure 3.69: The levels of Ξ^-C atom. The $BR(3D \to 2P)$ is given by $\Gamma_{E1}^{3D\to 2P}$ and Γ_{abs}^{3D}. $w(E1)$ represents the transition probability of $E1$ and $w(abs.)$ represents the probability of absorption by the nucleus. They are proportional to the partial widths.

Table 3.10: The calculated binding energies of the Ξ^--C bound state using the Ehime potential[21].

		2P		3D		
	W_0	E [MeV]	Γ [MeV]	E [MeV]	Γ [MeV]	ΔE [MeV]
Coulomb + Ehime	0.0	-0.5833	0.0	-0.126	0.0	0.457
	-1.0	-0.5793	0.098	-0.126	0.725×10^{-5}	
	-3.0	-0.5470	0.288	-0.126	0.217×10^{-4}	
	-5.0	-0.4804	0.457	-0.126	0.359×10^{-4}	
	-7.0	-0.3733	0.589	-0.126	0.498×10^{-4}	

- the (K^-, K^+) processes other than $K^-p \to K^+\Xi^-$.

Each contamination was evaluated as described below.

Contamination of Ξ^- produced at SSD and the emulsion

As discussed in Section 3.3.3, since the vertex resolution in z direction was not sufficient, it is not possible to completely separate the events in which K^- reacted the target or SSD. When the selection of vertex z, $-50 < z < 0$ mm was applied, contamination of the Ξ^- produced in SSD1 and the emulsion was evaluated. The distribution of vertex z when the SSD1 rejection is applied is shown in black in Fig. 3.56. This is decomposed into two distributions, as shown in red and blue, in which Ξ^- was produced in the target or in SSD1 and the emulsion, by the same procedure as described in the Section 3.3.3. In the region of $-50 < z < 0$ mm, the ratio of the number of background events (the distribution in blue) to the total number of events (in black) was 9.3%.

Contamination of p and π^+

Background particles such as p and π^+ are contaminating the mass square distribution of scattered particles. Within the gate of the mass square, the contamination ratios of p and π^+ to K^+ were estimated by fitting the mass square distribution shown in Fig. 3.70 by a background plus a K^+ peak function. Note that the kinematical and SSD1 rejection were applied. Assuming Gaussian tails as p and π^+ background shapes, this distribution was fitted by three Gaussian functions as shown in red line. Dashed lines show decomposition to three Gaussian functions, representing the K^+ peak and the p and π^+ background on both sides. The ratio of the K^+ peak and the contamination depends on the gate of mass square, and it was set for each K^+ momentum region as shown in the first column of Table 3.11. By using the mass square selection gates previously

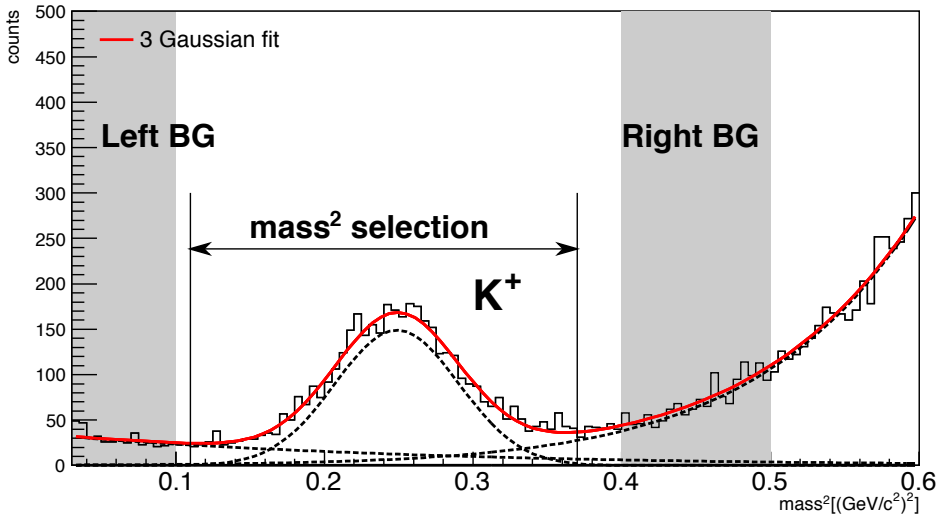

Figure 3.70: The mass square distribution of scattered particles.The distribution was fitted by three gauss functions shown in red. Dashed lines were decomposed gauss functions, representing the K^+ peak and background on both sides.

determined which depends on the K^+ momentum (see Fig. 3.52), the estimated ratio of K^+ and the background in those selected K^+ regions were obtained as shown in Table 3.11.

Table 3.11: The ratio of K^+ in the mass square distribution.

K^+ momentum [GeV/c]	mass^2 selection [(GeV/c^2)^2]	K^+ production [%]	left BG tail [%]	right BG tail [%]
0.6 - 0.8	0.19 - 0.29	86	9	5
0.8 - 1.0	0.17 - 0.31	83	11	6
1.0 - 1.1	0.14 - 0.34	78	14	8
1.1 - 1.2	0.13 - 0.35	76	15	9
1.2 - 1.4	0.11 - 0.37	72	17	11

When the kinematic selection and the SSD1 rejection were applied, the K^+ with the high momentum was selected. As seen in the K^+ momentum (p_{K^+}) distribution shown in red of Fig. 3.71, 90% of events distribute $p_{K^+} < 1.2$ GeV/c and the other 10 % distribute in $1.1 < p_{K^+} < 1.2$ GeV/c. That is, almost all particles were classified into the conditions in the bottom two rows of Table 3.11, and the the weighted average of K^+ production and BG was 72.4% and 27.6%, respectively.

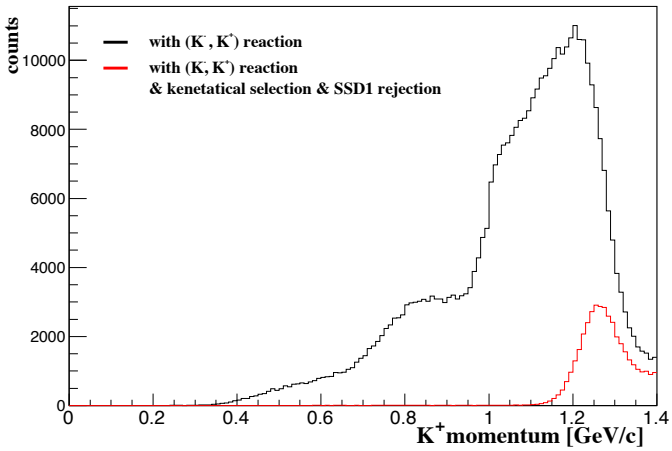

Figure 3.71: The K^+ momentum (p_{K^+}) distribution for the (K^-, K^+) reaction. Red line shows the p_{K^+} distribution with the kinematical selection and the SSD1 rejection.

As shown in Fig. 3.70, when the mass square was gated to select K^+, the missing mass distributed as shown in black in Fig. 3.72. When the left- and right- side background regions, the shaded regions in Fig. 3.70, were selected, the missing mass distributions were obtained as shown in red and blue in Fig. 3.72, respectively. The spectra are scaled to satisfy the ratio of the number of events, K^+ : left BG : right BG = 72 : 17 : 11. The right-side background, considered to be mainly as contamination of p, makes a tail in the lower missing mass.

In the above discussion, the function of three Gaussians only was assumed in the fitting. When the function of three Gaussians plus a constant was assumed, the mass distribution was fitted as shown in Fig. 3.73. The ratio of K^+ and the background contained in the $\pm 3\sigma$ region of the K^+ peak is 67 : 33. Differences in K^+ contribution due to fit functions, 5%, was considered as a systematic error of the analysis.

Contamination of the other process

The contamination from the other possible one-step quasi-free process in the (K^-, K^+) reaction was estimated. As described already, there are four possible one-step quasi-free processes. When calculating the stop probability, the Ξ^- mass was assumed. So the analysis was not correct for the processes other than (a) in which only Ξ^- was produced. Thus, contamination of these processes was estimated by simulation. The missing mass distribution via the four processes were simulated

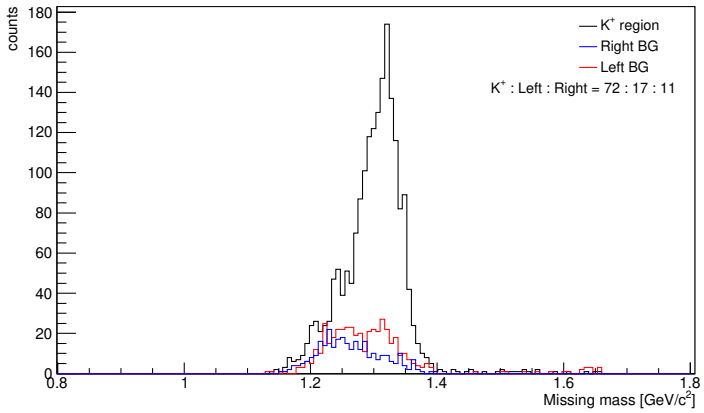

Figure 3.72: The missing mass distribution after the mass square (mass^2) of scattered particles was selected. When the mass square was gated on the K^+ region ($0.11 < \text{mass}^2 < 0.37$ [GeV/c^2]), on the left side background region ($0 < \text{mass}^2 < 0.1$ [GeV/c^2]), and on the right side background region ($0.4 < \text{mass}^2 < 0.5$ [GeV/c^2]) the missing mass distribution is shown in black, red and blue, respectively.

(see Fig. 3.62). In the same way, as the real data analysis, the Ξ^- stop probability was calculated event by event assuming that the produced particle was Ξ^- and the kinematical selection was applied. The obtained missing mass distribution is shown in Fig. 3.74. The distributions via the process (a), (b), (c) plus (d) are shown in red, blue and magenta, respectively. The end point of Ξ^- mass distribution via the process (a) is around 1.4 GeV/c^2. In the missing mass region less than 1.4 GeV/c^2, there were almost no contamination by the processes (b), (c), and (d). In addition, intermediate meson-induced two-step processes and the $K^-\text{p} \rightarrow f_0\Lambda, a_0\Lambda$, and $\phi\Lambda$ reaction, followed by the $f_0/a_0/\phi \rightarrow K^-K^+$decay is possible. They contribute to the mass distribution at the larger mass than Ξ^- mass. Thus, they were not considered in the simulation since experimental data about them were limited and they were not studied precisely.

Comparison with the data

The missing mass distribution was estimated by combining the simulated Ξ^-, Ξ^{-*}, $\Xi\pi$ production spectra and the contamination of p and π^+ based on real data. The ratio of K^+ production to p and π^+ contamination was 72 : 28, and the ratio of the (K^-, K^+) processes followed their total cross section. As shown in Fig. 3.75, this estimated distribution shown in red was compared to the data shown in black when the kinematical selection was applied. The estimated one was scaled so that the total number of events was equal to the data, and it can be decomposed into the processes (a) - (d) and the contamination of p and π^+, as the shaded histograms shown in the figure. Compared to the data, the estimation well reproduced the tails on both sides of the distribution. In the missing mass region less than 1.4 GeV/c^2, contaminations of the (K^-, K^+) processes not considered in the simulation are negligibly small. When the number of events in the

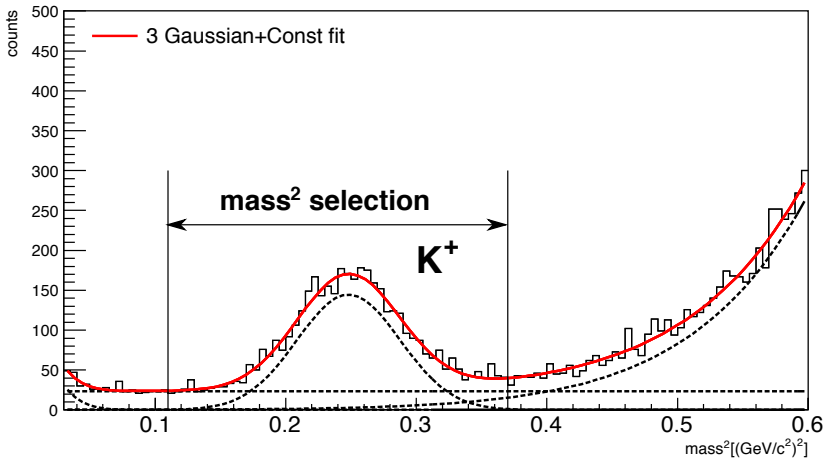

Figure 3.73: The mass square distribution of scattered particles fitted by three gauss plus constant functions. The decomposed gaussian functions and constant function were shown in doted lines. The ratio of K^+ and background including with the mass^2 selection is 67 : 33.

process (a) was regarded as signal (S) and the other contamination as noise (N), the missing mass (MM) region of 1.25 $<$ MM $<$ 1.4 GeV/c^2 was selected so as to maximize the $S/\sqrt{N}$ value. The process (a) contributes by 80% in this region.

As discussed above, with the condition that the mass square distribution was fitted with three Gaussians plus a constant function of K^+: contamination of $p, \pi^+ = 67{:}33$, the missing mass distribution was also estimated. The Ξ^- contributes by 75% in the region of 1.25 $<$ MM $<$ 1.4 GeV/c^2. The number of produced Ξ^- had a systematic error of a few percents, which was small compared to the error for X-ray yield of 40%. The minimum value of Ξ^--stop number was evaluated employing Ξ^- contamination of 75%.

The expected yield of Ξ^- stops in the target

When the kinematical selection, the SSD1 rejection and the missing mass selection were applied, 3.5×10^4 events are selected. The expected number of the events in which the produced Ξ^- particle stops in the target is estimated to be 5437. 90.7% of them reacted in the target and 80_{-5}% was produced via the process (a). Finally, the expected value of the number of Ξ^- stopped in the target was 3945_{-246}. Considering the error, the value with lower error, 3699, was employed to evaluate the BR.

Evaluation of the branching ratio

The branching ratio $BR(3D \to 2P)$ was evaluated according to Eq. 3.15. The Ξ^- stopped in the target would be captured by a carbon nucleus, but not by the other species. Thus, $N_{\Xi capture}$ should be equal to the number of Ξ^- stop, namely 3699 events. As for the ϵ_{HBX}, a value evaluated in

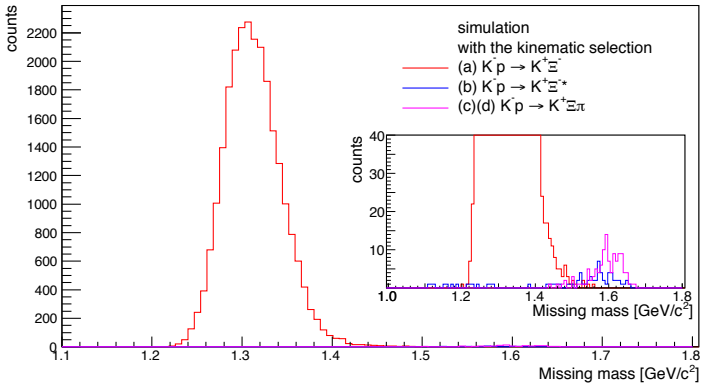

Figure 3.74: The simulated missing mass distributions of the one-step (K^-, K^+) processes with the kinematical selection. The expanded distributions are shown in the inset figure.

Section 3.2.2 was employed, and its typical value was 1% at 300 keV. When the BGO suppression was applied, the signal survival ratio was also considered as a part of the ϵ_{HBX}. The X-ray yield (N_{yield}) was obtained by the peak fitting. $P_{\Xi}(3D)$ of Ξ^-C atom has yet to be theoretically calculated. Thus, it was assumed to be 0.6 which is the same as in the case of Ξ^-Ag atom in this thesis. Finally, since the upper limit of the $BR(3D \to 2P)$ was discussed, the minimum values of $N_{\Xi capture}$ and ϵ_{HBX} were used in evaluation.

The evaluated $BR(3D \to 2P)$ as a function of E_{mean}, which is the mean of the Gaussian function used in the fitting, is plotted in Fig. 3.76. It is the case of the assumed peak width of 0.8 keV. The center values of BR are shown with black dots and the errors representing 68% confidence level. The 68% upper limits are shown with a black line. The axis of the X-ray energy shift (ΔE) of the $(3D \to 2P)$ transition is added at the top. For the case of the wide peak width of 20 keV, BR is also plotted as in Fig. 3.77.

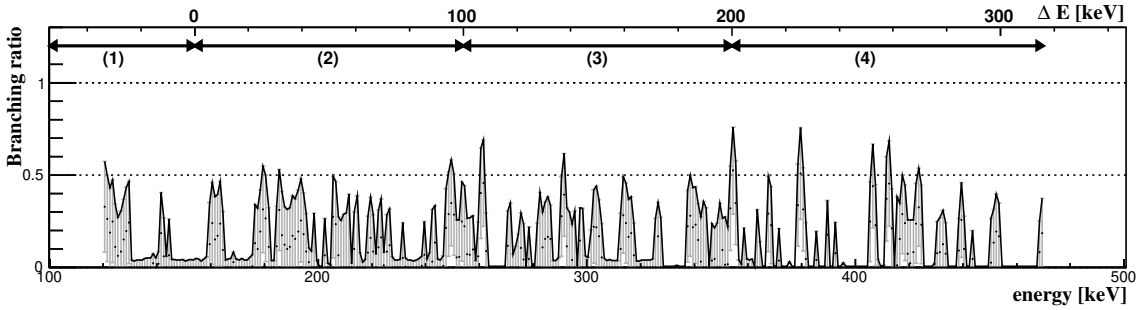

Figure 3.76: The BR($3D \to 2P$) assuming narrow width (0.8 keV).

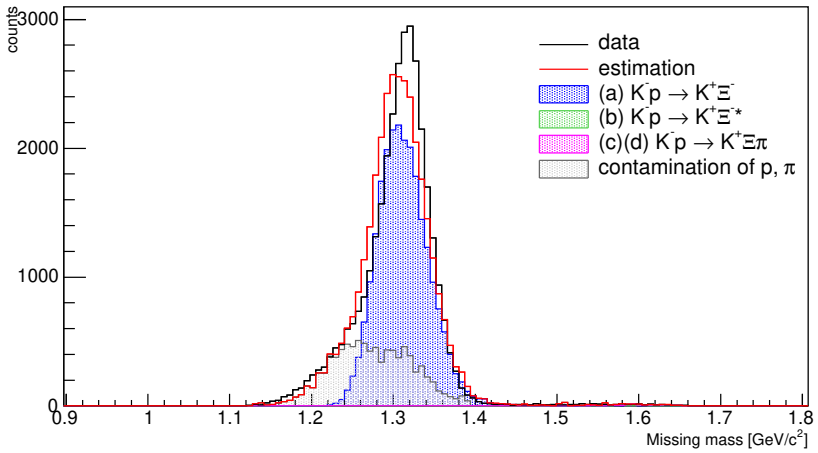

Figure 3.75: The comparison of the missing mass of experimental data and the estimated one. The estimated means the spectrum obtained by combining MC simulated Ξ^-, Ξ^{-*}, $\Xi\pi$ production spectra and contamination of p and π^+ estimated based on the real data.

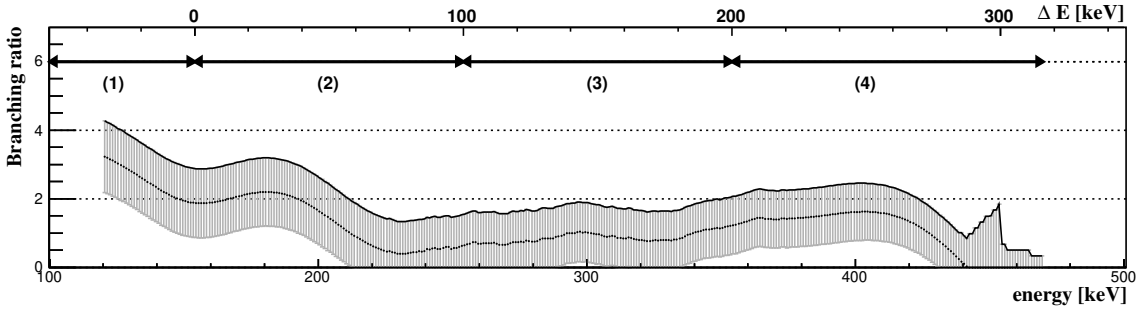

Figure 3.77: The BR($3D \to 2P$) in the case of wide widths (20 keV).

The X-ray energy region was divided based on the energy shift ΔE, that is, (1) $\Delta E \leq 0$ keV, (2) $0 < \Delta E \leq 100$ keV, (3) $100 < \Delta E \leq 200$ keV, and (4) 200 keV $< \Delta E$. The upper limit of BR was taken from the maximum point in each region of ΔE, and it was obtained as a function the experimental X-ray peak width, σ_{exp}, as shown in Fig. 3.78.

Comparison to theoretical calculations

The experimentally obtained BR value was compared with the theoretical calculation given by Eq. 3.18.

Firstly, Γ_{abs} was obtained by numerically solving the Schrödinger equation assuming an optical Ξ^--nucleus potential of Woods-Saxon type as shown in Fig. 3.50. Since the depth of the real part of the potential V_0 was suggested to be $10 - 20$ MeV [10], the Schrödinger equation was solved with assumption of $V_0 = -15$ or -20 MeV and of $W_0 = 0 - 2.0$ MeV. Details of the numerical

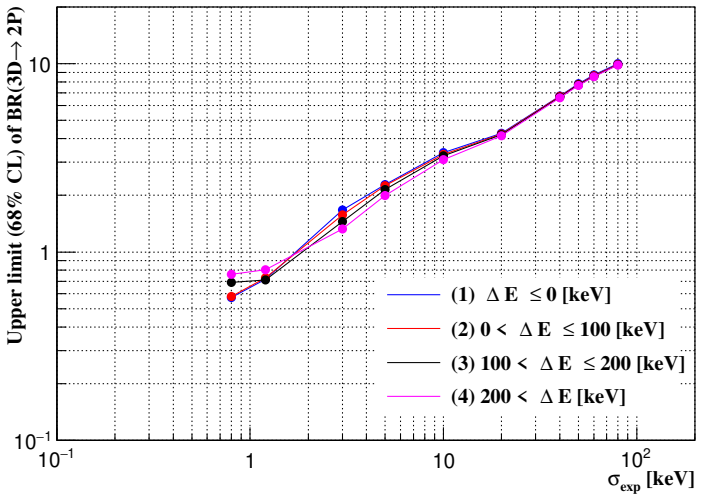

Figure 3.78: The experimentally obtained upper limit of $BR(3D \to 2P)$ as a function of the X-ray peak width σ_{exp}. The upper limit of branching was evaluated in the regions (1) $\Delta E \leq 0$ keV, (2) $0 < \Delta E \leq 100$ keV, (3) $100 < \Delta E \leq 200$ keV, and (4) 200 keV$< \Delta E$.

calculation is explained in Appendix A. The results of the calculation for the atomic $2P$ and $3D$ states are listed in Table. 3.12. The correlation between the BR and W_0 is obtained as shown in Fig. 3.79. For the cases of V_0 is -15 MeV and V_0 is -20 MeV are shown in red and black, respectively.

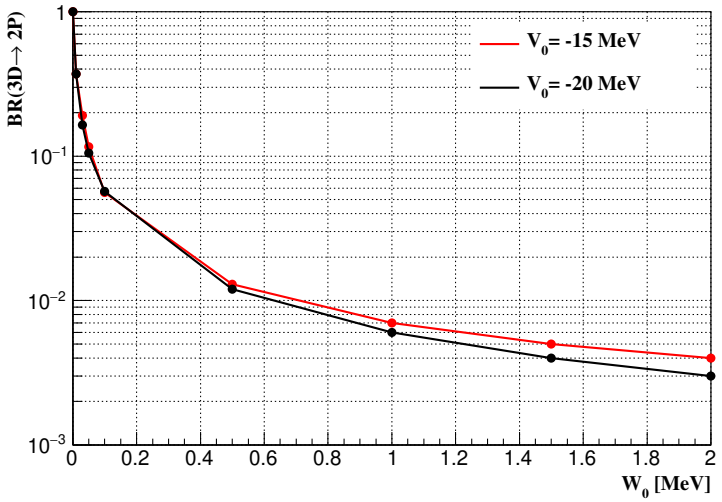

Figure 3.79: The correlation between the BR and W_0

Table 3.12: The theoretically calculated energies and widths assuming the Woods-Saxon type potential.

		$2P$		$3D$			
V_0 [MeV]	W_0[MeV]	E[MeV]	Γ_{abs}[MeV]	E[MeV]	Γ_{abs}[MeV]	Γ_{E1}[MeV]	BR
-15	0.0	-0.219	0	-0.126	0	2.36×10^{-7}	
	-0.01	-0.219	1.47×10^{-4}	-0.126	4.00×10^{-7}	2.36×10^{-7}	0.37
	-0.03	-0.219	4.40×10^{-4}	-0.126	1.00×10^{-6}	2.36×10^{-7}	0.19
	-0.05	-0.219	7.33×10^{-4}	-0.126	1.80×10^{-6}	2.36×10^{-7}	0.12
	-0.1	-0.219	1.47×10^{-3}	-0.126	4.00×10^{-6}	2.36×10^{-7}	0.056
	-0.5	-0.219	7.31×10^{-3}	-0.126	1.80×10^{-5}	2.43×10^{-7}	0.013
	-1.0	-0.219	1.45×10^{-2}	-0.126	3.60×10^{-5}	2.40×10^{-7}	0.0066
	-1.5	-0.22	2.15×10^{-2}	-0.126	5.20×10^{-5}	2.44×10^{-7}	0.0047
	-2.0	-0.22	2.81×10^{-2}	-0.126	6.40×10^{-5}	2.55×10^{-7}	0.0040
-20	0.0	-0.242	0	-0.126	0	3.53×10^{-7}	
	-0.01	-0.242	5.92×10^{-5}	-0.126	6.00×10^{-7}	3.53×10^{-7}	0.37
	-0.03	-0.242	1.78×10^{-4}	-0.126	1.80×10^{-6}	3.53×10^{-7}	0.16
	-0.05	-0.242	2.96×10^{-4}	-0.126	3.00×10^{-6}	3.53×10^{-7}	0.11
	-0.1	-0.242	5.93×10^{-4}	-0.126	5.80×10^{-6}	3.52×10^{-7}	0.057
	-0.5	-0.242	2.96×10^{-3}	-0.126	2.92×10^{-5}	3.52×10^{-7}	0.012
	-1.0	-0.242	5.89×10^{-3}	-0.126	5.82×10^{-5}	3.51×10^{-7}	0.0060
	-1.5	-0.242	8.77×10^{-3}	-0.126	8.66×10^{-5}	3.50×10^{-7}	0.0040
	-2.0	-0.242	1.16×10^{-2}	-0.126	1.55×10^{-4}	3.48×10^{-7}	0.0030

Secondly, Γ_{E1} is given as calculated in Appendix B. Γ_{E1} value and the BR by Eq.3.18 are also shown in Table. 3.12. The correlations between the BR and the width Γ_{2P} are plotted in red and black for the case of V_0 depth of -15 MeV and -20 MeV, respectively, in Fig. 3.80.

On the other hand, the experimental X-ray peak width, σ_{exp} gave the width of the $2P$ state, $\Gamma(2P)$, assuming that $\Gamma(3D)$ is negligibly narrow compared to $\Gamma(2P)$. Considering the resolution of the Ge detectors, σ_{Ge}, $\Gamma(2P)$ is given as

$$\Gamma(2P) = \sigma(2P) \times 2.35 \cong \sqrt{{\sigma_{exp}}^2 - {\sigma_{Ge}}^2} \times 2.35. \tag{3.19}$$

At the point of $\Gamma(2P) = 2.0$ keV, $\sigma(2P)$ and σ_{Ge} are comparable, $\sim$0.85 keV. In the region of $\Gamma(2P)$ is less than 2.0 keV, $\Gamma(2P)$ can not be measured. Thus, the value at $\Gamma(2P) = 2.0$ keV was employed as the upper limit of BR in that region. The upper limit of BR as a function of $\Gamma(2P)$ with the condition (1) described previously is also shown in blue in Fig. 3.80. It shows the upper limit of 68% confidence level, and the lower side of the curve is allowed region. The cross point of the curves obtained by the data and the theoretical calculation corresponds to the lower limit of W_0. The upper limit was not low enough to reach the theoretical curve, and the curves did

not crossed. As a result, it is found that significant improvement of the experimental sensitivity is needed to constrain the W_0 value.

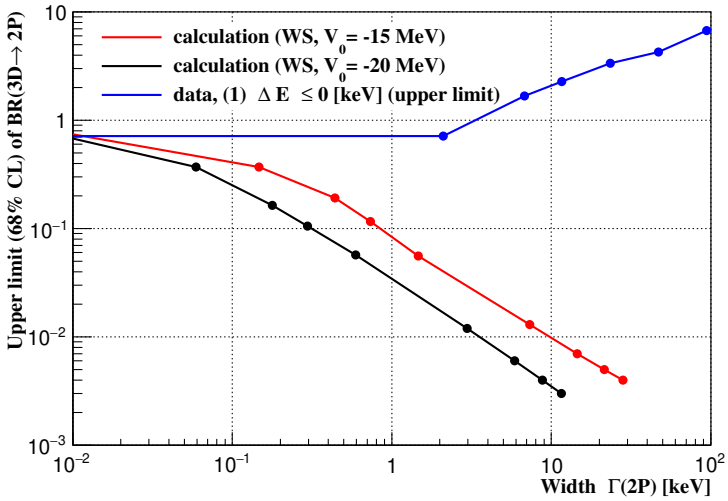

Figure 3.80: Comparison of the theoretical calculation and the experimentally obtained upper limit of the $BR(3D \to 2P)$. The result of theoretical calculation is shown in red and black for the case of V_0 depth of 15 and 20 MeV, respectively. The upper limit obtained by the experimental data is shown in blue. It is the result for the case of (1) $\Delta E \leq 0$.

Chapter 4

Conclusion and Outlook

4.1 Ξ^-Ag and Ξ^-Br atomic X rays

Conclusion

The data of 1279 σ-stop events were analyzed in coincidence with Hyperball-X. In both of the expected regions of Ξ^-Ag and Ξ^-Br atomic X rays, no evident peak was found. The background level was $0.17^{+0.57}_{-0.10}$ count per keV in the 370-keV region. The BR and P_Ξ were also evaluated, but the obtained upper limits were over 1 due to poor statistics. The background level obtained at present 20% statistics for Ξ^-Ag and Ξ^-Br atomic X rays are shown in Table 4.1.

Outlook

The data of the 67 emulsion modules, for which image analysis with selection (1) was finished, were analyzed. It corresponds to about 20% of the estimated σ-stop total yield in the emulsion exposed to the beam. Thus, it is expected that 4 times more statistics will be added in the future. Finally, an expected X-ray yield of the Ag($8J \to 7I$) transition will be 7.75 counts for $\Xi^-\sigma$-stop events. The $S/\sqrt{N}$ would be 4.56 in the $\pm 2\sigma$ peak region. Note that the $P_{\Xi(8J)}$ was assumed to be 0.6. In addition, 1.5 times of Ξ^- atomic X rays will be obtained by combining $\Xi^-\sigma$-stop and $\Xi^-\rho$-stop events. For that analysis, it is necessary to distinguish Ξ^- events from the background ρ-stop events of protons. The selection of "ρ-stop with an Auger emission" is useful. A half of $\Xi^-\rho$-stop events is identified since the 50% of ρ-stop events are accompanied by Auger electrons [7]. If $\Xi^-\rho$-stop events are identified completely, the X-ray yield will be 11.6 counts and the statistical error of the peak energy will be 250 eV. Considering a 250-eV statistical error and a 100-eV systematic error, the energy shift would be determined with a 270-eV accuracy. If a further experiment with a doubled beam time using a larger Ge array with 3 times the efficiency of Hyperball-X, a statistical error will be improved to be comparable with a systematic error, and the energy shift will be measured with a 100-eV accuracy. The estimation with full statistics for Ξ^-Ag and Ξ^-Br atomic X rays are summarized in Table 4.1.

Table 4.1: The BG level obtained in 20% statistics and estimation for full statistics. For yield estimation, P_{Ξ^-} is assumed to be 0.6.

		20% analyze	100% analyze (estimation)	
		BG level [counts/keV]	Yield [counts]	$S/\sqrt{N}$ ($\pm 2\sigma$)
Ag	$9K \to 8J$	0.32	8.80	3.77
	$8J \to 7I$	0.17	7.75	4.56
Br	$8J \to 7I$	0.76	6.64	1.85
	$7I \to 6H$	0.32	4.85	2.15

4.2 Ξ^-C atomic X rays

Conclusion

From the result of analysis for Ξ^- C atom, the upper limit of the $BR(3D \to 2P)$ was obtained as a function of the width of the X-ray peak. The upper limit was over 1 when a wider peak than the Ge resolution was assumed, and the result showed that the current experimental sensitivity was insufficient to give BR an upper limit. The result for the peak of 2-keV (FWHM) width ($\sim$ resolution of Ge detector) was compared to the model calculation in which the Ξ^--nucleus interaction was represented by a Woods-Saxon type optical potential in order to extract information on the imaginary part of the assumed potential. The well depth of the imaginary potential was not constrained by this experiment due to poor sensitivity.

Outlook

The experimental method for measurement of Ξ^- atomic X rays emitted from the reaction target was established, although it was found that some additional improvements were needed. It is necessary to improve the sensitivity by 3 times to constrain W_0 to be more than $\sim$10 keV, or by 10 times to constrain W_0 to be more than $\sim$100 keV.

Even though no evident peak was observed, evaluating the upper limit of the branching ratio of the $E1$ transition was useful for obtaining information on the imaginary part of the Ξ^--nuclear potential which describes Ξ^- absorption to a nuclei. This is useful especially for the transition where the BR value is estimated to be small such as the ^{12}C$(3D \to 2P)$ transition. In order to limit the W_0 depth, it is necessary to improve sensitivity by 10 times with some of the following improvements. Firstly, target thickness should be optimized to increase the yield $N_{\Xi capture}$. It should be optimized considering both of the Ξ^- stopping efficiency and the X-ray absorption. Secondly, the acceptance of the Ge detector array should be improved. If a more compact Ξ^- tracking detector is introduced instead of the SSD and the emulsion, more Ge detectors can be

installed around the target and the ϵ_{HBX} would be increased. Thirdly, better identification of scattered particles is needed to reduce background. The (K^-, K^+) reaction should be selected as cleanly as possible especially because contamination of protons makes background. Fourthly, the Ξ^- position detector with higher accuracy is needed to reject Ξ^- particles which are not stopped in the target. For example, a segmented scintillation target will be useful to measure the Ξ^- track directly although it is not as dense as diamond.

Observing cascade X-rays from a Ξ^- atom simultaneously is the most powerful way to measure the branching ratio. The energy for the $(4F \to 3D)$ transition of Ξ^-C atom is 55 keV considering only Coulomb force. Thus, the region of less than 100 keV should be measured.

Chapter 5

Summary

For a general understanding of the baryon-baryon interaction, investigating of ΞN interaction is necessary while experimental data are limited. The Ξ^- atomic X-ray spectroscopy is one of the useful ways to obtain information on the ΞN interaction. The shift of the X-ray transition energy (δE) from that of the Coulomb interaction only and the X-ray peak width give information of the real and imaginary parts of the Ξ^--nuclear potential, respectively.

From this research, important results are obtained as the first experimental attempt on Ξ^- atomic X-ray spectroscopy. The first Ξ^- atomic X-ray spectroscopy experiment (J-PARC E07) to measure Ξ^-C, Ξ^-Ag, and Ξ^-Br atomic X rays was performed at the J-PARC K1.8 beam line. In the experiment, Ξ^-s were produced in a diamond target via the (K^-, K^+) reaction. Some of them were stopped in the target or in the nuclear emulsion placed downstream of the target and then formed Ξ^- atoms. Two magnetic spectrometers were used in order to identify the (K^-, K^+) reaction events. Incident K^-s of 1.8 GeV/c momentum and scattered K^+s were analyzed by the beam line spectrometer and the KURAMA spectrometer, respectively. Ξ^- atomic X rays were measured using the Ge detector array called Hyperball-X. A new in-beam energy calibration method for the Ge detectors using LSO scintillators and ^{22}Na sources was developed and achieved a 100-eV accuracy.

Most of produced Ξ^-s decay before stopping and cause a huge background. In order to measure Ξ^- atomic X rays with good $S/\sqrt{N}$, two methods to select Ξ^--stop events were developed. In Method 1, Ξ^--stop events were identified by the nuclear emulsion image analysis. Based on the present analysis, the Ξ^-Ag and Ξ^-Br atomic X-ray spectrum was obtained with 20% statistics of the estimated total σ-stop yield. It was found that the background level was $0.17^{+0.57}_{-0.10}$ in 1 keV around the 370-keV region where the Ag($8J \to 7I$) transition is expected. When the emulsion image analysis is completed, an expected X-ray yield of the Ag($8J \to 7I$) transition will be 7.75 counts for the σ-stop events, and $S/\sqrt{N}$ would be 4.56 for the $\pm 2\sigma$ peak region. On the other hand, in Method 2, the Ξ^- produced with a large stop probability at the target is selected using information of the Ξ^- momentum. As a result, in the obtained Ξ^-C atomic X-ray spectrum, no evident peak was found. The upper limit of the branching ratio $BR(E1; 3D \to 2P)$ of the

Ξ^-C atom was experimentally evaluated. This limit was compared to the theoretical calculation using the Woods-Saxon-type Ξ^--nuclear optical potential. It was found that the experimental sensitivity was not sufficient to constrain the imaginary part of the Ξ^--nuclear potential. More improvements, for example optimization of the target thickness and developments of detectors to reject contamination of the background process, are required in the future experiment.

Appendix A

Numerical calculation of Schrödinger equation

In this chapter, the procedure to solve the Schrödinger equation is explained. Since the Schrödinger equation cannot be solved analytically in general, the approximate solution is obtained by numerical calculation.

A.1 Schrödinger equation

Theoretical component of the Schrödinger equation of Ξ^- bound system is given as

$$Hu_{nl}(r) = e_{nl}u_{nl}(r) \tag{A.1}$$

where $u_{nl}(r)$ is the radial wave function with the radial quantum number n and the orbital angular momentum l, and they are ortho-normalized as follows.

$$< u_{nl}(r)|u_{nl}(r) > \;=\; \int dr^3 r|u_{nl}(r)|^2 = 1, \tag{A.2}$$

$$< u_{n'l}(r)|u_{nl}(r)) > \;=\; \int dr^3 r u_{n'l}(r)u_{nl}(r) = \delta_{n'n}. \tag{A.3}$$

The Ξ^--nucleus Coulomb and strong potentials are represented as $V_{Coul.}(r)$ and $V_{opt}(r)$, respectively. The Hamiltonian is given by

$$H = -\frac{\hbar^2}{2m}\frac{d^2}{dr^2} + \frac{\hbar^2 l(l+1)}{2mr^2} + V_{Coul.}(r) + V_{opt}(r), \tag{A.4}$$

where m is the reduced mass of $\Xi^-$and the nucleus.

A.2 Numerical method

There are several numerical calculation methods. The radial space is divided into N by the mesh with a size of δr as shown in Fig A.1. $r_{max} = N\delta r$ should be far enough so that the wave function converges at $r = r_{max}$. The wave function $\mathbf{u}$ is given in matrix representation,

$$\mathbf{u} = \begin{pmatrix} u(r_0) \\ \vdots \\ u(r_{i-1}) \\ u(r_i) \\ u(r_{i+1}) \\ \vdots \\ u(r_{max}) \end{pmatrix} \tag{A.5}$$

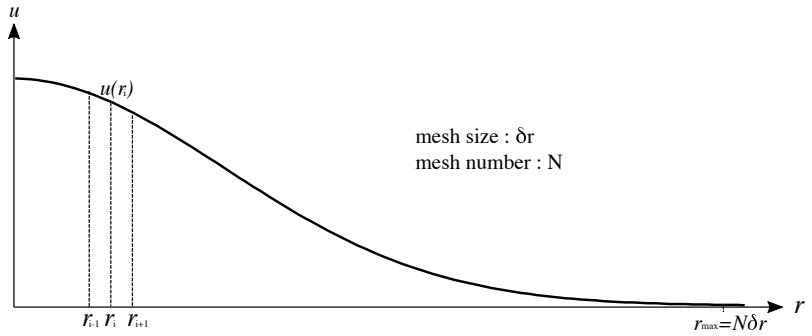

Figure A.1: The radial wave function. The radial space is divided into N by the mesh of size δr. $u(r_i)$ is the probability density function at r_i. r_{i+1} is given as $r_{i+1} = r_i + \delta r$.

The standard method to solve the equation is directly calculating Eq. A.1 at each point, namely, $u_{nl}(r_i)$ is calculated from $u_{nl}(r_i - 2)$ and $u_{nl}(r_i - 1)$ using the Numerov method or Runge-Kutta method. The procedure of the calculation is,

(1) Assuming an appropriate energy eigenvalue E_0, calculate the Schrödinger equation starting from around zero to r_{max}.

(2) In the same way as (1), calculate the Schrödinger equation starting from r_{max} to around zero with E_0.

(3) Check the connectivity of the wave function obtained in (1) and (2) at a certain point r_0.

(4) By changing the E_0 value, repeat the procedure (1) to (3) and E is determined.

For the case of Ξ^- atom with a complex potential, wave functions and energy eigenvalues are also complex.

Inverse Hamiltonian method

On the other hand, the inverse Hamiltonian method [43] [44] was employed in this thesis. Calculate according to the following procedure (also see a diagram in Fig. A.2),

(1) Introduce a first guess and form a reciprocal operator, $B_n = 1 + \Delta T/(H - E_0)$.
Introduce a set of ortho-nomalized functions $\{u_n^{k=0}\}$ as initial guess. The energy eigenvalues and eigenfunctions for the harmonic oscillator are employed as the initial guess.

(2) Apply the operator Bn to $\{u_n^{k=0}\}$ and make an updated states $\{u_n^{k+1}\}$.
Always they are ortho-nomalized using the Gram-Schmit process.

(3) Calculate the energy $e^{k+1} =< u_n^{(k+1)}|H|u_n^{(k+1)} >$
Calculate overlap using $H(r_i)$ and $u_n^{(k+1)}(r_i)$ at each point, then sum up them from r_0 to r_{max}. The derivative can be represented using the three point formula as $u(r_i)'' \approx (u(r_{i+1}) - 2u(r_i) + u(r_{i-1}))/(\delta r)^2$.

$$u'' = \frac{d\left(\frac{du}{dr}\right)}{dr} \tag{A.6}$$

$$\sim \frac{\frac{u(r+\delta r)-u(r)}{\delta r} - \frac{u(r)-u(r-\delta r)}{\delta r}}{\delta r} \tag{A.7}$$

$$= \frac{u(r+\delta r) - 2u(r) - u(r-\delta r)}{(\delta r)^2} \tag{A.8}$$

Thus, the Eq. A.1 is

$$-\frac{\hbar^2}{2m}\begin{pmatrix} -2 & 1 & 0 & 0 & \cdots & 0 \\ 1 & -2 & 1 & 0 & & \vdots \\ 0 & 1 & -2 & 1 & & \\ \vdots & & & \ddots & & \\ & & & & & \\ 0 & \cdots & & 0 & 1 & -2 \end{pmatrix}\mathbf{u} + \frac{\hbar^2 l(l+1)}{2m}\mathrm{diag}\left(\frac{1}{r_0^2}, \cdots \frac{1}{r_i^2}, \cdots \frac{1}{r_{max}^2}\right)\mathbf{u}$$
$$+\mathrm{diag}\left(V_{Coul}(r_0), \cdots V_{Coul}(r_i), \cdots V_{Coul}(r_{max})\right)\mathbf{u}$$
$$+\mathrm{diag}\left(V(r_0) + iW(r_0), \cdots V(r_0) + iW(r_i), \cdots V(r_0) + iW(r_{max})\right)\mathbf{u} \tag{A.9}$$

Note that $\mathrm{diag}(x_1, x_2, \cdots)$ represents diagonal matrix.

(4) Calculate dispersion of energy eigenvalue δE.
δE is defined as

$$\delta E \equiv \sqrt{\left[(H - e_{nl}^{k+1})\mathbf{u_{nl}^{k+1}}\right]^\dagger (H - e_{nl}^{k+1})\mathbf{u_{nl}^{k+1}}} \tag{A.10}$$

(5) Iterate (2) to (4) until δE becomes small enough.

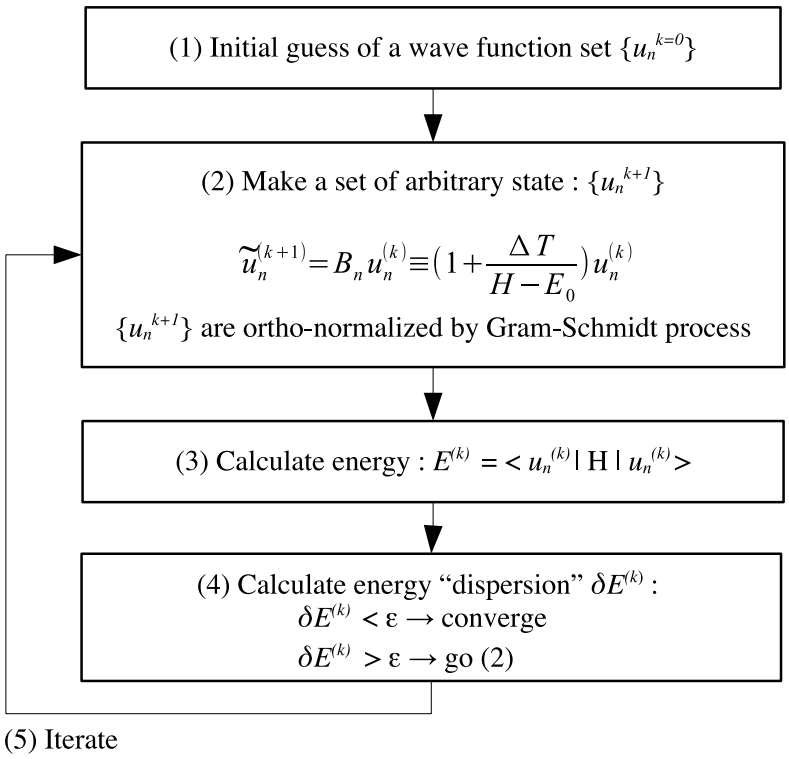

Figure A.2: Overview for the Inverse Hamiltonian method

A.3 Ξ^--C system

In this section, the calculation of Ξ^- -C bound system by the inverse Hamiltonian method is shown. Especially, the wave functions and eigenvalues of $2P$ and $3D$ state were obtained.

Ξ-nuclear potential

Assuming the potential of Woods-Saxon type as Ξ-nuclear potential as follows,

$$V_{opt}(r) = \frac{V_0 + iW_0}{1 + \exp\left(\frac{r-R}{a}\right)}. \tag{A.11}$$

where R is the nuclear radius, a is the diffuseness and V_0 and W_0 are well depths of the real and the imaginary potentials, respectively. R is $r_0 A^{1/3} = 1.27 A^{1/3}$ fm and a is 0.67 fm. The potential shape is shown in Fig. A.4 for the case of $V_0 = 15$ MeV and $W_0 = 1.5$ MeV.

Result

The mesh size and r_{max} should be set so that the wave function converges at r_{max}. In this case, the mesh size and r_{max} were taken as 0.1 fm and 500 fm, respectively, and the convergence of the

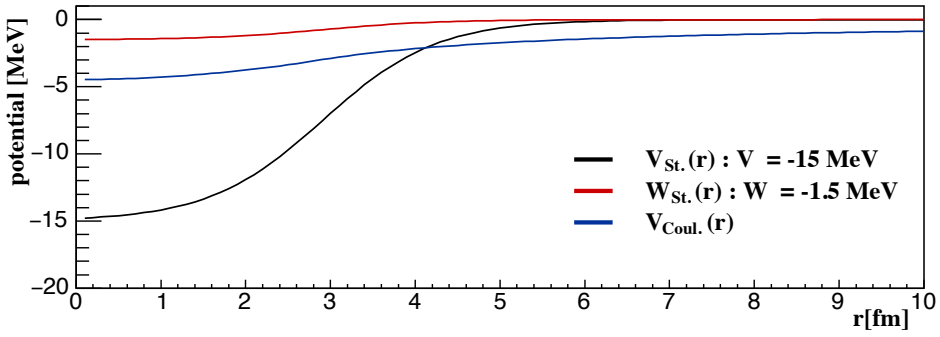

Figure A.3: The potential shape of ΞN interaction.

calculation was checked. If the obtained energy eigenvalue changes when the mesh is refined or r_{max} is larger, the calculation is not converged.

For the Ξ^--C system, the eigenvalue as a hydrogen like atom $E_N = -1.1336/N^2$, where N is the Coulomb principal quantum number defined as $N = n + l$. The effective Coulomb principlal quantum number N_{eff} is introduced as

$$N_{eff} \equiv \sqrt{\frac{E1}{E_{Re}}} \tag{A.12}$$

The result of calculation considering only Coulomb potential is shown in Table. A.1.

Table A.1: The calculated eigenvalues (E_{Re}) and N_eff for the case of that only the Coulomb interaction was considered.

nl	$E_{Re}[MeV]$	N_{eff}
1s	-0.939282	1.0986
1p	-0.282985	2.0015
2s	-0.257637	2.0976
1d	-0.125953	3.0000
2p	-0.125811	3.0017
3s	-0.118157	3.0974
2d	-0.070849	4.0000
1f	-0.070849	4.0000
3p	-0.070786	4.0018
4s	-0.067523	4.0974

The depth of the potential (V_0, W_0) are taken as (15 MeV, 0 MeV), (15 MeV, 1.5 MeV) and (20 MeV, 1.5 MeV), the obtained energy eigenvalues are shown in Table. A.2 For the case of (15 MeV, 1.5 MeV), from N_{eff} value, $2p$ and $1d$ state are identified as the $2P$ and $3D$ atomic state, respectively. The obtained wave functions shown in Fig.A.4 in black represent the $2P$ state. The

real part is shown in solid and the imaginary part is shown in dotted line. For the $3D$ state, they are also shown in red.

Table A.2: The calculated eigenvalues (E_{Re} and E_{Im}) and N_{eff} for the case of that the Coulomb and the strong interaction were considered.

caseA (V_0=15 MeV, W_0=0 MeV)				caseB (V_0=15 MeV, W_0=1.5 MeV)				caseC (V_0=20 MeV, W_0=1.5 MeV)			
nl	E_{Re}	E_{Im}	N_{eff}	nl	E_{Re}	EIm	N_{eff}	nl	E_{Re}	E_{Im}	N_{eff}
1s	-7.593339	-	0.3864	1s	-7.578491	-0.952363	0.3868	1s	-10.891140	-1.376294	0.3226
1p	-1.133883	-	0.9999	1p	-1.091383	-0.371776	1.0192	1p	-2.718265	-0.786759	0.6458
2s	-0.471038	-	1.5513	2s	-0.469902	-0.019224	1.5532	2s	-0.549581	-0.046017	1.4362
2p	-0.218504	-	2.2777	2p	-0.220356	-0.010751	2.2681	2p	-0.242393	-0.005787	2.1626
3s	-0.173247	-	2.5580	3s	-0.173046	-0.004379	2.5595	3s	-0.190447	-0.009224	2.4397
1d	-0.126126	-	2.9980	1d	-0.126124	-0.000026	2.9980	1d	-0.126232	-0.000057	2.9967
3p	-0.104323	-	3.2964	3p	-0.104905	-0.003468	3.2872	3p	-0.112118	-0.001919	3.1797
4s	-0.089453	-	3.5599	4s	-0.089387	-0.001636	3.5612	4s	-0.095766	-0.003277	3.4405
2d	-0.070952	-	3.9971	1f	-0.071836	-0.000967	3.9725	1f	-0.077082	0.001652	3.8349
1f	-0.070849	-	4.0000	2d	-0.070951	-0.000016	3.9972	2d	-0.071016	-0.000035	3.9953

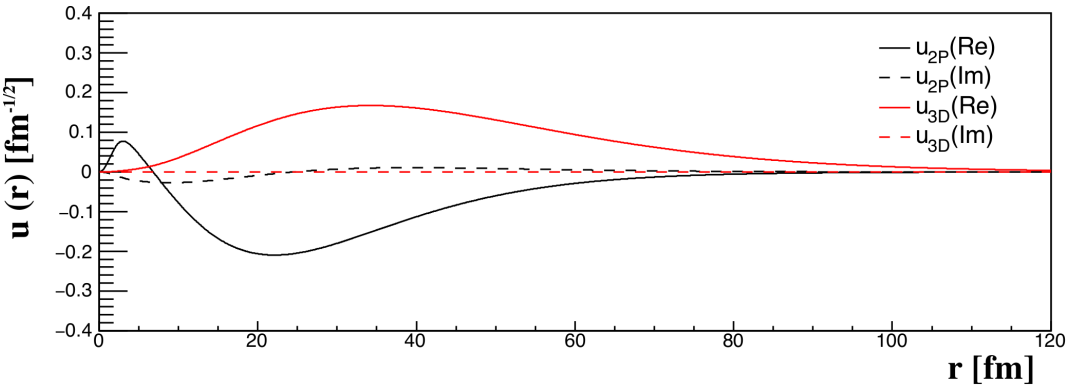

Figure A.4: The wave function of the $3D$ and $2P$ state shown in red and black for the condition of V_0 is 15 MeV and W_0 is 1.5 MeV. The solid and dotted line represent the real and imaginary part of wave function, respectively.

Appendix B

Calculation of $\Gamma_{E\lambda}$

In this section, how to obtain the width $\Gamma_{E\lambda}$ of the $E\lambda$ transition is explained. The width $\Gamma_{E\lambda}$ is related to the transition probability $w_\gamma(\lambda\mu)$ of γ-ray emission as $\Gamma = w\hbar$.

B.1 Transition probability of γ decay

With the atomic state transition from i to f states, a aphoton with an energy $\hbar\omega = E_i - E_f$ is emitted. This is radiation emission of the atom due to the charge density distribution ρ and current density distribution $\vec{j}$ oscillating over time. When the radiation energy emissions rate all over the sphere per unit time is written in $< W >$, the transition probability T is the radiation energy rate per the emitted photon energy of $\hbar\omega$, that is, $T =< W > /\hbar\omega$. The density of the radiation energy is given as a Pointing vector, $\overrightarrow{S} = \frac{c}{4\pi}\overrightarrow{E} \times \overrightarrow{H}$, where $\overrightarrow{E}$ and $\overrightarrow{H}$ are written in

$$\overrightarrow{E}(\vec{r}, t) = E\exp(-i\omega t) + c.c. \tag{B.1}$$

$$\overrightarrow{H}(\vec{r}, t) = H\exp(-i\omega t) + c.c. \tag{B.2}$$

For the $\sigma\lambda$ transition (σ is E or M), the transition probability of a proton emission with the multipolarity $\sigma\lambda\mu$, $T^{(\sigma)}_{\lambda\mu}$, is given as,

$$T^{(\sigma)}_{\lambda\mu} = \frac{8\pi(\lambda+1)}{\lambda[(2\lambda+1)!!]^2}\frac{k^{2\lambda+1}}{\hbar}|\mathfrak{M}^{(\sigma)}_{\lambda\mu}|^2, \tag{B.3}$$

where k is the wave number, $\mathfrak{M}^{(\sigma)}_{\lambda\mu}$ is the transition matrix element. The derivation of Eq. B.3 is explained in the reference[]. The transition matrix element is obtained as the expectation value of the $\sigma\lambda\mu$ moment as follows,

$$E\lambda: \quad < f|\mathfrak{M}^{(E)}_{\lambda\mu}|i > = e\int r^\lambda Y^*_{\lambda\mu}(\theta,\phi)\varphi^*_f(\mathbf{r})\varphi_i(\mathbf{r})dv \tag{B.4}$$

$$M\lambda: \quad < f|\mathfrak{M}^{(M)}_{\lambda\mu}|i > = -\frac{ik}{\lambda+1}\left(\frac{e\hbar}{Mc}\right)\int r^\lambda Y^*_{\lambda\mu}(\theta,\phi)\nabla\cdot(\varphi^*_f(\mathbf{r})\mathbf{L}\varphi_i(\mathbf{r}))dv \tag{B.5}$$

In addition, the terms of internal magnetic moment associated with the electron spin are given as below,

$$E\lambda: \ \mathfrak{M}'^{(E)}_{\lambda\mu} = -\frac{ik}{\lambda+1}\int r^{\lambda}Y^{*}_{\lambda\mu}(\theta,\phi)\nabla\cdot(\mathbf{r}\times\mathbf{M})d\tau \tag{B.6}$$

$$M\lambda: \ \mathfrak{M}'^{(M)}_{\lambda\mu} = -\int r^{\lambda}Y^{*}_{\lambda\mu}(\theta,\phi)\nabla\cdot\mathbf{M}d\tau \tag{B.7}$$

Usually, $\mathfrak{M}'^{(E)}$ can be ignored since it is smaller by 3 order than $\mathfrak{M}^{(E)}$.

B.2 Specific calculation of $T^{(E)}_{\lambda\mu}$

Consider the transition from the initial state $|n_i l_i m_i s_i\rangle$ to the final state $n_f l_f m_f s_f\rangle$ by the transition operator $\mathfrak{M}'_{\lambda\mu}$, where n is the radial quantum number, l is the orbital angular momentum, m is the magnetic quantum number and s is the spin quantum number. $\mathfrak{M}'_{\lambda\mu}$ changes the orbital angular momentum by λ, that is, $l'_f = \lambda + l_i$. Also, the magnetic quantum number is changed by μ as $m_f = \mu + m_i$. In general, since the angular momenta of the particles in the initial and final states are not aligned, $T^{(\sigma)}_{\lambda}$ is summed up m_f and average for m_i (divided by multiplicity $2l_i$+1). The same applies to the spin quantum number. Then we get,

$$T^{(E)}_{\lambda}(E_\gamma)[s^{-1}] = \frac{8\pi(\lambda+1)}{\lambda\{(2\lambda+1)!!\}^2}\times\alpha\times\frac{c}{e^2}\left(\frac{E_\gamma[MeV]}{197[MeV]}\right)^{2\lambda+1}B(E\lambda), \tag{B.8}$$

where c is the light speed, $\hbar c = 197$ MeV·fm, and $\alpha = e^2/\hbar c \cong 1/137$. Here, the reduced transition probability $B(\lambda)$ is defined as

$$B(E\lambda, n_i l_i \to n_f l_f) = \frac{1}{2(2l_i+1)}\sum_{s_i,s_f}\sum_{m_f,\mu,m_i}|\langle n_f l_f m_f s_f|\mathfrak{M}'^{(E)}_{\lambda\mu}|n_i l_i m_i s_i\rangle|^2 \tag{B.9}$$

B.2.1 Reduced transition probability B(λ)

Wigner-Eckart theorem

In general, the matrix element of the spherical tensor operator $\mathcal{T}^{(k)}_q$, which describes a transformation of coordinate rotation such as a spherical harmonics function, can be separated into two parts as

$$\langle\alpha JM|\mathcal{T}^{(k)}_q|\alpha' J'M'\rangle = \langle kq, J'M'|JM\rangle\langle\alpha J||\mathcal{T}^{(k)}||\alpha' J'\rangle \tag{B.10}$$

Here, the first part is the Clebsch-Gordan coefficient $\langle kq, J'M'|JM\rangle$, which depend on the magnetic quantum numbers, and the second part is the irreducible matrix element, $\langle\alpha J||\mathcal{T}^{(k)}||\alpha' J'\rangle$. This is the Wigner-Eckart theorem.

The Clebsch-Gordan coefficients are given in terms of the Wigner 3-j symbols by

$$\langle kq, J'M'|JM\rangle = (-1)^{k-J'+M}(2J+1)^{1/2}\begin{pmatrix} k & J' & J \\ q & M' & -M \end{pmatrix}. \tag{B.11}$$

B.2.2 Eλ transition

For the Eλ transition of $n_i l_i m_i s_i \to n_f l_f m_f s_f$, the expectation value of the electromagnetic moment including Eq. B.9 is calculated. The wave function $\Phi(\mathbf{r})$ is separated into a radial part u_{nl} and a angular part $Y_{lm}(\theta\phi)$. The Wigner-Eckart theorem is applied and the transition by the magnetic operator $\mathfrak{M}^{\mu}_{\lambda}$ is separated into a radial and an angular term as follows,

$$\langle n_f l_f m_f s_f | \mathfrak{M}^{\mu}_{\lambda} | n_i l_i m_i s_i \rangle = \left(\int d\Omega Y^*_{l_f m_f} Y_{\lambda\mu} Y_{l_i m_i} \right) \left(q_{eff} e \int dr r^{\lambda} u^*_{n_f l_f} u_{n_i l_i} \right), \tag{B.12}$$

where $Y_{\lambda\mu}(\theta\phi)$ is a spherical harmonics function.

Angular term

The angular component, given as the first term on the righthand side of Eq. B.12, is calculated. The operator of the transition is spherical harmonics function $Y_{\lambda\mu}$ and the Wigner-Eckart theorem is applied.

Or, Eq.(4.6.3) in "Angular momentum in quantum mechanics" by A.R. Edmonds [45],

$$\int_0^{\pi}\int_0^{\pi} Y_{l_1 m_1}(\theta,\phi) Y_{l_2 m_2}(\theta,\phi) Y_{l_3 m_3}(\theta,\phi) \sin(\theta) d\theta d\phi = \left[\frac{(2l_1+1)(2l_2+1)(2l_3+1)}{4\pi} \right]^{1/2} \begin{pmatrix} l_1 & l_2 & l_3 \\ 0 & 0 & 0 \end{pmatrix} \begin{pmatrix} l_1 & l_2 & l_3 \\ m_1 & m_2 & m_3 \end{pmatrix} \tag{B.13}$$

can be used. By taking a square of Eq. B.13, we get

$$\sum_{m_f,\mu,m_i} \left| \int d\Omega Y^*_{l_f m_f} Y_{\lambda\mu} Y_{l_i m_i} \right|^2 = \frac{(2l_f+1)(2\lambda+1)(2l_i+1)}{4\pi} \begin{pmatrix} l_f & \lambda & l_i \\ 0 & 0 & 0 \end{pmatrix}^2. \tag{B.14}$$

Here, the following formula was used:

$$\sum_{m_1,m_2} \begin{pmatrix} l_1 & l_2 & l_3 \\ m_1 & m_2 & m_3 \end{pmatrix} \begin{pmatrix} l_1 & l_2 & l'_3 \\ m_1 & m_2 & m'_3 \end{pmatrix} = \delta l_3 l'_3 \delta m_3 m'_3 \frac{1}{2l_3+1} \tag{B.15}$$

Radial term

The component of radial direction of Eq. B.12 is calculated by the wave function obtained in Appendix A and the operator ($\mathbf{r}^{\lambda}$).

Since the center of mass of the whole system is stopped, when the Ξ^- moves, the remaining part is recoiled. Along with this recoil motion, the Ξ^-'s charge is corrected as the effective charge q_{eff} considering the mass of core nucleus (M_N), the proton number (Z) and the mass of Ξ^- (m_{Ξ}),

$$q_{eff} = -\frac{M_N + Z m_{\Xi}}{M_N + m_{\Xi}}. \tag{B.16}$$

Residual transition probability $B(\lambda)$

From the above explanation, the reduced transition probability $B(E\lambda)$ is described as

$$B(E\lambda, n_i l_i \to n_f l_f) = \frac{1}{2(2l_i+1)} \sum_{s_i,s_f} \sum_{m_i,\mu,m_f} \frac{(2l_f+1)(2\lambda+1)(2l_i+1)}{4\pi} \begin{pmatrix} l_f & \lambda & l_i \\ 0 & 0 & 0 \end{pmatrix}^2 \left(q_{eff} e \int dr r^\lambda u^*_{n_f l_f} u_{n_i l_i} \right)^2 \quad \text{(B.17)}$$

The term of 3j symbols in Eq.B.20 has $m_1 = m_2 = m_3 = 0$. It can be calculated as follows [45],

$$\begin{pmatrix} l_1 & l_2 & l_3 \\ 0 & 0 & 0 \end{pmatrix} = (-1)^{J/2} \left[\frac{(lj_1 + l_2 - l_3)(l_1 + l_3 - l_2)(l_2 + l_3 - l_1)!}{(l_1 + l_2 + l_3 + 1)!} \right]^{\frac{1}{2}} \frac{(L/2)!}{(L/2 - l_1)!(L/2 - l_2)!(L/2 - l_3)!}, \quad \text{(B.18)}$$

where $L = l_1 + l_2 + l_3$.

B.2.3 Transition probability of C($3D \to 2P$)

Calculation of the probability for E1 transition of $3D \to 2P$ is described. The 3j-symbol term included in Eq. B.13 is calculated using the formula of Eq. B.18,

$$\begin{pmatrix} l' & 1 & l \\ 0 & 0 & 0 \end{pmatrix} = \begin{pmatrix} 2 & 1 & 1 \\ 0 & 0 & 0 \end{pmatrix} = (-1)^2 \left[\frac{2!2!0!}{5!} \right]^{1/2} \frac{2!}{0!1!1!} = \sqrt{\frac{2}{15}}. \quad \text{(B.19)}$$

Then Eq. B.20 is

$$\sum_{m_f,\mu,m_i} \left| \int d\Omega Y^*_{l_f m_f} Y_{\lambda\mu} Y_{l_i m_i} \right|^2 = \frac{3 \times 3 \times 3}{4\pi} \times \frac{2}{15} = \frac{3}{2\pi}. \quad \text{(B.20)}$$

After all, the transition probability $T^{(E)}_\lambda$ is obtained from Eq. B.8. The width $\Gamma^{(E)}_\lambda$ [MeV] is given from $T^{(E)}_\lambda$ as,

$$\Gamma^{(E)}_\lambda = \hbar T_\lambda(E_\gamma) \quad \text{(B.21)}$$

By applying $\lambda = 1$, calculated transition probability $T^{(E)}_1$ and width $\Gamma^{(E)}_1$ are obtained as a function of E_γ as shown in Fig. B.1. Note that the wave function was obtained assuming the well depths of the Ξ^- potential, V_0 and W_0, are 15 MeV and 1.5 MeV, respectively. In this case, the spacing of the $3D$ and $2P$ states is 0.94 MeV (see Table. 3.12) and the corresponding width of $3D$ state is 2.44×10^{-7} [MeV].

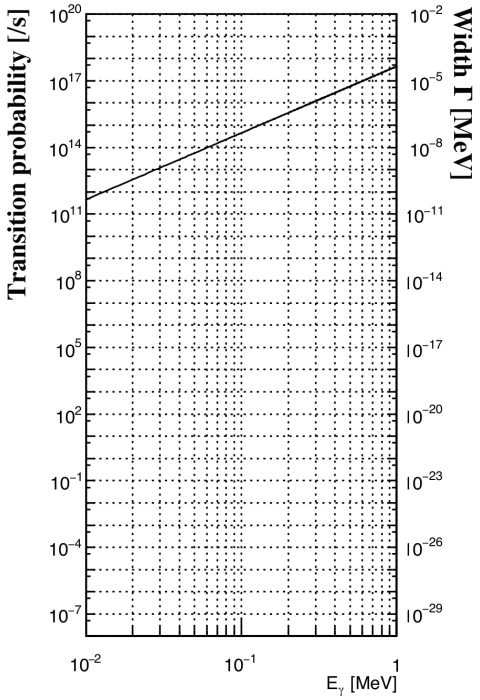

Figure B.1: The transition probability $T^{(E)}_{1\mu}$ and the width $\Gamma^{(E)}_{1\mu}$ of C $3D \to 2P$ transition for the case of the well depth of the Ξ^- potential V_0 is 15 MeV and W_0 is 1.5 MeV .

Bibliography

[1] O. Hashimoto and H. Tamura, Prog. Part. Nucl. Phys. **57**, 564 (2006).

[2] M. Tanabashi *et al.* (Particle Data Group), Phys. Rev. D **98**, 030001 (2018).

[3] R. Knorren, M. Prakash, and P. J. Ellis, Phys. Rev. C **52**, 3470 (1995).

[4] H. Noumi *et al.*, Phys. Rev. Lett. **89**, 072301 (2002).

[5] P.M. Dauber *et al.*, Phys. Rev. **179**, 1262 (1969).

[6] T. Iijima *et al.*, Nucl. Phys. A **546**, 588 (1992).

[7] KEK E176 Collaboration, S. Aoki *et al.*, Nucl. Phys. A **828**, 191 (2009).

[8] E224 Collaboration, Nucl. Phys. A **625**, 231 (1997)

[9] A. T. M. Aerts and C. B. Dover, Phys. Rev. D **28**, 450 (1983).

[10] T. Fukuda *et al.* (E224 Collaboration), Phys. Rev. C **58**, 1306 (1998).

[11] P. Khaustov *et al.* (The AGS E885 Collaboration), Phys. Rev. C **61**, 054603 (2000).

[12] A. Ichikawa, Ph.D. thesis, Kyoto University

[13] S. Aoki *et al.*, Prog. Theor. Phys. **89**, 493 (1993).

[14] S. Aoki *et al.*, Phys. Lett. B **355**, 45 (1995).

[15] H. Takahashi *et al.*, Phys. Rev. Lett. **87**, 212502 (2001).

[16] J. K. Ahn *et al.* (E373 (KEK-PS) Collaboration), Phys. Rev. C **88**, 014003 (2013).

[17] K. Nakazawa *et al.*, Prog. Theor. Exp. Phys. **2015**, 033D02 (2015).

[18] E. Hiyama and Y. Yamamoto, Prog. Theor. Phys. **128**, 105 (2012).

[19] D.J. Millener, Nucl. Phys. A **881**, 298 (2012).

[20] M. M. Nagels, T. A. Rijken, and J. J. de Swart, Phys. Rev. D **20**, 1633 (1979).

[21] M. Yamaguchi *et al.*, Prog. Theor. Phys. **105**, 627 (2001).

[22] E. Friedman and A. Gal, private communication (2001).

[23] C. J. Batty, E. Friedman, and A. Gal, Phys. Rev. C **59** 295 (1999).

[24] G. Backenstoss, T. Bunaciu, J. Egger, H. Koch, A. Schwitter, and L. Tauscher, Z. Physik A **273**, 137 (1975)

[25] C. J. Batty *et al.*, Phys. Lett. B **74** 27 (1978).

[26] R. J. Powers *et al.*, Phys. Rev. C **47**, 1263 (1993).

[27] C. J. Batty, E. Friedman and A. Gal, Phys. Rep. **287**, 385 (1997).

[28] K. Imai, K. Nakazawa and H. Tamura, Proposal of J-PARC E07.

[29] T. Takahashi, the Hadron Beamline Group, the K1.8 Experimental Group, Nucl. Phys. A **835**, 88 (2010).

[30] R. Honda *et al.*, Nucl. Instr. Meth. A **787**, 157 (2015).

[31] Y. Igarashi *et al.*, IEEE Trans. Nucl. Sci. **57**, 618 (2010).

[32] R. Honda and K. Miwa, Proceedings of 3rd International Workshop on New Photon Detectors, PoS Press., 031 (2012).

[33] Y. Igarashi, *et al.*, IEEE Trans. Nucl. Sci. **52**, 2866 (2005).

[34] T.O. Yamamoto *et al.* (J-PARC E13 Collaboration), Phys. Rev. Lett. **115**, 222501 (2015).

[35] K. Tanida, Hyperfine Interactions **193**, 81 (2009).

[36] S.Y.F. Chu, L.P. Ekström and R.B. Firestone, The Lund/LBNL Nuclear Data Search, Version 2 (1999).

[37] J. Myrheim and L. Bugge, Nucl. Instr. Meth. **160**, 43 (1979).

[38] J. Myrheim and L. Bugge, Three Dementional Computer Program (TOSCA) for Non-Linear Electromagnetic Fields, RL-81-070557 (1982).

[39] Y. Nara *et al.*, Phys. Rev. C **61**, 024901 (1999).

[40] H. Ekawa, Doctoral thesis, Kyoto University (2019).

[41] J. Yohida, private communication (2019.)

[42] The National Nuclear Data Center

[43] Yong Rae Kwon and F. Tabakin, Phys. Rev. C **18**, 932 (1978).

[44] K. Hagino and Y. Tanimura, Phys. Rev. C **82**, 057301 (2010).

[45] A. R. Edmonds, Angular momentum in quantum mechanics, Princeton University Press, (1957).